

DESIGN AND EVALUATION OF A MOBILE BEDSIDE PET/SPECT IMAGING SYSTEM

By

MATTHEW THOMAS STUDENSKI

A DISSERTATION PRESENTED TO THE GRADUATE SCHOOL
OF THE UNIVERSITY OF FLORIDA IN PARTIAL FULFILLMENT
OF THE REQUIREMENTS FOR THE DEGREE OF
DOCTOR OF PHILOSOPHY

UNIVERSITY OF FLORIDA

2009

© 2009 Matthew Thomas Studenski

To my family

ACKNOWLEDGMENTS

There are many people who have loved and supported me and are responsible for the completion of this work. I would like to thank my wife, Sindrishka, and my son, Alexander, for motivating me and supporting my work on this dissertation. Without their daily sacrifices and love, this research would never have been completed. I would like to recognize the love and support of my parents and sister in all my endeavors throughout my life. They are the reason that I am who I am today. I thank the members of my committee, Dr. Hintenlang, Dr. Shukla, and Dr. Van Oostrom for their insightful comments and critiques of my work. Finally, I thank Dr. Gilland, my mentor and advisor, who has guided me through my studies these last three years and has always pushed me to be the best that I could be. His daily challenges have prepared me well for the next step in my life.

TABLE OF CONTENTS

	<u>page</u>
ACKNOWLEDGMENTS.....	4
LIST OF TABLES	8
LIST OF FIGURES.....	9
ABSTRACT	13
CHAPTER	
1 THE MOBILE PET/SPECT SYSTEM.....	15
1.1 Purpose of the System.....	15
1.2 Nuclear Medicine.....	15
1.2.1 Positron Emission Tomography	16
1.2.2 Single Photon Emission Computed Tomography	16
1.3 Clinical Uses for PET and SPECT.....	17
1.4 Mobile Nuclear Medicine Systems	18
1.5 Multi-modality Nuclear Medicine	19
1.6 Our Mobile System Design Goals	19
1.7 511 keV SPECT	20
2 SYSTEM DESIGN	22
2.1 Detectors	22
2.2 Gantry.....	23
2.3 Detector Positioning.....	23
2.4 System Operation.....	24
3 SYSTEM PERFORMANCE EVALUATION	27
3.1 Introduction.....	27
3.2 Evaluation Methods	27
3.2.1 Energy Resolution	27
3.2.2 Spatial Resolution.....	28
3.2.3 Detection Sensitivity	30
3.2.4 Count Rate Capability	31
3.2.5 Flood Field Uniformity	31
3.2.6 Phantom Acquisition	31
3.3 Results.....	32
3.3.1 Energy Resolution	32
3.3.2 Spatial Resolution.....	32
3.3.3 Detection Sensitivity	33
3.3.4 Count Rate Capability	34

3.3.5	Flood Field Uniformity	34
3.3.6	Phantom Acquisition	35
3.4	Summary and Discussion.....	35
4	IMAGE ACQUISITION AND PROCESSING METHODS	42
4.1	Introduction.....	42
4.2	Methods.....	43
4.2.1	Experimental Phantom	43
4.2.2	Data Acquisition.....	44
4.2.3	Metz Filtering of the Projection Data.....	44
4.2.4	Image Reconstruction.....	45
4.2.5	Effect of Angular Sampling	46
4.2.6	Comparison with a Commercial SPECT System.....	47
4.3	Results.....	47
4.3.1	Septal Penetration Compensation.....	47
4.3.2	Comparison with a Commercial SPECT System.....	48
4.3.3	Effect of Angular Sampling	48
4.4	Summary and Discussion.....	49
5	DESIGN AND SIMULATION OF A HIGH ENERGY PINHOLE COLLIMATOR.....	57
5.1	Introduction.....	57
5.2	Methods.....	58
5.2.1	Theoretical Collimator Resolution and Sensitivity	58
5.2.2	Pinhole Collimator Design	60
5.2.2.1	Field-of-view and pinhole acceptance angle.....	60
5.2.2.2	Collimator focal length	60
5.2.2.3	Pinhole material	61
5.2.3	Axial Blurring With Pinhole Collimators	61
5.2.4	Determination of Pinhole Parameters.....	63
5.2.5	GATE Simulations	63
5.2.6	Keel Edge vs. Knife Edge Pinhole Collimator.....	64
5.2.7	Tomographic Comparison of Pinhole and Parallel Hole Collimators.....	65
5.3	Results.....	66
5.3.1	Acceptance Angle and Collimator Focal Length	66
5.3.2	Pinhole Collimator Design Parameters	67
5.3.2.1	Spatial resolution.....	68
5.3.2.2	Sensitivity.....	69
5.3.2.3	Pinhole diameter.....	70
5.3.3	Keel Edge Collimator.....	71
5.3.4	Tomographic Comparison.....	71
5.4	Conclusions.....	73
6	RADIATION DOSE TO SURROUNDING AREAS	85
6.1	Introduction.....	85

6.2	Methods.....	85
6.2.1	Regulatory Limits.....	85
6.2.2	¹⁸ F-FDG Effective Dose Calculation.....	86
6.2.2.1	Uptake period.....	88
6.2.2.2	Acquisition period.....	89
6.2.2.3	Decay period.....	89
6.2.3	^{99m} Tc Effective Dose Calculation.....	90
6.2.4	Effective Dose Reduction Options.....	91
6.2.4.1	Activity reduction.....	91
6.2.4.2	Portable shielding.....	92
6.3	Results.....	92
6.3.1	Dose to Other Immobile Patients.....	92
6.3.2	Dose to Staff not Treating the Injected Patient.....	93
6.3.3	Dose to Non-Occupational Staff Directly Treating the Patient.....	94
6.3.4	Dose to Occupational Staff in the ICU.....	94
6.3.5	Dose Reduction Techniques.....	95
6.3.5.1	Activity reduction.....	95
6.3.5.2	Portable shielding.....	96
6.4	Summary and Discussion.....	97
7	FUTURE WORK.....	103
7.1	Additional Studies.....	103
7.2	Defect Phantom Acquisitions.....	103
7.3	PET Performance Evaluation.....	104
APPENDIX		
A	SYSTEM INSTRUCTION MANUAL.....	108
A.1	Powering up the System.....	108
A.2	Testing the Detector.....	108
A.3	Setting the Channel Thresholds.....	108
A.4	Energy Calibration.....	108
A.5	Linearity Calibration.....	109
A.6	Starting an Acquisition.....	111
A.7	Acquisition Protocol.....	111
A.8	Powering the System Down.....	112
A.9	Troubleshooting.....	112
B	MATLAB CODE FOR IMAGE POST-PROCESSING.....	113
B.1	SPECT Listmode Data Processing.....	113
B.2	Center-of-rotation Correction.....	114
LIST OF REFERENCES.....		117
BIOGRAPHICAL SKETCH.....		121

LIST OF TABLES

<u>Table</u>		<u>page</u>
3-1	Low energy (140 keV) and high energy (511 keV) collimator parameters.	41
3-2	System spatial resolution.....	41
3-3	System sensitivity.....	41
5-1	Source-to-collimator distances at each projection angle obtained from an acquisition with the mobile system using a dynamic cardiac phantom.....	83
5-2	Reconstructed spatial resolution and sensitivity from GATE simulations for both the parallel hole and pinhole collimators.	84
5-3	Average sensitivity with the pinhole and parallel hole collimators calculated after eliminating the final projection angles with long source-to-collimator distances.	84
6-1	Portable shield weight for varying thicknesses of lead.....	102

LIST OF FIGURES

<u>Figure</u>	<u>page</u>
2-1 Various views of the mobile PET/SPECT imaging system.	25
2-2 Front view of the associated electronics rack and computers for the mobile system.	25
2-3 View of the detector head showing the 4×4 photomultiplier tube array and pixilated NaI crystal.	25
2-4 Computer-aided design drawings of the system gantry and the different detector positioning capabilities.	26
2-5 A single detector head fitted with a collimator can be used for single photon imaging to achieve complete angular sampling which might not be able to be achieved with a detector underneath the bed in PET mode.	26
3-1 Energy spectra obtained from 140 keV and 511 keV point sources.	36
3-2 Normalized intrinsic spatial resolution LSFs with ^{99m} Tc (140 keV) and ¹⁸ F (511 keV).	37
3-3 Normalized system spatial resolution LSFs at 10, 20, and 30 cm from the detector face for both 140 keV and 511 keV.	37
3-4 Line source images for system spatial resolution measurements.	38
3-5 Coronal slices from reconstructed SPECT images with point sources and the corresponding point spread functions in both the transaxial and coronal planes.	38
3-6 Count rate as a function of activity for 140 keV and 511 keV.	39
3-7 Raw, uncorrected flood images for both 140 keV and 511 keV energies.	39
3-8 45×45 pixel linearity corrected flood images for both 140 keV and 511 keV energies used to correct for uniformity in acquired images.	40
3-9 Reconstructed images from the dynamic cardiac phantom acquisitions with both ^{99m} Tc and ¹⁸ F.	40
4-1 The dynamic cardiac phantom and the bedside imaging system with the detector head in a left oblique position (45 degrees).	50
4-2 Point source images for 140 keV and 511 keV sources without windowing.	50
4-3 MTFs for both 140 and 511 keV point sources used in calculating the Metz filter.	51

4-4	Metz filters and the associated horizontal and vertical profiles from for both 140 keV and 511 keV with different values for X.....	51
4-5	Five projection angles demonstrating how different acquisition protocols can result in myocardial truncation.....	52
4-6	Parameters used in the center-of-rotation correction algorithm to allow for shifted detector positioning which eliminated myocardial truncation.....	52
4-7	Projection images obtained at 45 degrees using ^{99m}Tc and out-of-field activity with varying degrees of filtering.....	53
4-8	Projection images obtained at 45 degrees using ^{18}F and out-of-field activity with varying degrees of filtering.....	53
4-9	Comparison of the mobile system's performance to a commercial system using the dynamic cardiac phantom and ^{99m}Tc	54
4-10	Four long axis and four short axis slices from the 15 minute ^{99m}Tc acquisitions with 19 and 10 projection angles.....	54
4-11	Four long axis and four short axis slices from the ^{99m}Tc 135 degree angular coverage acquisition and the 90 degree angular coverage acquisition.....	55
4-12	Four long axis and four short axis slices from the ^{18}F acquisitions without activity in the liver and 37 and 19 projection angles.....	55
4-13	Four long axis and four short axis slices from the 30 minute ^{18}F acquisition (including out-of-field activity).....	56
5-1	Design parameters for a parallel hole collimator and pinhole collimator.....	74
5-2	Scale drawing demonstrating the effect of different acceptance angles on the field-of-view at different projection angles.....	75
5-3	Scale drawing demonstrating the FOV size with two different collimator acceptance angles and the Defrise phantom at different source-to-collimator distances.....	76
5-4	Difference between a knife edge and keel edge pinhole collimator.....	76
5-5	Coronal slices and profiles along the axis-of-rotation from the Defrise phantom reconstructions with two acceptance angles and varying radius-of-rotations.....	77
5-6	Transaxial and coronal slices from the NCAT phantom simulations with 70° and 90° acceptance angles.....	78
5-7	Theoretical profiles for both pinhole and parallel hole collimators with two different pinhole diameters at different locations in the FOV.....	79

5-8	Theoretical spatial resolution on the object plane of our parallel hole collimator compared to Metzler, <i>et al.</i> 's pinhole collimator prediction with varying source-to-collimator distances.....	80
5-9	GATE simulations of a point source with both the parallel hole and pinhole hole collimator.	80
5-10	Theoretical profile predicted by Cherry, <i>et al.</i> (dashed line) and the horizontal GATE profile (solid line) of a point source in air with varying source-to-collimator distances for the parallel hole collimator on the image plane.	81
5-11	Theoretical profiles predicted by Anger (dashed line) and Metzler, <i>et al.</i> (open circles) and the horizontal GATE profile (solid line) of a point source in air with varying source-to-collimator distances and photon entry angles for the pinhole collimator on the image plane.	81
5-12	Metzler, <i>et al.</i> 's theoretical pinhole collimator sensitivity relative to that of our parallel hole collimator over varying source-to-collimator distances.....	82
5-13	GATE sensitivity of the parallel hole and pinhole collimator at b= 10 cm with different degrees of thresholding demonstrating the effect of septal penetration photons.	82
5-14	Theoretical and GATE sensitivities relative to that of the theoretical parallel hole collimator with different source-to-collimator distances and photon entry angles.....	83
6-1	Top and side views of the distances assumed in the ICU for the dose calculation. The patient is red, portable shields are blue, and staff are green.	98
6-2	Total effective dose per exam integrated over all time periods at various distances from a patient for acquisitions with both ^{18}F and $^{99\text{m}}\text{Tc}$	99
6-3	Total effective dose per exam integrated over the first ten hours of the procedure at various distances from a patient for acquisitions with both ^{18}F and $^{99\text{m}}\text{Tc}$	99
6-4	Effective dose for staff directly treating the patient based on the time spent at 1 m from the patient for acquisitions with both ^{18}F and $^{99\text{m}}\text{Tc}$	100
6-5	Total effective dose during a ten hour shift for non-occupational staff directly treating the patient assuming that the time spent at 1 m is the same every hour and the rest of the time is spent at least 4 m from the patient for acquisitions with both ^{18}F and $^{99\text{m}}\text{Tc}$	100
6-6	Total effective dose during a 10 hour shift for occupational staff directly treating the patient assuming that the time spent at 1 m is the same every hour and the rest of the time is spent at least 4 m from the patient for acquisitions with both ^{18}F and $^{99\text{m}}\text{Tc}$	101

6-7	Total effective dose to immobile patients and staff in an adjacent room to the ICU with a patient injected with reduced amounts of ^{18}F or $^{99\text{m}}\text{Tc}$	101
6-8	Total effective dose with lead shields of varying thicknesses to patients and staff in the ICU for both ^{18}F and $^{99\text{m}}\text{Tc}$ procedures.	102
7-1	Pictures of the defect phantom showing the myocardium and the defect.	106
7-2	Short and long axis slices from the reconstructed image of the cardiac phantom with a defect at both 140 keV and 511 keV. White arrows indicate the defect.	107
7-3	Three slices from the preliminary, two projection angle PET acquisition with a ^{22}Na point source demonstrating the system's ability to process coincidence data.	107

Abstract of Dissertation Presented to the Graduate School
of the University of Florida in Partial Fulfillment of the
Requirements for the Degree of Doctor of Philosophy

DESIGN AND EVALUATION OF A MOBILE BEDSIDE PET/SPECT IMAGING SYSTEM

By

Matthew Thomas Studenski

May 2009

Chair: David Gilland

Major: Nuclear Engineering Sciences

Patients confined to an intensive care unit, the emergency room, or a surgical suite are managed without nuclear medicine procedures such as positron emission tomography (PET) or single photon emission computed tomography (SPECT). These studies have diagnostic value which can greatly benefit the physician's treatment of the patient but require that the patient is moved to a scanner. This dissertation examines the feasibility of an economical PET/SPECT system that can be brought to the bedside of an immobile patient for imaging.

We chose to focus on cardiac SPECT imaging including perfusion imaging using ^{99m}Tc tracers and viability imaging using ^{18}F tracers first because of problems arising from positioning a detector beneath a patient's bed, a requirement for the opposed detector orientation in PET imaging. Second, SPECT imaging acquiring over the anterior 180 degrees of the patient results in reduced attenuation effects due to the heart's location in the anterior portion of the body.

Four studies were done to assess the clinical feasibility of the mobile system; 1) the performance of the system was evaluated in SPECT mode at both 140 keV (^{99m}Tc tracers) and 511 keV (positron emitting tracers), 2) a dynamic cardiac phantom was used to develop and test image acquisition and processing methods for the system at both energies, 3) a high energy pinhole collimator was designed to reduce the effects of high energy photon penetration through

the parallel hole collimator, and 4) we estimated the radiation dose to persons that would be in the vicinity of a patient to ensure that the effective dose is below the regulatory limit.

With these studies, we show that the mobile system provides an economical means of bringing nuclear medicine to an immobile patient while staying below the regulatory dose limit to other persons. The system performed well at both 140 keV and 511 keV and provided viable images of a phantom myocardium at both energies. The system does not achieve the same sensitivity and spatial resolution as a dedicated system but performs well in detecting severe myocardial defects that would otherwise go undetected.

CHAPTER 1

THE MOBILE PET/SPECT SYSTEM

1.1 Purpose of the System

An economical and mobile bedside PET/SPECT system has been designed that can move within a hospital to image critically-ill patients, for example, those in intensive care unit (ICU) or emergency room (ER) settings. Because of their medical condition, these patients cannot easily be transported to a conventional single photon emission computed tomography (SPECT) or positron emission tomography (PET) facility. Currently in an ICU or ER, patients with known or suspected severe coronary artery disease typically must be managed without the benefit of myocardial perfusion or viability imaging studies to assess patient condition.

1.2 Nuclear Medicine

Nuclear medicine is unique in that it can show physiological processes that are occurring in the body and not just anatomical features, as in planar radiography, fluoroscopy, or computed tomography (CT). The two most commonly used modalities are PET and SPECT.

Functional imaging is fundamentally different from anatomical imaging in that the images are obtained from emission photons as opposed to transmission photons. Emission photons originate inside the patient and are detected outside the patient while transmission photons are emitted from one side of the patient and the unattenuated photons are detected on the opposite side.

In an emission image, a molecule or compound is designed to be uptaken into a specific organ of interest. The compound is tagged with a radioactive isotope and injected into the patient. The patient is then held for a period of time while the compound collects in the tissue or organ of interest. After this uptake period, the patient is positioned on the scanner and an acquisition is performed. As the isotope decays, the emitted photons are detected by gamma

cameras outside the patient. The amount and location of the detected activity is an indicator of how that organ is functioning. Functional images can be planar but the majority of nuclear medicine images currently are three dimensional (3D) as in PET or SPECT.

1.2.1 Positron Emission Tomography

Typical clinical PET systems are made up of a ring of detectors that surround the patient. Before the scan, the patient is injected with a positron emitter, typically ^{18}F -fluoro-deoxy-glucose (^{18}F -FDG), which will be metabolized by active tissue in the patient. The ^{18}F -FDG (or other positron emitting compound) will decay, emitting a positron which will undergo an annihilation reaction. Each annihilation reaction produces two 511 kilo-electronvolt (keV) photons emitted at 180 degrees ($^{\circ}$) from each other to conserve momentum. These two photons exit the patient and are detected in the ring of detectors. Timing circuits in the system pair the detector locations where each annihilation photon interacted. This is termed a coincidence event and by connecting the two paired detectors, a line of response containing the location of the annihilation event is determined. By recording all of the lines of response, a 3D image showing the location of the metabolized ^{18}F -FDG can be reconstructed.

1.2.2 Single Photon Emission Computed Tomography

In SPECT imaging, the patient is injected with a compound tagged with a gamma emitter that will be preferentially uptaken into the tissue of interest. The most common is $^{99\text{m}}\text{Tc}$ methoxy-isobutyl-isonitrile ($^{99\text{m}}\text{Tc}$ sestamibi), which is uptaken into the myocardium (heart muscle). The gamma ray that is emitted is detected by gamma cameras that rotate around the patient as opposed to the stationary ring of detectors in a PET scanner. The 2D image acquired at each angle is called a projection. To achieve full angular coverage, the detectors must acquire through at least 180° . As the number of projections obtained through this angular range is increased, the quality of the image also increases. Unlike PET imaging where

the collimation determining lines of response is electronic through timing circuitry, in SPECT, each detector has a lead collimator, typically parallel hole, which only allows gamma rays to interact in the detector from a known line of response. After the detector has obtained enough projection images around the patient, a 3D image can be reconstructed using the known lines of response.

1.3 Clinical Uses for PET and SPECT

Clinically, PET scans using ^{18}F -FDG (^{18}F -FDG-PET) are most often used to detect tumors and to examine the effects of cancer therapy. The reason for using PET to detect and monitor cancer is that ^{18}F -FDG is a metabolism tracer. Tumors readily uptake the tagged glucose tracer because of their rapid growth rate and demonstrate high contrast in a PET image. Although tumor detection is the most common, PET imaging is versatile and is not limited to cancer patients. Using different radiotracers, PET images of the brain can be used to evaluate patients who have memory disorders of an undetermined cause or seizure disorders that are not responsive to therapy. ^{18}F -FDG-PET imaging also helps evaluate signs of coronary artery disease, called viability imaging. Myocardial viability studies allow for the differentiation of nonfunctioning heart muscle from heart muscle that could benefit from a medical procedure such as an angioplasty or coronary artery bypass surgery to reestablish adequate blood flow and improve heart function.

As with PET, clinical SPECT imaging is also versatile. Studies include bone scans and brain scans but the most common SPECT procedure is myocardial perfusion imaging. Myocardial perfusion imaging is used to determine the condition of the patient's heart muscle. The procedure involves injection of $^{99\text{m}}\text{Tc}$ sestamibi in two separate studies; one under stress and one at rest. For the stress study, the patient is subjected to physical or pharmacological stress just prior to radiopharmaceutical injection to obtain an indicator of perfusion during periods of

increased myocardial activity. The rest study is used as an indicator of myocardial viability where low perfusion indicates non-viable tissue and high perfusion indicates viable myocardial tissue that can be re-vascularized, similar to an ^{18}F -FDG viability study using a PET scanner. The amount of blood flowing to the myocardium can be determined because the $^{99\text{m}}\text{Tc}$ uptake is proportional to the instantaneous myocardial perfusion. Regions of the myocardium that show reduced blood flow in the stress test but appear normal in the rest study are termed ischemic. For some patients, it is required to do both myocardial viability and perfusion studies.

1.4 Mobile Nuclear Medicine Systems

It is common for immobile patients to receive transmission images such as C-arm fluoroscopy or a mobile radiograph which can be brought directly to the bedside. On the other hand, for a patient to receive a routine nuclear medicine examination (PET or SPECT), that patient must be transported to the nuclear medicine department and positioned on one of the scanners. Because of this requirement, immobile patients with suspected coronary artery disease must be treated without the benefit of a simple nuclear medicine scan. This deficit in patient treatment has been the motivation to develop a mobile system that would be able to move to the bedside of immobile patients to perform functional imaging along with the anatomical imaging currently provided by mobile x-ray tubes.

Several attempts at developing a mobile nuclear medicine system based on the principle of ectomography have been documented in the 1990s [1]-[3]. Ectomography uses a single detector head at a single projection angle and a collimator that rotates throughout the acquisition. The major problem with this method is the requirement of a converging collimator which suffers from spatial resolution loss as depth increases. Not only did these collimators experience depth resolution issues, but the ideal slant angle for cardiac imaging was 40° and manufacturing

techniques only allowed a maximum angle of 30°. Due to these challenges, attempts at designing mobile systems implementing ectomography were abandoned.

More recently, the Segami Corporation (Columbia, MD 20588) has developed the “Nomad”, a commercially available mobile SPECT system specifically designed for cardiac imaging. Although this system is mobile, its design requires moving the patient out of bed and positioning them in a chair on the mobile system. This might work for some patients but still does not allow for imaging of truly immobile patients.

These systems show potential for mobile nuclear medicine but at the same time they are optimized for imaging at a single energy and only in SPECT mode. These specific design characteristics limit their usefulness in a clinical environment and are not as economical as they could be.

1.5 Multi-modality Nuclear Medicine

As an answer to the rising cost of imaging systems, Pichler, *et al.* proposed a multi-modality PET/SPECT system using a Sodium Iodine/Lutetium Orthosilicate (NaI/LSO) phoswich scintillator capable of imaging at different energies while still providing high resolution and sensitivity [4]. Although this system was not mobile, it showed that combining two imaging modalities can be more economical than purchasing the two separate systems. Furthermore, the flexibility of being able to perform different studies on a single system is beneficial and saves time and money since multiple studies can be obtained during a single trip to the scanner.

1.6 Our Mobile System Design Goals

We designed our system to counter the deficits in previous designs. To overcome the problem of imaging truly immobile patients, the system was designed to be compact and mobile to maneuver to a patient’s bedside. We also designed the system with dual detector heads to be

capable of imaging in SPECT mode with one or both of the heads orbiting the patient or in PET mode with the detector heads in an opposed orientation. The detectors were designed to be able to image at multiple energies to include the lower energy SPECT photons and the high energy annihilation photons for PET which makes the system versatile and economical. To meet all of these goals, concessions had to be made in the scintillating crystal material resulting in lower sensitivity at high energies, a limited field-of-view, and reduced spatial resolution when compared to a dedicated clinical system.

An economical mobile imaging system of this nature is not expected to achieve the same image quality of conventional SPECT or PET systems, particularly when the mobile system is designed for both 140 keV and 511 keV imaging in both PET and SPECT mode. Our goal was not to match the performance of a clinical system but to detect moderate to severe myocardial defects in immobile patients with both perfusion and viability imaging. The targeted spatial resolution for this system was 1.5 – 2.0 centimeters (cm) in the reconstructed image.

Conventional systems can achieve better spatial resolution (and other performance parameters), but these systems are often not a viable option for patients in an ICU or emergency room. The versatility of our system overcomes the deficits in spatial resolution and sensitivity by allowing different nuclear medicine study to be performed on a patient without moving the patient. It also saves money by not requiring the purchase of multiple scanners. All these issues will be discussed further in chapter 3.4.

1.7 511 keV SPECT

Because of the system's ability to image different energies, another option we have considered for cardiac imaging is to use ^{18}F -FDG as the radiotracer but use the system in SPECT mode instead of a PET mode (see chapter 2.3). Previous studies on myocardial ^{18}F -FDG-SPECT show that on the basis of regional ^{18}F -FDG uptake and defect scores (a visual four-point scale

that indicated the presence of absence of a defect in the left ventricular myocardium); ^{18}F -FDG-SPECT using ultra high energy collimators can be used for assessment of myocardial viability as accurately as ^{18}F -FDG-PET [5]. Using appropriate intensity thresholding, it was shown in phantom studies that ^{18}F -FDG-SPECT can be used to measure defect size as accurately as conventional PET [6]. Based on these prior studies, it can be seen that ^{18}F -FDG-SPECT can be used effectively for myocardial imaging by designing an appropriate high energy collimator. We suspect the reduced sensitivity of the system from absorptive rather than electronic collimation and the high photon energy can be partially compensated by longer scan times in ICU applications.

CHAPTER 2 SYSTEM DESIGN

2.1 Detectors

Our mobile system consists of two compact detectors, each with approximately $25 \times 25 \text{ cm}^2$ detector areas, mounted on a mobile gantry with a detachable computer and electronics rack (Figures 2-1 and 2-2). The electronics rack is 62 cm (24.5 inches (in)) deep, 66 cm (26 in) wide, and 1 meter (m) (39 in) tall. The detectors (fabricated at Thomas Jefferson National Accelerator Facility [7]) consist of pixilated NaI(Tl) ($5.0 \times 5.0 \times 12.5 \text{ mm}^3$ with 5.5 millimeter (mm) pitch). The photomultiplier tube (PMT) readout uses position-sensitive PMTs with high-rate four analog outputs arranged in a 4×4 array for each detector to form the $25 \times 25 \text{ cm}^2$ active detector area (Figure 2-3). A detailed description of the detector electronics and signal processing can be found in [7].

We needed a scintillator material that enabled a compact and economical imager for both $^{99\text{m}}\text{Tc}$ and positron tracers (including ^{18}F). Three possible scintillator materials were tested by Raylman *et al.* to compare spatial resolution and sensitivity: NaI(Tl), gadolinium oxyorthosilicate (GSO), and lutetium-gadolinium oxyorthosilicate (LGSO) [8]. The NaI(Tl) crystal produced the best energy resolution but had the worst spatial resolution and lowest detection sensitivity. The GSO crystal had the worst energy resolution and fell between the other two materials in terms of spatial resolution and detection sensitivity. The LGSO crystal produced the best sensitivity and spatial resolution and was only inferior to NaI(Tl) in terms of energy resolution. In spite of the lower detection efficiency and spatial resolution, NaI(Tl) was chosen in this system design due to its lower cost and its superior performance in imaging 140 keV gamma emissions. As stated earlier, we anticipate that this low detection efficiency at high energies can be partially compensated by longer scan times in ICU applications.

2.2 Gantry

The custom gantry system, manufactured by Accelerated Development Solutions (Phillipsburg, NJ 08865), has been designed to position the two detectors for tomographic imaging under the challenging conditions imposed by the ICU or emergency room environments. The gantry is built on a standard palate jack with 8 cm (3 in) low profile legs that slide beneath ICU beds for stable support, as shown in the computer-aided design drawings in Figure 2-4. The base is 1.47 m (58 in) long and 75 cm (29.5 in) wide. The detectors mount to the rails of a linear bearing set that allows precise horizontal and vertical detector motion. Vertical detector motion is motor-driven using electronic motion control modules and the horizontal motion is controlled manually. The height of the gantry is 1.97 m (77.5 in). Detector pivoting provides the additional, necessary motion dimension for tomographic imaging. The linear motions and pivot angle are digitally encoded for input to the reconstruction software and can be readout on the gantry.

2.3 Detector Positioning

Although this system is capable of acquiring coincidence PET data from the two detectors in an opposed orientation (Figures 2-4A, and 2-4B), the 511 keV SPECT approach using high energy collimators and acquiring projections over the anterior 180° (Figures 2-1 and 2-5) has two advantages despite the reduced detection sensitivity from absorptive rather than electronic collimation.

First, projection data with complete angular sampling (anterior 180°) are more readily achieved with SPECT mode compared with PET mode (Figure 2-5). The latter mode requires positioning and orbiting a detector beneath the patient bed and it might not be feasible to rotate a detector beneath the bed to achieve full angular sampling due to the obstruction from support structures and the thickness of the mattress [9]. Second, the effects of attenuation and scatter in

the patient are greatly reduced with 511 keV SPECT for cardiac imaging using 180° anterior data relative to PET, which has attenuation effects from the entire thickness of the patient.

2.4 System Operation

Tomographic acquisitions with this system require manual detector positioning at each projection angle. The horizontal and vertical location of the detector head along with the detector angle must be recorded at each projection angle for post-processing to eliminate anatomy truncation in the final reconstructed image (see chapter 4.2.4).

Software on the system computers provides the energy normalization and a linearity correction before data are output. In PET mode, software also processes the coincidence data. The data are output in listmode where each event in SPECT mode is represented by 14 bytes (2 bytes for the x pixel, 2 bytes for the y pixel, 2 bytes for the energy, and 8 bytes for a timestamp) and every event in PET mode is represented by 12 bytes (2 bytes for the x pixel in detector 1, 2 bytes for the y pixel in detector 1, 2 bytes for the energy in detector 1, 2 bytes for the x pixel in detector 2, 2 bytes for the y pixel in detector 2, and 2 bytes for the energy in detector 2). The output image has 45×45 pixels and must be uniformity corrected after the acquisition using an intrinsic flood image that is obtained before the tomographic acquisition is started. A step-by-step manual of system operation can be found in Appendix A and the MATLAB code for post-processing can be found in Appendix B.



Figure 2-1. Various views of the mobile PET/SPECT imaging system. Detectors are shown in A) Left lateral and right anterior oblique orientation. B) Lateral orientation. C) Anterior-posterior orientation.

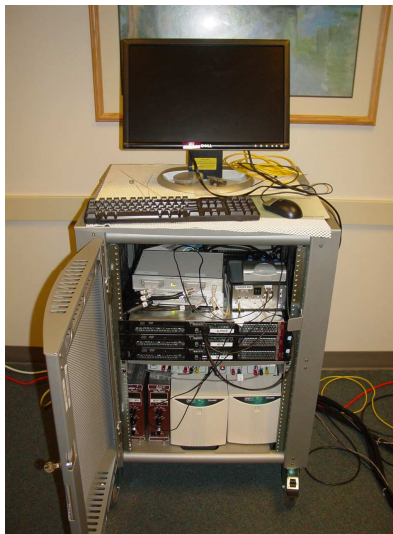


Figure 2-2. Front view of the associated electronics rack and computers for the mobile system.

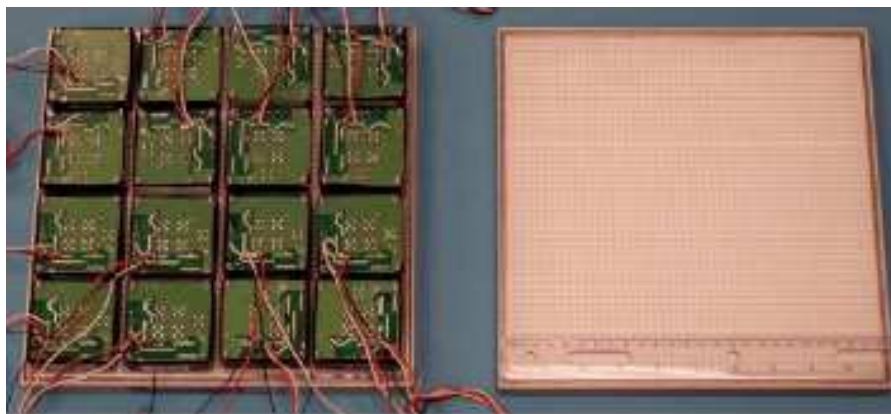


Figure 2-3. View of the detector head showing the 4x4 photomultiplier tube array and pixilated NaI crystal.

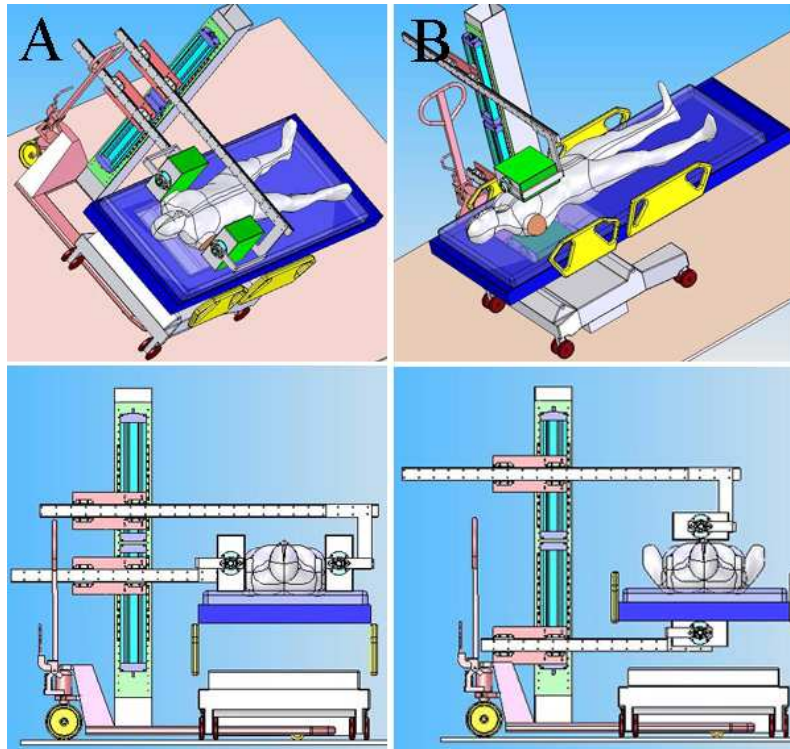


Figure 2-4. Computer-aided design drawings of the system gantry and the different detector positioning capabilities. A) Lateral view. B) Anterior-posterior view. Notice that the ICU bed arms move up and down to allow for detector positioning.

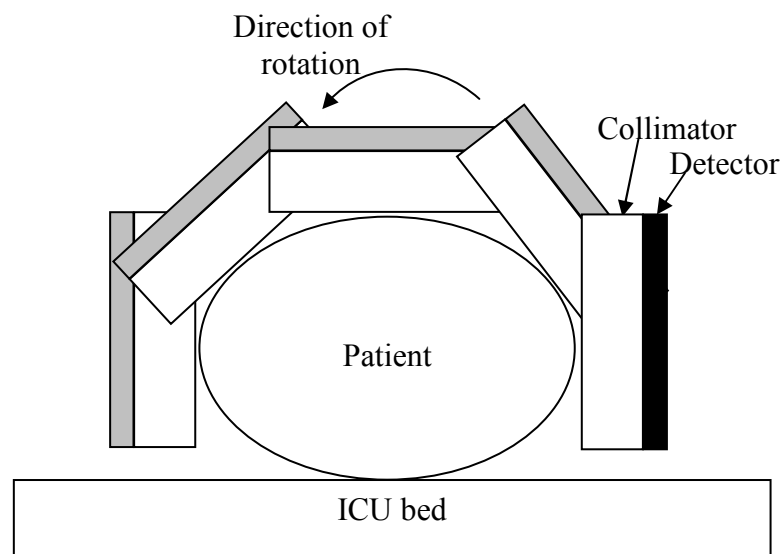


Figure 2-5. A single detector head fitted with a collimator can be used for single photon imaging to achieve complete angular sampling which might not be able to be achieved with a detector underneath the bed in PET mode.

CHAPTER 3 SYSTEM PERFORMANCE EVALUATION¹

3.1 Introduction

To begin the investigation the clinical feasibility of our system, a full performance evaluation was completed. Five imaging metrics were evaluated for both 140 keV and 511 keV SPECT imaging with this system; intrinsic energy resolution, spatial resolution (planar and reconstructed), detection sensitivity, count rate capability, and uniformity. These metrics test all aspects of system performance and allow for comparison to commercial systems.

3.2 Evaluation Methods

3.2.1 Energy Resolution

The energy resolution of the system was measured intrinsically (without a collimator) with a point source positioned 75 cm from the detector face and 1.0×10^7 total counts acquired for each source. Using this geometry, energy spectra of the point sources were obtained. An 80 micro-Curie (μCi) source of $^{99\text{m}}\text{Tc}$ (140 keV) was imaged at the detector's low energy setting and a 240 μCi source of ^{18}F (511 keV gamma) was imaged at the high energy setting. These radioactivity levels were low enough to ensure that the detector did not exceed the maximum count rate.

To determine a keV/channel calibration factor for each energy setting, a 5 μCi source of Cobalt-57 (^{57}Co) (122 keV gamma emission) was imaged at the low energy setting and a 65 μCi source of Cesium-137 (^{137}Cs) (662 keV gamma emission) was imaged at the high energy setting. The peak channel for each of these sources was recorded and a keV/channel factor was obtained for each energy setting by comparing the peak channels of the two different sources at each respective energy setting. This calibration factor was used to convert the measured energy resolution (full-width-half-maximum (FWHM) in channels) into keV units. The photopeak

¹ © IEEE 2009. Reprinted with permission from (M. T. Studenski, "Performance evaluation of a bedside cardiac SPECT system," *IEEE Trans. Nucl. Sci.* (Accepted for publication on 1/12/2009)).

FWHM was measured without curve fitting due to the low noise and fine sampling (channel width less than FWHM/100) of the energy spectrum. The maximum was taken to be the peak value and the full-width was found by linear interpolation of the two closest half maximum channels on each side of the photopeak.

3.2.2 Spatial Resolution

The intrinsic planar spatial resolution of the system at 140 keV and 511 keV was measured using a 5 cm thick, 1 mm wide lead slit phantom with ^{99m}Tc (190 μCi) and ^{18}F (160 μCi) point sources. The sources were positioned 75 cm from the detector face, and 5.0×10^6 counts were obtained for both energies. Count rate was substantially below the system maximum. The intrinsic spatial resolution was measured and averaged over three acquisitions with the slit phantom translated in 1 mm increments perpendicular to the slit. This was done in order to average out potential variation in the measured spatial resolution due to the position of the slit position relative to the detector grid.

The system planar spatial resolution at 140 keV and 511 keV was evaluated using low and high energy collimators, respectively. The collimator parameters are given in Table 3-1. The theoretical septal penetration level for the high energy collimator at 511 keV is 7% using the formula from [10], which is slightly greater than the conventionally used level of 5%. This 5% level could have been met but would have increased the collimator weight substantially. The decision to reduce the weight and allow more penetration was done realizing that manual positioning of the detectors was required during an acquisition and a heavy collimator makes this difficult.

The actual planar spatial resolution was measured from line source images acquired using 1 mm inner diameter capillary tubes containing either 500 μCi of ^{99m}Tc or 200 μCi of ^{18}F with an energy window of 30% for ^{99m}Tc and 20% for ^{18}F . Images with 5.0×10^5 total counts were

obtained at distances of 10 cm, 20 cm, and 30 cm from the collimator face and in both x and y orientations. Profiles were taken across the images to obtain line spread functions (LSF) at each distance, and the FWHM was measured. For the 511 keV case, the FWHM was measured both with and without subtracting a constant from the LSF to reduce the effect of the septal penetration “tails” in the measured LSF. This constant, 0.18, was computed from the average intensity of twenty pixels not contained in the peak. The reported FWHM was the average of the x and y directions. These results were then compared to the theoretical FWHM calculated using the effective length and diameter of the collimator holes and the distance from the collimator face [10]. In order to assess the level of septal penetration in the line source images, the full-width at tenth-maximum (FWTM) was also measured. Uniformity correction was applied to all the images acquired for spatial resolution measurements.

The reconstructed SPECT spatial resolution at 140 keV was measured using a point source of ^{99m}Tc (2.5 milli-Curies (mCi)) located at the tip of a syringe. The same measurement was performed at 511 keV using 250 μCi of ^{18}F . A total of 19 projections (every 10° from 0° – 180°) with 5.0×10^5 counts per projection and a 20% energy window were obtained. The activity in the syringe was centered in the detector field-of-view with a radius of rotation of 22 cm. The projections were reconstructed using the maximum likelihood-expectation maximization (MLEM) algorithm [11] with 50 iterations into a $45 \times 45 \times 45$ voxel image (5 mm^3 voxels). The iterative MLEM reconstruction algorithm was used because we have found this method to be superior to filtered backprojection (FBP) with a ramp filter in terms of reducing streak artifacts when projection angular sampling is somewhat coarse, as in this case. The system model within the MLEM algorithm assumed ideal spatial resolution, so there was not any spatial resolution enhancement through image processing. The number of iterations, 50, was chosen based on the

fact that the change in the reconstructed spatial resolution at greater iteration numbers was negligible. A profile was taken across a transaxial and coronal slice of the reconstructed image and from this, the FWHM was measured.

The effect of projection angle sampling was not studied in this chapter. Theoretically, it has been noted that the required number of angular samples changes linearly with the linear sampling distance and inversely with the field-of-view (FOV) size [12]. Comparing the FOV of this system (25 cm) to that of a traditional system (typically 50 cm), the required number of angular samples with this system is reduced by a factor of two relative to a traditional SPECT system. This theory will be addressed in chapter 4.

3.2.3 Detection Sensitivity

The extrinsic (with a collimator) detection sensitivity in terms of counts/ $\mu\text{Ci/s}$ was evaluated using point sources of 240 μCi $^{99\text{m}}\text{Tc}$ and 170 μCi ^{18}F suspended 15 cm from the collimator face. Each acquisition was 300 seconds (s) with an energy window twice the width of the FWHM of the photopeak. For the $^{99\text{m}}\text{Tc}$ case, the measured sensitivity was obtained by summing the counts over the entire detector surface. For the ^{18}F case, in order to get a more meaningful measure of sensitivity that excluded uncollimated photons, the measured sensitivity was obtained by summing over a 35 cm^2 circular region-of-interest (ROI) centered on the peak image intensity. This ROI was chosen subjectively; in practice it is impossible to eliminate all penetrating photons while including all collimated photons with a single ROI. To quantify the effect of different ROI sizes on the sensitivity measurement, a second, 45 cm^2 circular ROI was also measured.

To investigate the non-uniformity in detection sensitivity over the detector surface, the sensitivity measurements for both energies were obtained with the point sources located at five

different positions across the detector field-of-view. The positions were chosen in an attempt to sample the full range of sensitivity variation based on the detector count rate readout.

A discrepancy was observed between the predicted and measured sensitivity for the ^{99m}Tc case. In order to further investigate this effect, additional detection sensitivity measurements were performed with ^{99m}Tc using the high energy collimator.

3.2.4 Count Rate Capability

The detector count rate performance for 140 keV and 511 keV was evaluated using point sources with 535 μCi of ^{99m}Tc and 1.1 mCi of ^{18}F . Each source was suspended 30 cm from the detector face and 20 s acquisitions were obtained while the source decayed through several half lives. The counts per second (cps) minus background integrated over the entire detector surface was recorded at each time point. For this acquisition no out-of-field activity was used.

3.2.5 Flood Field Uniformity

Flood field uniformity was evaluated using the images that resulted from the energy resolution measurements. The images are presented both with and without linearity correction. The linearity-corrected flood image is used for uniformity correction in the measured projection images.

3.2.6 Phantom Acquisition

The performance of this system was further assessed based on SPECT image quality using an anthropomorphic, dynamic cardiac phantom (Model ECT/DY-CAR/P, Data Spectrum Corp. Hillsborough, NC 27278). The phantom contains simulated lungs, spine, liver, and myocardium and will be described in more detail in chapter 4.2.1. Both ^{99m}Tc and ^{18}F studies were performed using approximately 1 mCi injected into the simulated myocardium. There was no activity placed outside of the myocardium. The phantom heart rate was 72 beats per minute (BPM); the ejection fraction (EF) was 45%. As with the previous SPECT acquisitions, 19 projections were

acquired with 2.5×10^5 counts per projection which resulted in approximately 35 minute scan time. The energy window was 30% for ^{99m}Tc and 20% for 511 keV.

3.3 Results

3.3.1 Energy Resolution

The energy spectra from the ^{99m}Tc and ^{18}F images can be seen in Figure 3-1. Using the calculated keV/channel factors (0.27 keV/channel at 140 keV and 1.00 keV/channel at 511 keV), the measured FWHM was 43 keV (31%) for 140 keV and 108 keV (23%) for 511 keV. Low energy tails are absent from the ^{99m}Tc spectrum, and the photopeak is asymmetric. We suspect that this is due to the fact that the energy discrimination with this detector has been optimized for 511 keV and that a low energy cutoff is affecting photons in the lower half of the photopeak, between approximately 100 keV and 140 keV.

3.3.2 Spatial Resolution

The intrinsic spatial resolution was measured to be 5.6 mm FWHM at 140 keV and 6.3 mm FWHM at 511 keV. Figure 3-2 shows the normalized LSFs from the slit phantom images. Because the face of the detector was completely shielded except for the slit, we suspect the cause of the low intensity tails in the 511 keV LSF are from photons that penetrate through the lead in the slit phantom.

Figure 3-3 shows the normalized system spatial resolution LSFs from the capillary tube acquisitions at 140 keV and 511 keV. Each plot includes the measurements at 10, 20 and 30 cm from the detector face. For both energies, plots are shown for the x and y profile directions. The tails in the 511 keV LSFs can be attributed to collimator septal penetration.

Figure 3-4 shows line source images acquired at 10 cm from the detector face for both 140 keV and 511 keV. The effects of septal penetration are evident in the 511 keV image in the

region surrounding the line source. The septal penetration pattern is consistent with the commonly observed, six point star artifact with hexagonal hole collimators [13].

Table 3-2 summarizes the measured FWHM as a function of distance from the collimator, b, both with and without constant subtraction, the theoretical calculation, and the percent deviation of the measured from the theoretical. The table shows that the tails from septal penetration caused substantial increase in the measured FWHM and a closer agreement with the theoretical spatial resolution occurred after subtracting the constant. Table 3-2 also shows the FWTM results in which the effect of septal penetration with 511 keV photons is evident in the larger FWTM values.

Figure 3-5 shows the reconstructed SPECT image of the point source and the corresponding LSF obtained by integrating the intensity along columns in the image (and normalizing). The FWHM of the LSF at 140 keV was 1.59 cm in the transaxial plane and 1.57 cm in the coronal plane. This is in close agreement with the theoretical, planar system spatial resolution (1.59 cm), which is obtained using the standard formula from [10] for the low energy collimator at a distance from the collimator face equal to the radius of rotation used in the SPECT acquisition. For the 511 keV source, the FWHM was 1.58 cm in the transaxial plane and 1.74 cm in the coronal plane. These values also agree well with the theoretical resolution (1.59 cm).

3.3.3 Detection Sensitivity

Table 3-3 contains the results from the sensitivity measurements along with the predicted sensitivity calculated from geometric collimator efficiency, g, and intrinsic crystal efficiency at both energies [10]. To show the effect of the sensitivity non-uniformity over the detector surface, both the minimum and maximum values from the five measurements are included in the

table. The measurements using ^{18}F have two values from the two different sized ROIs; the first value is the sensitivity from the 35 cm^2 ROI and the second value is from the 45 cm^2 ROI.

The 511 keV measurements compared well with the predicted values. Some of the measured values were actually higher than the predicted values, which we suspect is due to the inclusion of uncollimated photons in the measurement. The 140 keV measurements are lower than predicted for both the low and high energy collimators. This discrepancy can largely be attributed to the reduced sensitivity in the regions between PMT's, which is represented by the minimum measured sensitivity in Table 3-3.

3.3.4 Count Rate Capability

Figure 3-6 shows plots of the detected count rate as a function of activity for $^{99\text{m}}\text{Tc}$ and ^{18}F . The maximum count rate in both of these curves was found near the left end of the plateau of these curves. The presence of a plateau is unlike the count rate curve of a typical paralyzable detector, which exhibits a more clearly defined maximum. The maximum count rate was measured to be 1.46×10^5 cps for $^{99\text{m}}\text{Tc}$ and 1.56×10^5 cps for ^{18}F . This maximum occurred at 135 μCi for $^{99\text{m}}\text{Tc}$ and 275 μCi for ^{18}F . The images and energy spectra were distorted when the detector count rate was saturated.

3.3.5 Flood Field Uniformity

Figure 3-7 shows the uncorrected raw flood images acquired at both 140 and 511 keV, and Figure 3-8 shows the flood images after linearity correction. The 4×4 array of PMTs and the 45×45 pixel array can clearly be seen in the images. The degree of non-uniformity between the low intensity regions (between PMTs) and high intensity regions (within PMTs) is perhaps best quantified by the detection sensitivity minimum and maximum presented in Table 3-3. For 140 keV, the minimum and maximum regions differ by a factor of approximately 3.5; for 511 keV, they differ by a factor of approximately 2.

3.3.6 Phantom Acquisition

Figure 3-9 shows the reconstructed myocardium of the dynamic cardiac phantom in transaxial and coronal slices for the ^{99m}Tc and ^{18}F acquisitions. The ^{18}F images show artifacts in the form of extra-myocardial image intensities, which can be attributed to septal penetration effects. These effects result in a lower ventricle-to-myocardium contrast when compared to the ^{99m}Tc images, as found previously [13]. Chapter 4 examines further studies with the phantom to assess the effects of out-of-field activity, angular sampling, and counts per projection; issues that are important for the environment in which we expect to use this system.

3.4 Summary and Discussion

Our design goal for the performance of this mobile system was not expected, nor designed, to match that of a conventional SPECT system. The design of this camera, including a pixilated NaI crystal and position-sensitive PMTs, was chosen to allow a compact design with effective imaging closer to the edge of the camera. This will be advantageous for future PET imaging, which will require a detector to be positioned beneath the bed. For solely anterior, 180° SPECT, it may be that conventional camera designs will work effectively in the bedside environment with potentially improved system performance. In spite of the inferior performance relative to conventional systems, this bedside system may still provide images of sufficient quality to aid in patient management. For example, severe cardiac disease can be readily apparent in cardiac ^{99m}Tc and ^{18}F -FDG images and does not necessarily require a gamma camera or PET system with ultra-high spatial resolution and detection sensitivity.

In terms of energy resolution, the measured values (31% for 140 keV and 23% for 511 keV) were worse than typically found for conventional SPECT systems. Current systems using NaI scintillators can achieve an energy resolution of around 10% at 140 and 511 keV [14], [15], but adding a pixilated crystal and the position sensitive PMTs can degrade the resolution to 18%

[4]. Other systems using LSO and bismuth germanate (BGO) scintillators at 511 keV can achieve an energy resolution of about 18% and 22%, respectively [4], [14]. We are not aware of any fundamental reason why the energy resolution should be worse than a conventional gamma camera. The degraded energy resolution is expected to impact scatter rejection and, as a result, the detectability of myocardial defects to some degree.

In order to reduce costs and because ultra-high spatial resolution was not a design goal, this system uses a NaI crystal with 5 mm pixels. At a higher cost, a different material, such as cadmium zinc tellurium (CZT) or lanthanum bromide ($\text{LaBr}_3:\text{Ce}$) with much smaller pixels could be used, which would improve both spatial resolution and energy resolution [16].

Gains could be made in the sensitivity of the system by matching the collimator pitch to the crystal pitch [17]. To reduce expenses with the system, using a traditional hexagonal hole collimator was more efficient than having a custom made square hole collimator that matched the pixel pitch. The larger size of the pixels in this system compared to other systems was another reason to choose the traditional hexagonal collimator.

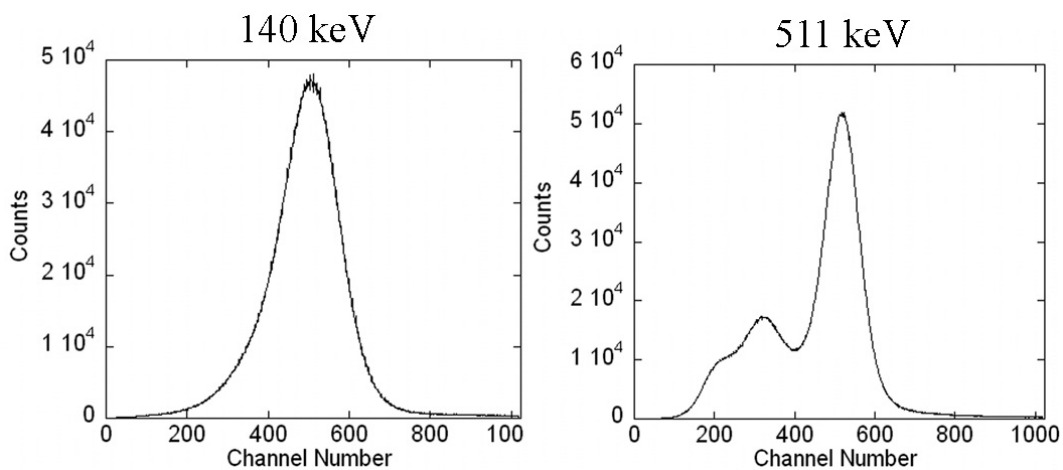


Figure 3-1. Energy spectra obtained from 140 keV and 511 keV point sources.

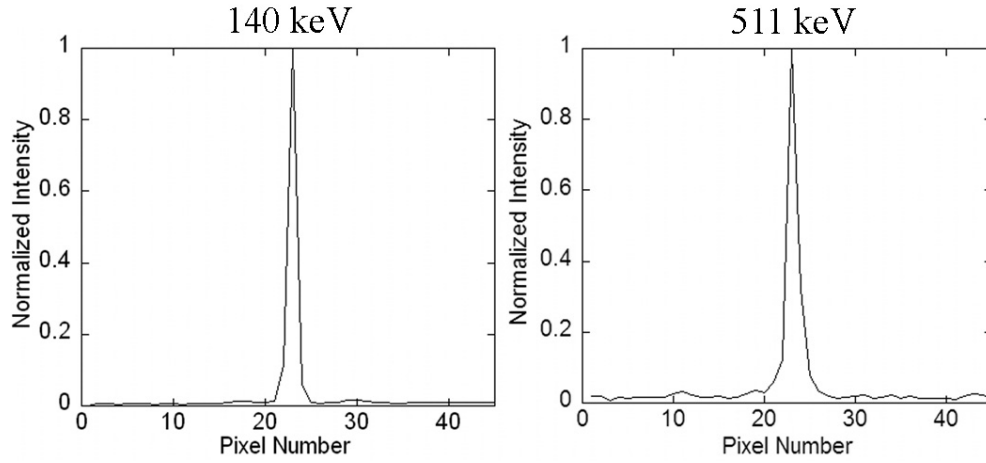


Figure 3-2. Normalized intrinsic spatial resolution LSFs with ^{99m}Tc (140 keV) and ^{18}F (511 keV).

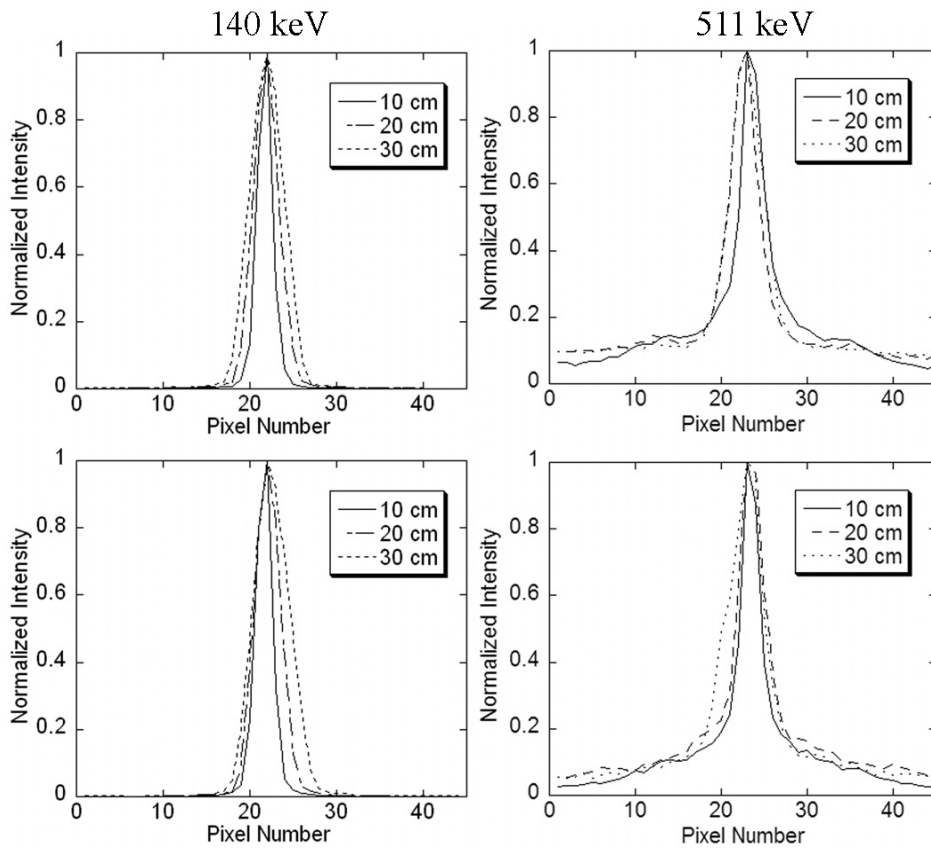


Figure 3-3. Normalized system spatial resolution LSFs at 10, 20, and 30 cm from the detector face for both 140 keV and 511 keV. The LSFs are shown in both the x direction and the y direction for both energies.

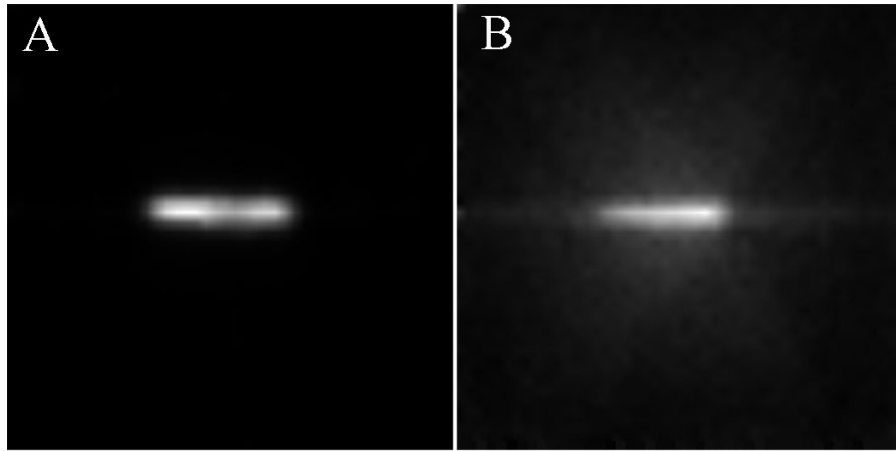


Figure 3-4. Line source images for system spatial resolution measurements. A) 140 keV. B) 511 keV. Line source to detector distance was 10 cm.

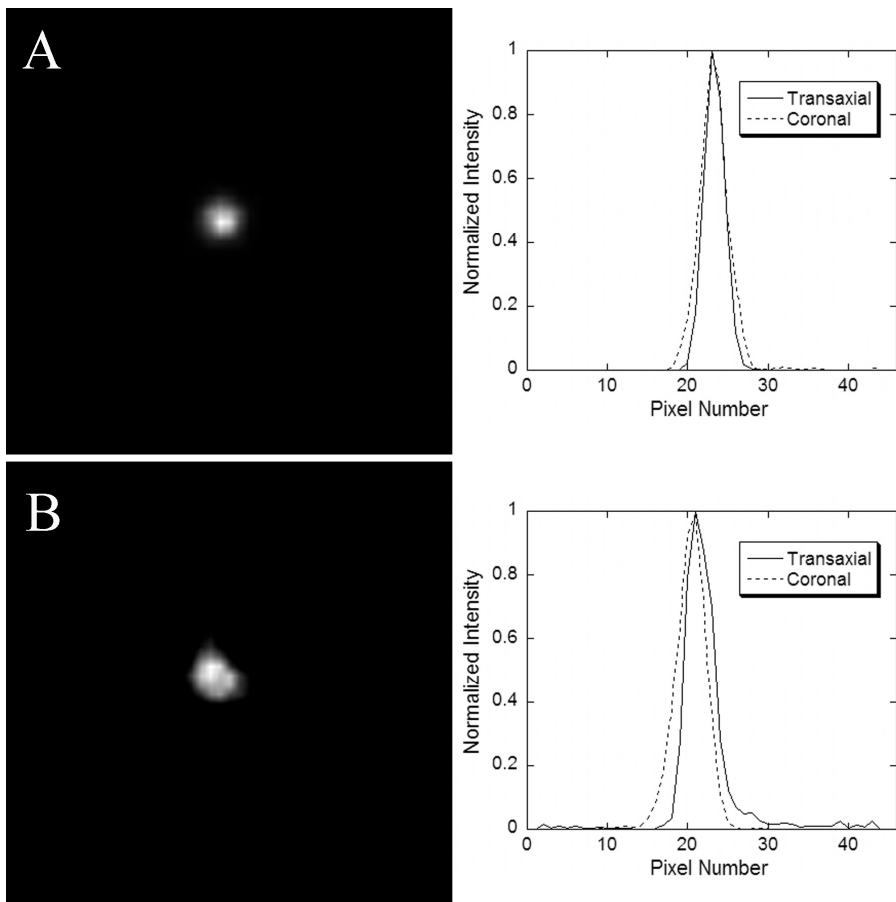


Figure 3-5. Coronal slices from reconstructed SPECT images with point sources and the corresponding point spread functions in both the transaxial and coronal planes. A) 140 keV. B) 511 keV.

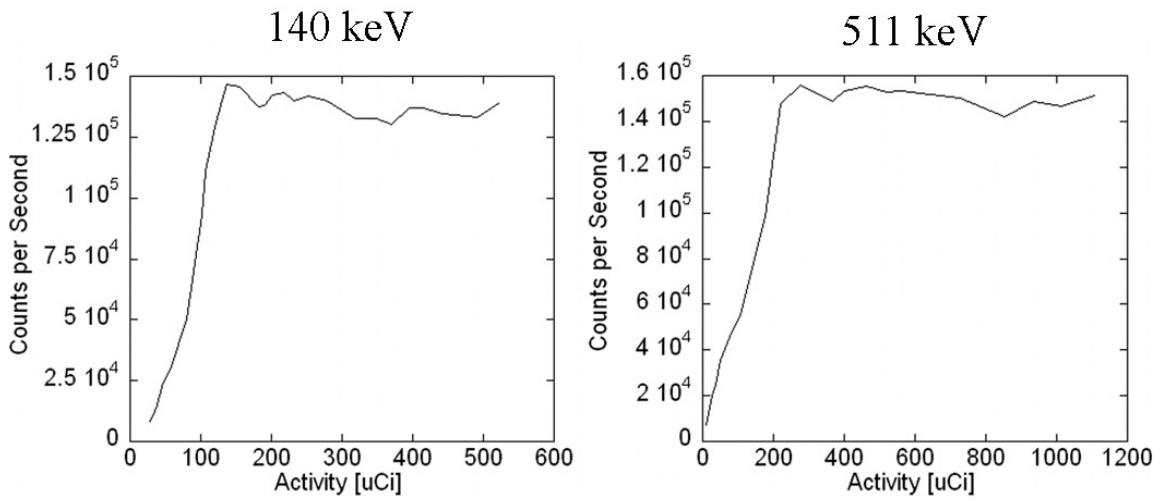


Figure 3-6. Count rate as a function of activity for 140 keV and 511 keV.

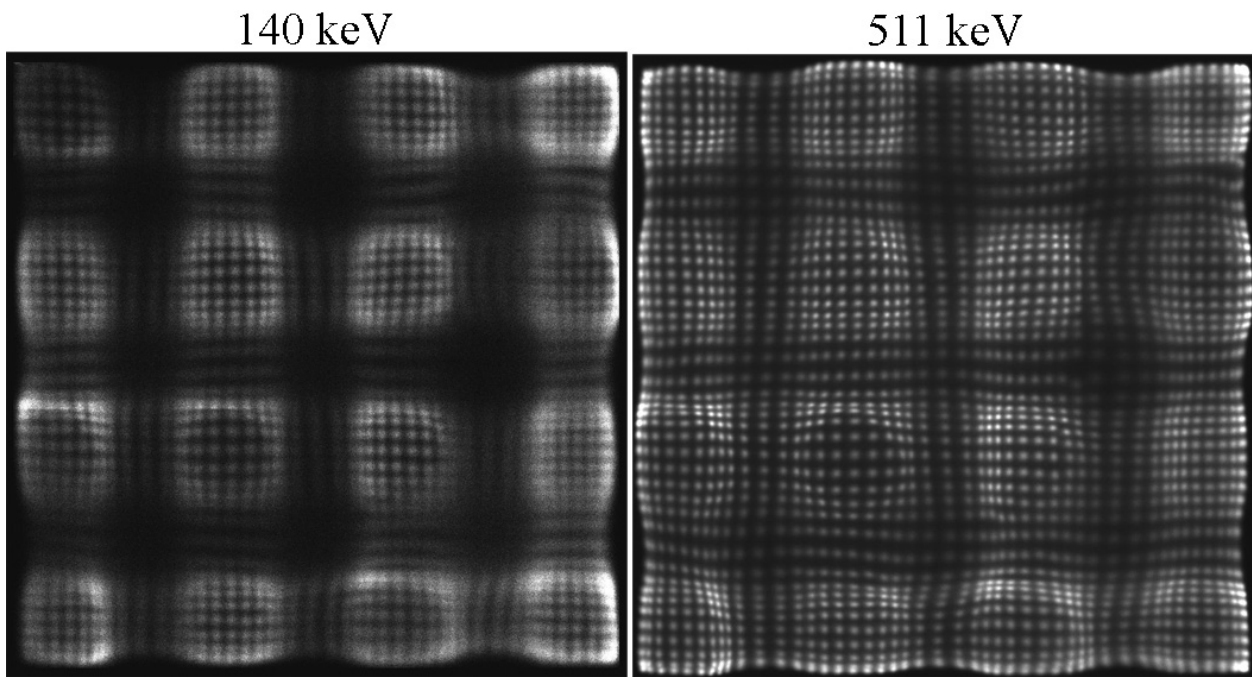


Figure 3-7. Raw, uncorrected flood images for both 140 keV and 511 keV energies.

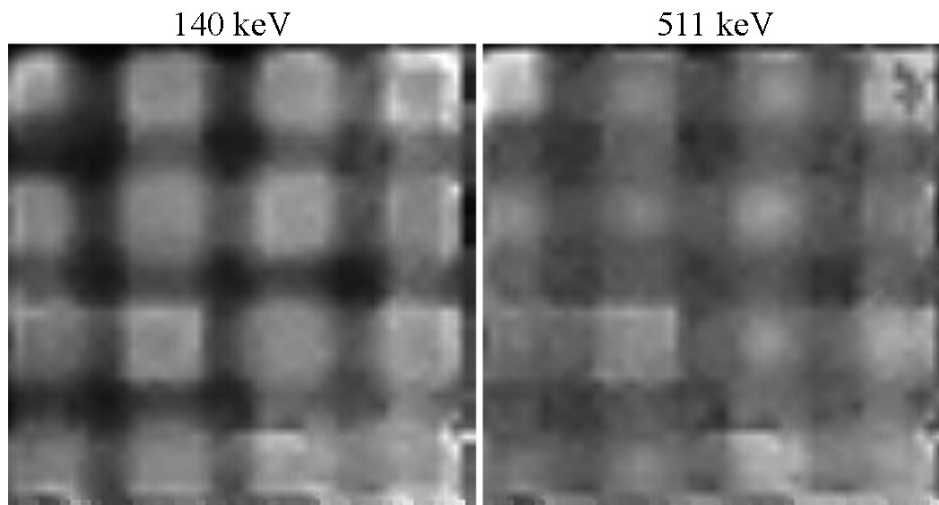


Figure 3-8. 45×45 pixel linearity corrected flood images for both 140 keV and 511 keV energies used to correct for uniformity in acquired images.

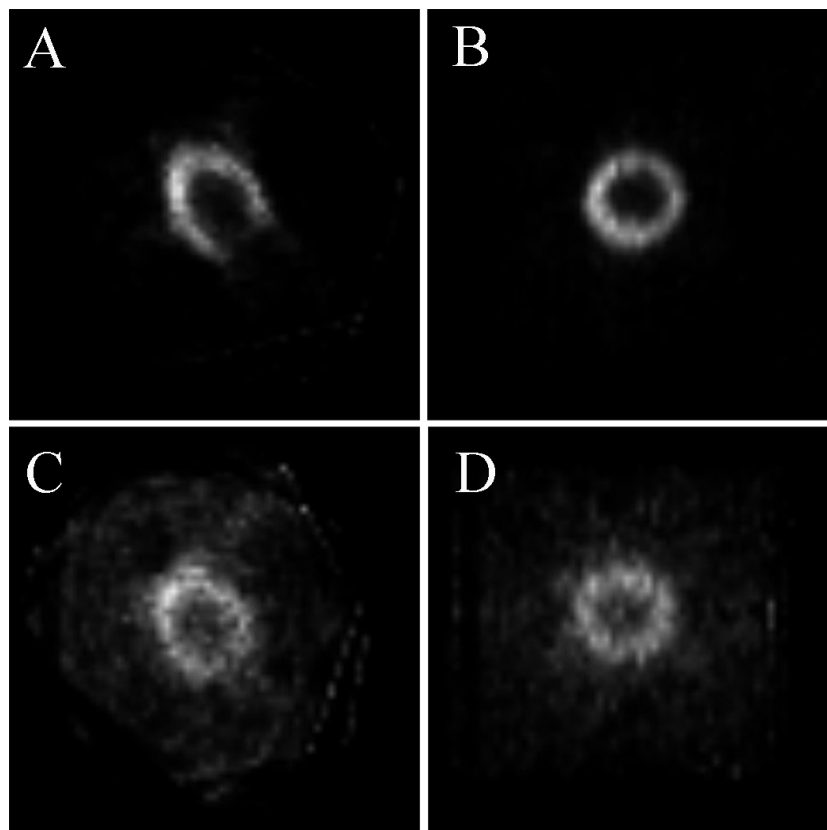


Figure 3-9. Reconstructed images from the dynamic cardiac phantom acquisitions with both ^{99m}Tc and ^{18}F . A) Transaxial slice at 140 keV. B) Coronal slice at 140 keV. C) Transaxial slice at 511 keV. D) Coronal slice at 511 keV.

Table 3-1. Low energy (140 keV) and high energy (511 keV) collimator parameters.

	Low energy	High energy
Hole shape	Hexagonal	Hexagonal
Collimator thickness [cm]	2.3	4.9
Hole diameter [mm]	1.5	2.3
Septal thickness [mm]	0.2	2.02

Table 3-2. System spatial resolution.

Energy	b [cm]	FWHM [cm]				FWTM [cm]
		w/o subtraction	With subtraction	Theoretical 1	% Deviation	
140 keV	10	1.14	-	0.99	14.7	2.16
	20	1.64	-	1.59	3.1	3.16
	30	2.35	-	2.23	5.4	4.12
511 keV	10	1.52	1.23	1.05	44.8 / 17.1	12.06
	20	2.04	1.68	1.59	28.3 / 5.7	13.42
	30	2.47	2.10	2.06	19.9 / 1.9	13.62

Table 3-3. System sensitivity.

Source energy and collimator	Predicted [cts/ μ Ci/s]	Measured [cts/ μ Ci/s]		
		Min.	Max.	Avg.
140 keV w/ low energy	8.57	1.73	6.06	4.15
140 keV w/ high energy	1.55	0.3	0.92	0.55
511 keV w/ high energy	0.92	0.40 / 0.93	0.87 / 1.14	0.67 / 1.06

CHAPTER 4 IMAGE ACQUISITION AND PROCESSING METHODS²

4.1 Introduction

Here, we further the clinical feasibility evaluation by considering reconstructed image quality using an anthropomorphic dynamic cardiac phantom to simulate a more realistic source distribution and out-of-field activity (Figure 4-1).

Three key factors for the imaging system are specifically addressed in this chapter; 1) mitigating the effects of septal penetration photons for the 511 keV SPECT data, 2) reducing truncation effects due to the relatively small field-of-view (FOV) of the detector, and 3) investigating the effects of reduced angular sampling and angular range.

To compensate for septal penetration effects, we used a Metz de-convolution filter which incorporates the measured 2D modulation transfer function (MTF) including septal penetration effects. The underlying assumption is that the septal penetration effects in the measured data can be modeled as a linear, spatially-invariant process. This method of septal penetration compensation was investigated previously for indium-111 (^{111}In) and iodine-123 (^{123}I) imaging by King *et al.* [18].

Due to the relatively small FOV of the detectors, truncation can arise in the tomographic image, particularly in regions distant from the axis-of-rotation. In order to overcome this problem, at each projection angle during the acquisition, the detector is translated tangentially to maintain the heart near the center of the FOV. This is effectively an angle-dependent center-of-rotation (COR) shift that is recorded and modeled in the reconstruction.

² This chapter is currently under review for publication in IEEE Transactions on Nuclear Science (M. T. Studenski and D. R. Gilland, "Acquisition and processing methods for a bedside cardiac SPECT imaging system," *IEEE Trans. Nucl. Sci.* (submitted 10/30/2008)).

In this chapter we investigate the effects of angular sampling and angular sampling range on the resulting reconstructed image. The smaller reconstructed FOV of this system should require less angular sampling than conventional SPECT systems [12]. We would like to determine the minimum number of angular samples required since detector positioning with this prototype system is done manually. The investigation of the reduced angular sampling range (i.e. less than 180°) is motivated by our expectation that for applications such as ICU bedside imaging, it may be difficult to obtain quality lateral views of the patient if they are not capable of lifting their arms.

4.2 Methods

4.2.1 Experimental Phantom

The dynamic cardiac phantom (Figure 4-1) consists of a water filled torso, a beating heart comprised of an inner and outer latex membrane, two lungs filled with one part water and two parts Styrofoam beads to simulate the density of the lungs, a Teflon spine, and a water filled liver. The volume contained between the two membranes of the beating heart can be filled with ^{99m}Tc to simulate a myocardial perfusion study or with ^{18}F to simulate a myocardial viability study. A computer controlled pump is used to expand and contract the myocardium and values for stroke volume, ejection fraction, and beats per minute (BPM) can be input to the controlling computer. For this investigation, the phantom was programmed for 72 BPM, 45% ejection fraction (EF), and 55 milliliter (mL) stroke volume.

For both the ^{99m}Tc and ^{18}F studies, the phantom myocardium was filled with approximately 1 mCi of activity and the phantom liver (1700 mL) was filled with approximately 2 mCi of activity. For the ^{18}F studies, in order to isolate the effects of out-of-field activity, additional acquisitions were performed with no activity in the liver.

4.2.2 Data Acquisition

Acquisitions consisted of 37 projection angles equally spaced over 180° . The energy window was 20% centered on the photopeak. Relatively high count, low noise projection data were acquired for both the ^{99m}Tc and ^{18}F studies, and a “count thinning” technique was used to generate lower count data from this high count data. For the ^{99m}Tc study, the high count data were obtained using an approximately 55 minute acquisition time, which resulted in 2.5×10^5 total counts per projection. The ^{18}F data was obtained using an approximately 80 minute acquisition time with approximately 3.0×10^5 total counts per projection. One change from the 37 projection angle protocol was that the ^{18}F acquisition containing out-of-field activity was done with 25 projection angles resulting in a 60 minute acquisition time.

In order to simulate the increased noise that results from shorter acquisition times, a “count thinning” technique was applied to the high count projection data [19]. This technique involves replacing each pixel value in the high count data with a sample from a binomial distribution with number of trials n equal to the high count pixel value and probability of success p equal to the desired scale factor. This is a convenient way to scale down the count level while maintaining the Poisson statistics of the measured data. The count thinning approach was used to scale down the projection data by factors of 2, 4, and 8.

4.2.3 Metz Filtering of the Projection Data

In the previous chapter, with planar images of an ^{18}F point source, we have observed low intensity “tails” due to septal penetration by the 511 keV photons. In order to conserve weight, the high energy collimator was designed with 49 mm long and 2.3 mm diameter hexagonal holes with 2.02 mm septa, which allowed a 7% penetration level rather than the conventional 5% [10]. To mitigate this septal penetration effect in this study, we filter the projection data prior to the reconstruction using a 2D Metz filter, which is a combination of a de-convolution and smoothing

filter [20]. The Metz filter function is given in Equation 4-1 where $MTF(v)$ is the 2D modulation transfer function and parameter X determines the extent to which the filter follows the inverse MTF before rolling-off to zero gain. We tested a range of values for X (50, 100, and 200) for the ^{18}F filter and negative values in the filtered images were set to zero.

$$Metz(v) = \frac{1 - (1 - MTF(v))^X}{MTF(v)} \quad (4-1)$$

The 2D MTF for the Metz filter was obtained from measured point spread functions using an ^{18}F point source (5 mm in diameter and 20 cm from collimator) and is shown in Figure 4-2 along with the point spread function from a similar ^{99m}Tc point source. The star pattern due to collimator septal penetration is evident and is not seen in the 140 keV point source image. We acknowledge that the MTF is distance dependent and we chose 20 cm as an average source-to-detector distance over all the projections covering 180° . We also tested the Metz filter on the ^{99m}Tc data to study its effect on the final reconstructed image. For the ^{99m}Tc projections, we tested the filter with values of 2, 5, and 10 for X .

The first step in processing the projection data was to obtain the MTFs for both ^{99m}Tc and ^{18}F . Figure 4-3 shows the MTFs along with horizontal and vertical profiles. From the calculated MTFs, the 2D Metz filter was created. Figure 4-4 shows horizontal and vertical profiles from the 2D Metz filters with different values of X tested for the ^{99m}Tc and ^{18}F acquisitions.

4.2.4 Image Reconstruction

Because of the small field-of-view of this system, the conventional method of orbiting the detector about a fixed axis located near the body axis can result in truncation of the heart region, as shown in Figure 4-5A.

In order to eliminate this truncation, at each projection angle the detector is shifted tangentially to maintain the myocardium near the center of the FOV (Figure 4-5B). This angle dependent shift (effectively an angle dependent “center-of-rotation” shift) is accounted for within the reconstruction algorithm.

For each projection, the horizontal and vertical position of the detector (x , y), and the detector angle (θ) are recorded. The angle dependent shift, Δ , is computed using Equations 4-2, 4-3, 4-4, and 4-5 which is illustrated further in Figure 4-6. The MATLAB code for this algorithm can be found in Appendix B.2.

$$\Omega = \tan^{-1}\left(\frac{y}{x}\right) \quad (4-2)$$

$$\alpha = \Omega - \theta \quad (4-3)$$

$$r = \sqrt{x^2 + y^2} \quad (4-4)$$

$$\Delta = r \cdot \sin(\alpha) \quad (4-5)$$

The MLEM reconstruction algorithm (50 iterations for ^{99m}Tc and 200 iterations for ^{18}F) was used to reconstruct the images without attenuation or scatter correction applied [11]. These iteration stopping points, combined with the Metz filter, were chosen subjectively. The reconstruction times were approximately 10 seconds for the ^{99m}Tc images and 40 seconds for the ^{18}F images.

4.2.5 Effect of Angular Sampling

One of the goals of this paper was to investigate the effect of reduced angular sampling and angular range on reconstructed image quality. To test how limiting the number of projection angles affected the final reconstructed images, we reduced the number of projections reconstructed from 37 to 19 and 10 evenly spaced projection angles through 180° . The count

level was adjusted for the three cases by count thinning to simulate a constant acquisition time. To test the effect of reduced angular sampling range, the anterior 135° and 90° of projection data were extracted and reconstructed. A constant acquisition time was simulated for these tests as well.

4.2.6 Comparison with a Commercial SPECT System

To compare the performance of the mobile system to a traditional SPECT system with ^{99m}Tc , we acquired data of the dynamic cardiac phantom on a commercial SPECT system (Triad 88, Trionix Research Laboratory, Twinsburg, OH 44087). The phantom myocardium was filled with ^{99m}Tc and a 180°, 64 projection acquisition was obtained at a moderately high count level (approximately 2.15×10^5 counts within a mid-ventricular 3 mm transaxial slice resulting in an acquisition time of approximately 20 minutes). No activity was added to the phantom liver. We compared this data to a 15 minute, 37 projection acquisition with ^{99m}Tc and out-of-field activity obtained with the mobile system.

4.3 Results

4.3.1 Septal Penetration Compensation

Figures 4-7 and 4-8 show 45° projection images from the ^{99m}Tc and ^{18}F acquisitions (with out-of-field activity), respectively, with the varying degrees of filtering. Detected events outside of the myocardium are more pronounced in the ^{18}F images, as expected, due to septal penetration. The effects of increased de-convolution with filter parameter X are observed. While there is greater myocardium-to-ventricle contrast with larger X, there is also enhancement of noise. The remainder of the results focus on X=5 for ^{99m}Tc and X=50 for ^{18}F , which we found visually most pleasing.

4.3.2 Comparison with a Commercial SPECT System

Figure 4-9 shows four long and short axis slices from both the commercial system acquisition and our 37 projection acquisition with the mobile system. The figure illustrates the high degree of similarity in terms of reconstructed image quality between these two systems for imaging ^{99m}Tc with this cardiac phantom.

4.3.3 Effect of Angular Sampling

For the remainder of this chapter, the figures are labeled in terms of number of projection angles / angular coverage in degrees / total acquisition time in minutes. Figure 4-10 shows four slices in both the short and long axis planes from 15 minute acquisitions with 19 and 10 projection angles. This figure demonstrates that reducing the number of projection angles to 19 does not appreciably affect the image quality when using ^{99m}Tc . Figure 4-10 also shows that reducing the sampling in an extreme case to 10 projections degrades the images both with streaking artifacts outside the myocardium and dark streaks in the myocardium.

We also wanted to test the effect of reducing the angular coverage from 180° . We observed that reducing the angular coverage to 135° did not severely degrade reconstructed image quality. Figure 4-11 also showed that severely limited angular coverage (90°) introduced substantial streak artifacts. In a clinical situation, reducing the angular coverage would only be recommended if the bedside environment prevented full 180° angular coverage.

Figure 4-12 shows the reconstructed image slices from the ^{18}F data without out-of-field activity in the liver. Compared with the ^{99m}Tc images with similar angular sampling, the ^{18}F images exhibit somewhat degraded spatial resolution of the myocardium walls and a reduced ventricle-to-myocardium contrast. These effects become more pronounced in the 19 angle images. In spite of this, the overall shape of the myocardium is accurately depicted.

Figure 4-13 shows the ^{18}F results with liver activity present. Also included in the figure are projection images with and without background activity. These images begin to show a distortion of the shape of the myocardium and a small level of intensity artifacts (hot and cold spots) that are not observed in the images without liver activity. As with the $^{99\text{m}}\text{Tc}$ acquisitions we reconstructed images with reduced angular coverage, but reducing the angular coverage to less than 180° resulted in severe streaking artifacts.

4.4 Summary and Discussion

This chapter presented the SPECT performance evaluation of a mobile gamma imager for cardiac applications using $^{99\text{m}}\text{Tc}$ and ^{18}F . The system employed angle-dependent projection shifting to reduce truncation effects and de-convolution filtering to control septal penetration effects with ^{18}F .

The results using a dynamic cardiac phantom showed that with $^{99\text{m}}\text{Tc}$, the mobile system was capable of producing reconstructed image quality comparable to a commercial SPECT system. The reconstructed image quality did not substantially degrade when the angular sampling was reduced to 19 angles over 180° or to 28 angles over 135° . This angular sampling is less than what is typically required of larger FOV, conventional SPECT systems.

The results with the ^{18}F images showed a moderate degree of spatial resolution loss compared with the $^{99\text{m}}\text{Tc}$ images. With liver activity present, a distortion of the myocardial shape was observed, which we attribute to increased detection of septal penetration photons. This distortion from septal penetration photons, even after filtering, is the motivation to design a high energy pinhole collimator.



Figure 4-1. The dynamic cardiac phantom and the bedside imaging system with the detector head in a left oblique position (45 degrees).

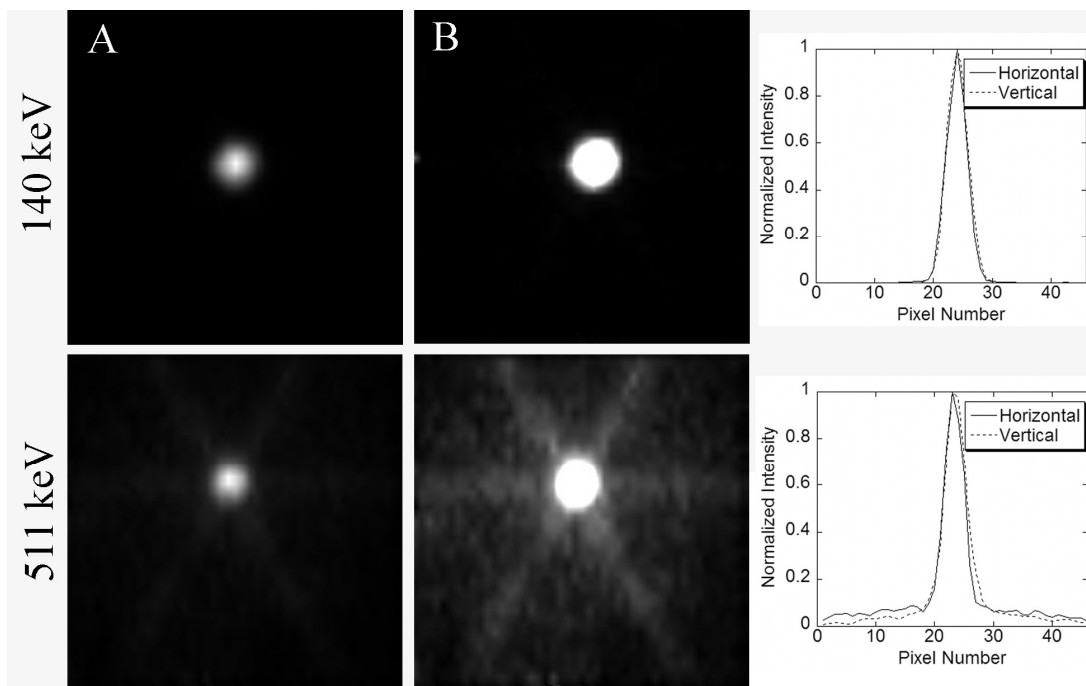


Figure 4-2. A) Point source images for 140 keV and 511 keV sources without windowing. B) Images windowed to 33% of the maximum pixel intensity. Images shown with the corresponding horizontal and vertical profiles. The FOV in both images is $25 \times 25 \text{ cm}^2$.

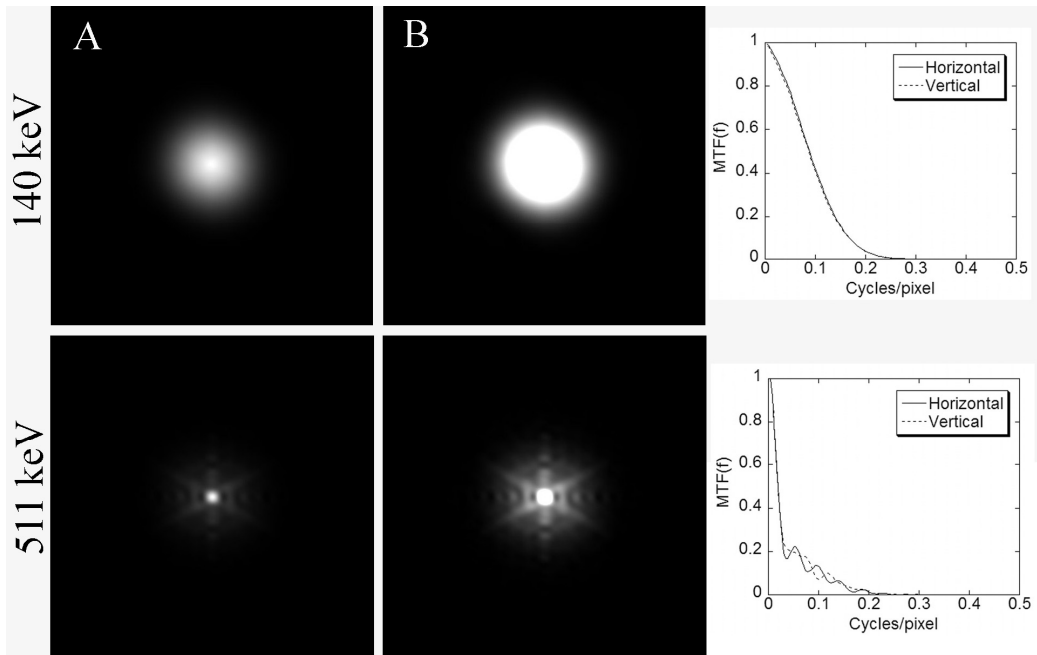


Figure 4-3. A) MTF. B) MTF windowed to 33% of the maximum pixel intensity. Images shown along with the corresponding horizontal and vertical profiles for both 140 and 511 keV point sources used in calculating the Metz filter.

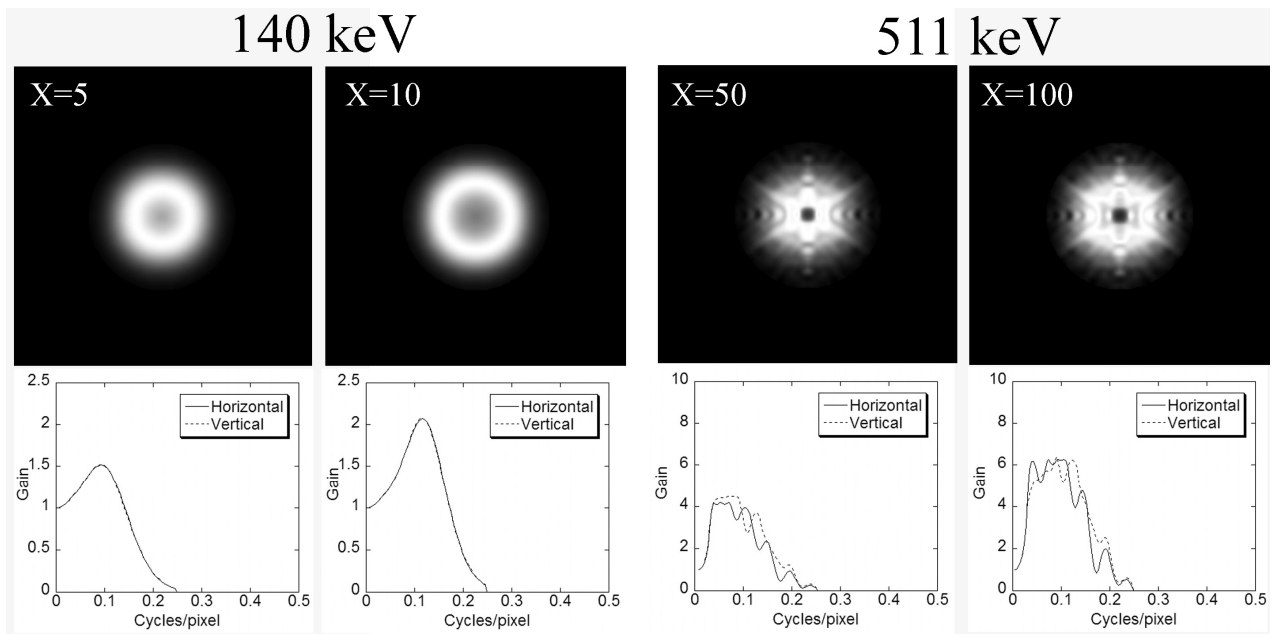


Figure 4-4. Metz filters and the associated horizontal and vertical profiles from for both 140 keV and 511 keV with different values for X.

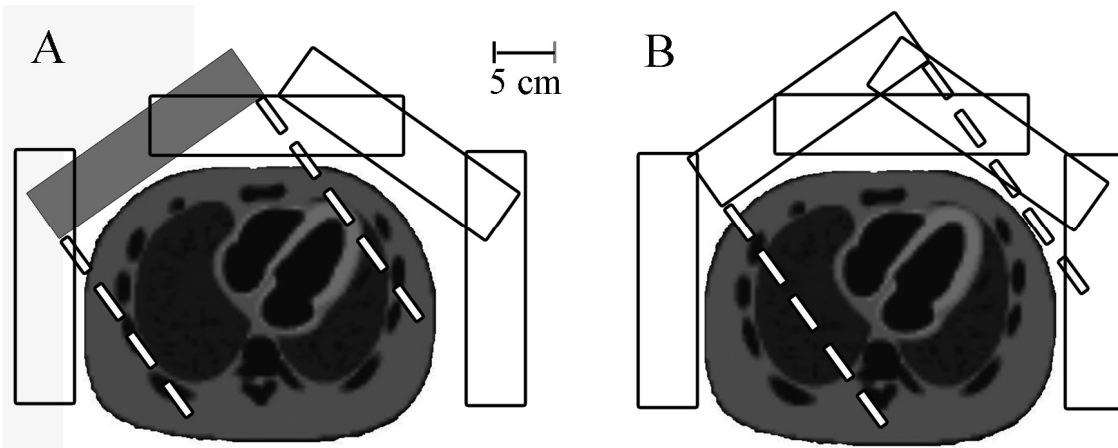


Figure 4-5. Five projection angles demonstrating how different acquisition protocols can result in myocardial truncation. A) Fixed axis acquisition protocol resulting in truncation. B) New protocol which does not truncate the myocardium. The shaded detector is an example of a position causing myocardial truncation as shown by the dashed lines indicating the edges of the FOV.

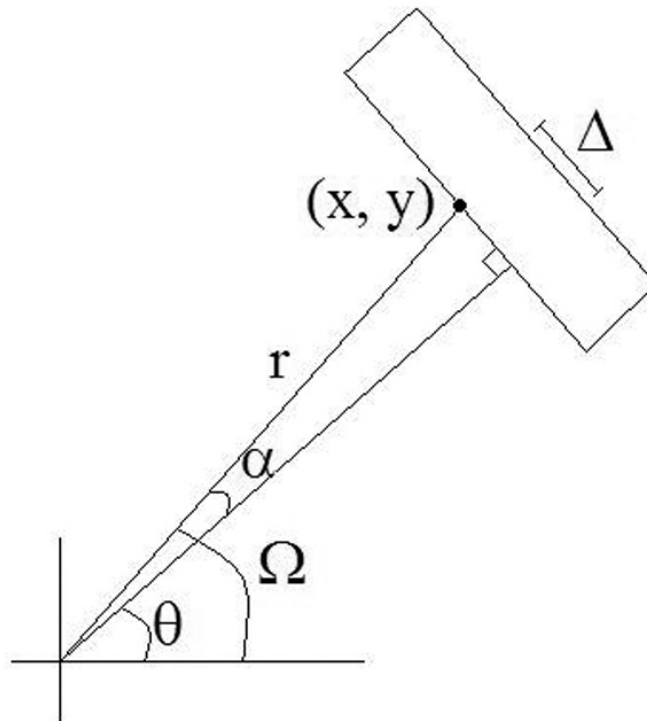


Figure 4-6. Parameters used in the center-of-rotation correction algorithm to allow for shifted detector positioning which eliminated myocardial truncation.

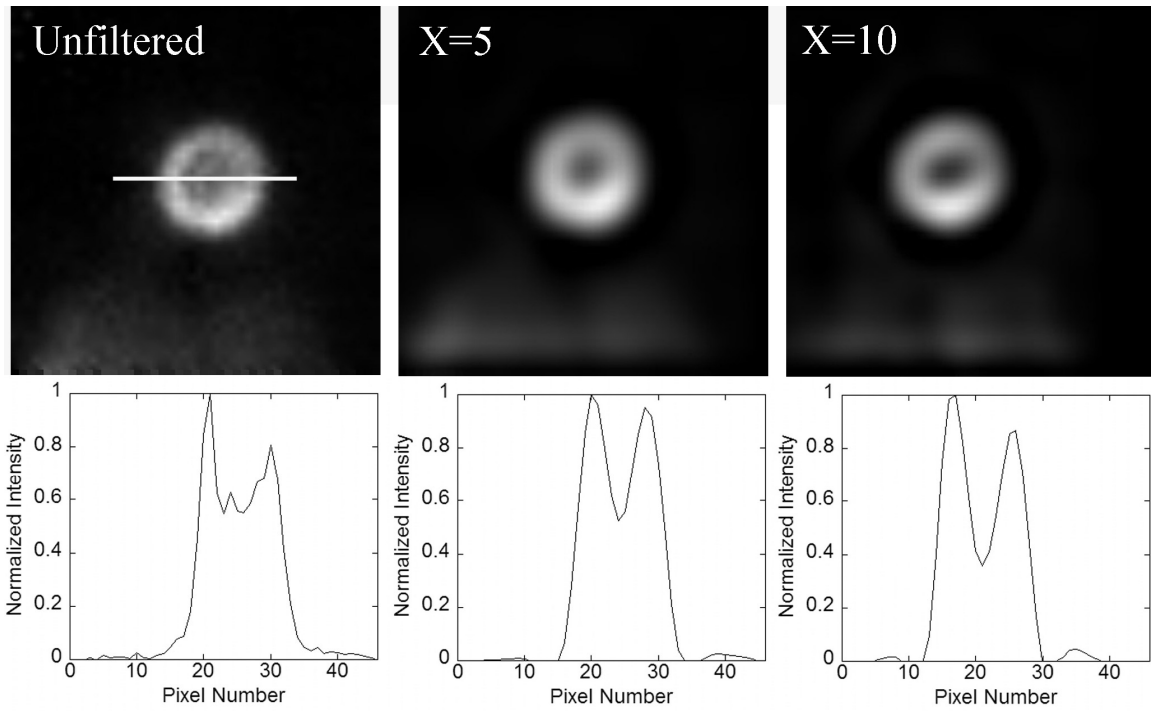


Figure 4-7. Projection images obtained at 45 degrees using ^{99m}Tc and out-of-field activity with varying degrees of filtering.

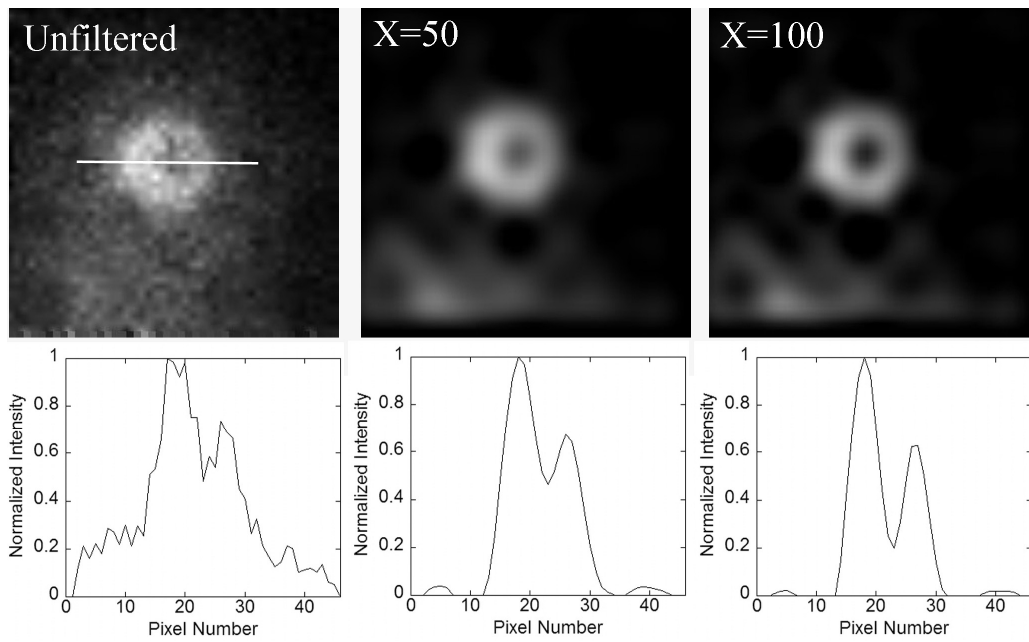


Figure 4-8. Projection images obtained at 45 degrees using ^{18}F and out-of-field activity with varying degrees of filtering.

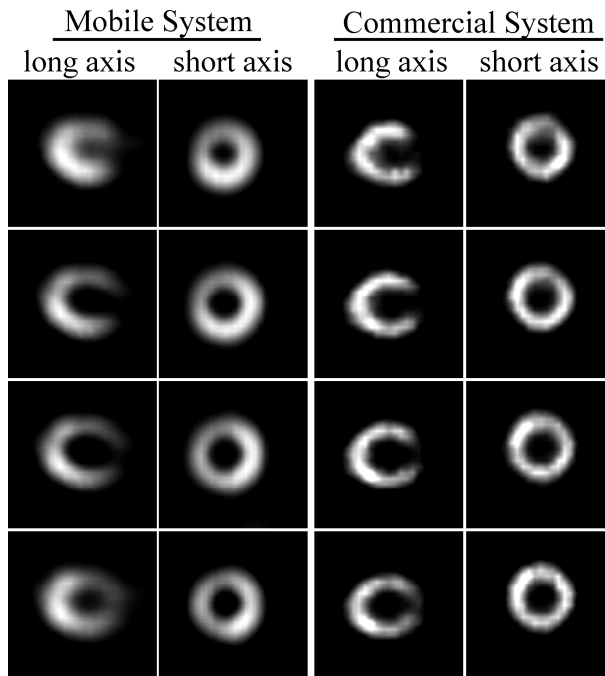


Figure 4-9. Comparison of the mobile system's performance to a commercial system using the dynamic cardiac phantom and ^{99m}Tc . The mobile system used 37 angles over 180 degrees and the commercial system used 64 angles over 180 degrees.

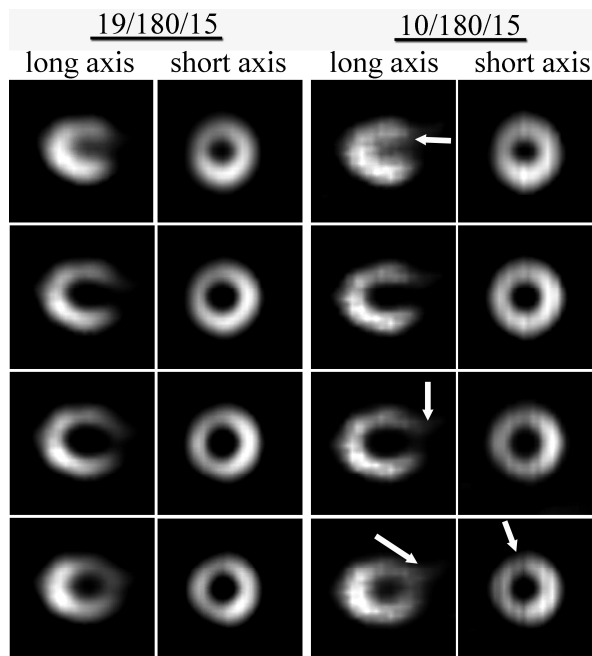


Figure 4-10. Four long axis and four short axis slices from the 15 minute ^{99m}Tc acquisitions with 19 and 10 projection angles. Artifacts in the images are indicated by the white arrows.

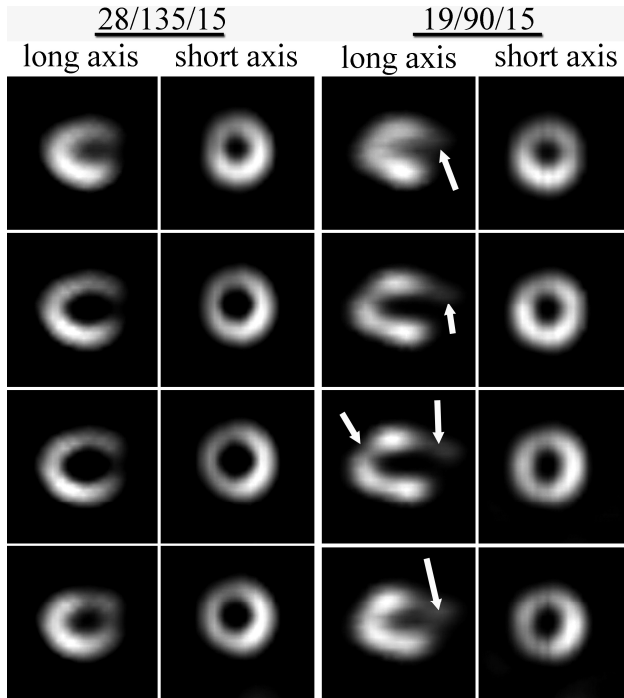


Figure 4-11. Four long axis and four short axis slices from the ^{99m}Tc 135 degree angular coverage acquisition and the 90 degree angular coverage acquisition. Artifacts are indicated by the white arrows.

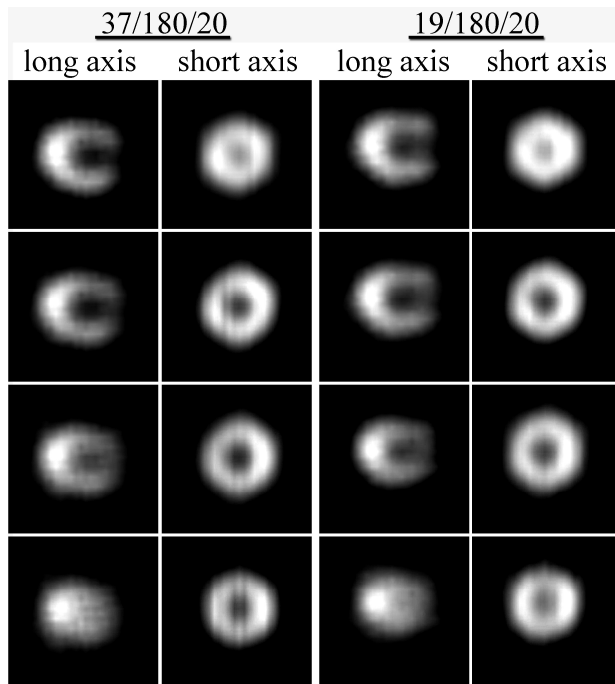


Figure 4-12. Four long axis and four short axis slices from the ^{18}F acquisitions without activity in the liver and 37 and 19 projection angles.

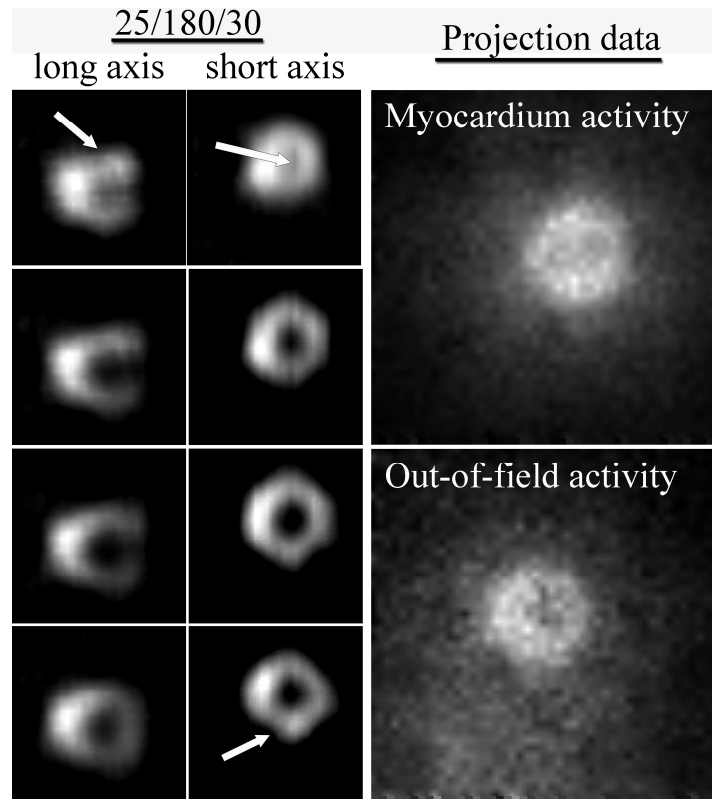


Figure 4-13. Four long axis and four short axis slices from the 30 minute ^{18}F acquisition (including out-of-field activity). Artifacts are indicated by the white arrows. The projection data to the right shows the effect of penetration photons from the out-of-field activity.

CHAPTER 5 DESIGN AND SIMULATION OF A HIGH ENERGY PINHOLE COLLIMATOR

5.1 Introduction

Previous chapters showed that ^{18}F imaging without a prohibitively heavy parallel hole collimator resulted in artifacts in the final reconstructed image from septal penetration patterns in the projection data. Chapter 4 showed that filtering the projection data with a Metz filter before reconstruction slightly alleviated this effect but did not completely correct for it. In this chapter, we take another approach to reduce these degrading penetration patterns by designing a high energy pinhole collimator.

Pinhole collimation is one of the simplest and oldest means of gamma ray imaging [21]-[23]. More recently, pinhole collimation has become popular for small animal imaging due to the extremely high spatial resolution that can be achieved [24], [25]. Pinhole collimation is also used for small organ imaging such as the thyroid, brain, and breast [26]-[29].

Several studies using high energy gamma emitters such as ^{131}I with pinhole collimators have been performed [29]-[32]. These studies show that although the pinhole collimator is not affected by septal penetration star patterns like a parallel hole collimator, high energy photons do penetrate through the edge of the pinhole or can scatter in the pinhole which reduces the spatial resolution of the system.

Our high energy pinhole collimator design will be based on theoretical equations defining collimator spatial resolution and sensitivity. We will then compare these theoretical results to Monte Carlo simulations using GATE (Geant4 Application for Tomographic Emission) [33], [34]. Finally, we will compare the final pinhole design to our current parallel hole collimator in simulated tomographic acquisitions.

Another aspect of pinhole collimation we must consider is the axial blurring that results in a tomographic acquisition from inadequate sampling at the edges of the field-of-view. We will study the magnitude of this effect for cardiac imaging with our mobile system.

5.2 Methods

5.2.1 Theoretical Collimator Resolution and Sensitivity

The design goal of this pinhole collimator is to match the performance of our parallel hole collimator in terms of spatial resolution and sensitivity. In parallel hole collimation, the resolution and sensitivity are determined by the hole shape, hole length (l), hole diameter (d), source-to-collimator distance (b), and septa thickness (t) (Figure 5-1). The spatial resolution (R_{coll}) and sensitivity (g) are defined by Cherry, *et al.* using Equations 5-1, 5-2, and 5-3 where l_{eff} is the effective collimator length taking into account penetration through the septa [10].

$$R_{\text{coll}} = \frac{d(l_{\text{eff}} + b)}{l_{\text{eff}}} \quad (5-1)$$

$$g = K^2 \left(\frac{d}{l_{\text{eff}}} \right)^2 \left[\frac{d^2}{(d+t)^2} \right] \quad (5-2)$$

$$l_{\text{eff}} = l - \frac{2}{\mu} \quad (5-3)$$

In Equation 5-2, K is a constant that is dependant on hole shape (~ 0.26 for hexagonal) and in Equation 5-3, μ is the attenuation coefficient of the collimator material at the imaging energy. Our high energy parallel hole collimator has hexagonal holes, $l = 4.9$ cm, $d = 2.3$ mm, and $t = 2.02$ mm.

Pinhole collimator spatial resolution and sensitivity are defined by the pinhole diameter (d), the collimator length (l), source-to-collimator distance (b), pinhole acceptance angle (α), and the angle between the photon path through the pinhole and the detector surface (θ) (Figure 5-1).

A simple method of analytically calculating pinhole collimator resolution (Equation 5-4) and sensitivity (Equation 5-5) was derived by Anger [35]. These equations tend to be inaccurate because the penetrative component does not take into account the angular dependence of the photon's path through the pinhole. Anger assumes an effective diameter, d_{eff} , of the pinhole that is larger than the actual pinhole diameter through which photons pass without any attenuation. With this method, the spatial resolution and sensitivity are calculated with a geometric component, only. The effective diameter is calculated using Equation 5-6.

$$R_{\text{coll}} = \frac{d_{\text{eff}}(1 + b)}{1} \quad (5-4)$$

$$g = \frac{d_{\text{eff}}^2 \sin^3(\theta)}{16b^2} \quad (5-5)$$

$$d_{\text{eff}} = \sqrt{d \left[d + 2\mu^{-1} \tan\left(\frac{\alpha}{2}\right) \right]} \quad (5-6)$$

More recently, theoretical equations accounting for the angular dependence of photon penetration have been derived by Metzler, *et al.* [36], [37]. Instead of simply calculating a geometric component with an effective diameter, they derived equations that account for the different photon pathlengths through the pinhole edges based on the photon approach angle. With this method, they combine both a geometric and penetrative component to calculate the spatial resolution and sensitivity of the pinhole collimator.

In [36], Metzler, *et al.* calculate collimator spatial resolution in terms of the root mean square (RMS) resolution instead of a FWHM as in Anger and Cherry, *et al.* To be able to have a meaningful comparison of the spatial resolution, we will use their method of generating a pinhole response function (PRF) to calculate a FWHM from a profile across this response function and scale this profile to account for pinhole magnification. This will provide a profile

on the object plane for a direct comparison with Anger's and Cherry, *et al.*'s predictions. The PRF is calculated using Equation 5-7 where ΔL is the photon pathlength through the pinhole edge and is defined in detail in [36].

$$\text{PRF}(r) = \begin{cases} \frac{\sin^3 \theta}{4\pi(b+l)^2} & r \leq \frac{d(b+l)}{2b} \\ \frac{\sin^3 \theta}{4\pi(b+l)^2} e^{-\mu\Delta L} & r > \frac{d(b+l)}{2b} \end{cases} \quad (5-7)$$

As with the spatial resolution, the theoretical sensitivity accounting for both geometric and penetrative components can be derived. We will calculate this using an analytical formulation derived by Metzler, *et al.* [37].

5.2.2 Pinhole Collimator Design

5.2.2.1 Field-of-view and pinhole acceptance angle

To meet our pinhole collimator design goal, we must determine the field-of-view (FOV) size required for imaging the myocardium. The myocardium has a length of up to 14 cm along the long axis [38], and we want to ensure that the myocardium is not truncated during an acquisition. Although we want to ensure complete coverage of the myocardium, we do not want an excessively large acceptance angle because we want to reduce the depth-of-interaction effect that occurs with photons obliquely entering the crystal and we want to reduce the out-of-field activity in the FOV. Figure 5-2 shows the anatomy covered by two acceptance angles (α) considered for this design, 70° and 90° , for three projection angles along with the location of the scintillation crystal. We did not consider smaller acceptance angles because these begin to truncate anatomy at the projection angles where the collimator is close to the myocardium.

5.2.2.2 Collimator focal length

Because of the small FOV ($25 \times 25 \text{ cm}^2$) of the detector, we must fix the collimator focal length to prevent anatomy from being projected off the edge of the crystal. Using Equation 5-8,

the length of the collimator is calculated taking into account the magnification of the FOV on the image plane. In Equation 5-8, D_{det} is the diameter of the detector which for our system is 25 cm. FOV(b) is the diameter of the FOV at any source-to-collimator distance, b, calculated using Equation 5-9. Equations 5-8 and 5-9 show that if we know the acceptance angle, we can calculate the collimator length.

$$l = \frac{b \cdot D_{\text{det}}}{\text{FOV}(b)} \quad (5-8)$$

$$\text{FOV}(b) = 2b \cdot \left(\tan \frac{\alpha}{2}\right) \quad (5-9)$$

5.2.2.3 Pinhole material

To reduce the amount of penetration photons, we considered using a pinhole material with a higher attenuation coefficient than lead [32], [39], [40]. For this design we only focused on tungsten because of the cost of other high Z materials such as gold, platinum, or uranium. The main collimator body is still made out of lead but an insert containing the pinhole will be made of tungsten.

5.2.3 Axial Blurring With Pinhole Collimators

In a tomographic acquisition with a pinhole collimator, the reconstructed image suffers from axial blurring due to incomplete sampling at the edges of the FOV [41]. This effect is reduced as the radius-of-rotation is increased. The problem is that as the radius-of-rotation is increased, the sensitivity and spatial resolution of the collimator decrease. A solution to this problem is to acquire in a helical orbit rather than a circular orbit. This reduces the effect of axial blurring and allows for a decreased ROR but because our system requires manual detector positioning at each projection angle, acquiring in a helical orbit would be extremely difficult.

During an acquisition, we want to orbit the detector as close to the patient as possible to increase the spatial resolution and sensitivity in the image. Since this will increase the amount of axial blurring at the edges of the FOV, we need to determine how much blurring will occur in a cardiac acquisition with our system. Since humans are not round, the acquisition protocol requires a changing radius-of-rotation depending on the projection angle. To obtain a realistic set radius-of-rotations, we performed a 25 projection acquisition on a dynamic cardiac phantom with a realistic torso and recorded the distance from the center of the myocardium to the collimator at each projection angle. This distance varied from 7 cm at the left anterior oblique angles up to 25 cm at the right lateral projection angle. All of the distances can be seen in Table 5-1.

We first wanted to study how the radius-of-rotation affected the amount of axial blurring in the final reconstructed image. Due to long run times with Monte Carlo simulations, we used a forward projection algorithm to simulate an acquisition with a Defrise phantom, similar to the method in [41]. The Defrise phantom is a series of seven 2.5 cm thick cylinders with 5 cm radii aligned on the axis-of-rotation. These cylinders are spaced 2.5 cm apart. We simulated 25 projections with RORs of 10 cm, 20 cm, and 30 cm to cover all the distances in a cardiac acquisition. To study the effect of different acceptance angles, we simulated collimators with 70 and 90 degree acceptance angles. Figure 5-3 shows the geometry in these simulations. The projection data were reconstructed using 50 iterations of a maximum likelihood expectation maximization algorithm (MLEM) into a $256 \times 256 \times 150$ matrix of 0.25 cm^3 voxels [11]. From the reconstructed images, we were able to quantify the effects of axial blurring.

We also used the forward projection algorithm to model a realistic activity distribution using the NCAT phantom [42]. We simulated 25 projection angles with the source-to-collimator

distances found in Table 5-1. We could only use this data to study the effect of axial blurring because sensitivity and spatial resolution effects were not simulated in the forward projector. We tested two different pinhole acceptance angles, 70° and 90° , to determine which provided a better image of the myocardium (Figure 5-2). Again, the projection data were reconstructed using 50 iterations of a MLEM algorithm.

5.2.4 Determination of Pinhole Parameters

After we analyzed the reconstructed NCAT phantom images, we were able to choose which acceptance angle we wanted and calculate the collimator focal length. Next we needed to determine a pinhole diameter that would match both the spatial resolution and sensitivity of our parallel hole collimator. We considered diameters ranging from 1 mm up to 4 mm knowing from theoretical equations that the 1 mm diameter would improve spatial resolution and reduce sensitivity and the 4 mm diameter would have the opposite effect. For the spatial resolution comparison, we compared source-to-collimator distances of 5 cm to 25 cm and photon entry angles of 90° (on collimator axis) and 70° (off axis) to cover different locations in the FOV. FWHMs were calculated at the object plane to accurately compare spatial resolution in both collimators by eliminating the effect of magnification from the pinhole collimator.

The theoretical sensitivity of the pinhole collimator was calculated relative to that of our high energy parallel hole collimator. As with the spatial resolution comparison, we compared source-to-collimator distances of 5 cm to 25 cm, on axis and off axis. With the theoretical comparisons of spatial resolution and sensitivity, we chose our pinhole collimator design parameters to most closely match our parallel hole collimator.

5.2.5 GATE Simulations

Simulations were run in GATE to test its accuracy against theoretical predictions. Once validated, we could simulate tomographic acquisitions and a keel edge collimator. Because of

long run times in GATE, planar simulations were done with a 100 μCi , 511 keV point source, and a 30 s acquisition time in air. To simplify the geometry, the simulated collimator was a 2.5 cm thick lead sheet ($25 \times 25 \text{ cm}^2$) with a tungsten insert containing the pinhole. This collimator was located at a distance from the crystal equal to the focal length. The crystal was simulated to be the same as in our mobile system (45×45 pixels, 1.25 cm thick NaI).

To test the accuracy of GATE, the point source was simulated in air at four different points, on axis and off axis at 10 cm and 30 cm from the collimator, to cover different areas in the FOV. The theoretical profiles were calculated on the image plane so Anger's prediction was scaled to account for magnification. The theoretical profiles were also convolved with the intrinsic resolution of the simulated crystal for the comparison with the simulated image.

The sensitivity was also calculated in the planar GATE images and compared with theoretical values over distances of 5 cm to 30 cm and off axis positions of 90° to 60° . All of the theoretical values were scaled by the capture probability of the 1.25 cm NaI crystal to account for detector efficiency ($\mu = 0.349 \text{ cm}^{-1}$ at 511 keV [43]).

5.2.6 Keel Edge vs. Knife Edge Pinhole Collimator

In addition to changing the pinhole material to reduce penetration, the collimator can be designed with a keel (or channeled) edge rather than a knife edge, as seen in Figure 5-4 [32]. Since there are no theoretical equations defining a keel edge pinhole, the results must be obtained from simulations using GATE.

The benefit of the keel edge is that the reduction in penetration photons through the edge of the pinhole provides better spatial resolution although this increase in resolution comes at a loss of sensitivity. Using the same pinhole collimator parameters from the chosen design, a simulation was run in GATE with a keel thickness of 2.5 mm ($\sim 50\%$ attenuation at 511 keV with tungsten [43]) to determine if a keel edge would be a better design than the knife edge.

5.2.7 Tomographic Comparison of Pinhole and Parallel Hole Collimators

The main reason behind designing a pinhole collimator was to eliminate the star pattern that results in high energy parallel hole collimator imaging. This pattern propagates through the reconstruction and degrades the final reconstructed image. As an initial comparison, we used theoretical equations to compare the spatial resolution and sensitivity of both collimators in air assuming that in a tomographic acquisition, an average source-to-collimator distance is 13 cm (Table 5-1). The spatial resolution was calculated on the object plane and the sensitivity was calculated in terms of counts/ $\mu\text{Ci/s}$.

Since the theoretical equations do not account for septal penetration, to determine the extent of the degradation in the reconstructed image, we needed to simulate projection data in GATE. To shorten the run times, we assumed that the activity distributed in the myocardium was condensed to a point source of 100 μCi . This point source was simulated in a 10 cm radius sphere of water and each projection was 30 s long. We did not simulate a complete tomographic acquisition because of simulation time. Instead, we simulated the point source at distances of 10 cm, 15 cm, 20 cm, and 25 cm from the collimator in the water sphere. We then created projection sets for a fixed ROR acquisition protocol using the single projection image and repeating it 25 times and to simulate a varying ROR protocol, we rounded the distances in Table 5-1 to the closest multiple of five and used our single projection images to generate a complete projection set. We reconstructed the projection data using 50 iterations of a MLEM algorithm. As before, we calculated the sensitivity in terms of counts/ $\mu\text{Ci/s}$ and for the spatial resolution, we calculated the reconstructed FWHM in the coronal and transaxial planes. The results for the pinhole collimator were then compared to the parallel hole collimator results.

Since spatial resolution and sensitivity decrease as source-to-collimator distance increases, we wanted to test acquisition protocols where we would eliminate the projections with a long

source-to-collimator distance (right anterior oblique and right lateral projections). To do this, we calculated the average sensitivity over a tomographic acquisition assuming we eliminated the last few projection angles. We took the sensitivity calculated from the GATE projection data with the point source in water and averaged over all projection angles for both the parallel hole and pinhole collimator. We realize that not acquiring over 180° will degrade the quality of the reconstructed image, but we showed in chapter 4 that with the small FOV of the detector, acquiring over 135° still provided a viable image of the myocardium.

5.3 Results

5.3.1 Acceptance Angle and Collimator Focal Length

Before we determined any of the pinhole collimator design parameters, we analyzed the effect of radius-of-rotation on axial blurring in a tomographic acquisition. Figure 5-5 shows coronal slices and a profile along the axis-of-rotation for the Defrise phantom simulations with both the 70 and 90 degree acceptance angles and varying radius-of-rotations (10 cm, 20 cm, and 30 cm). For both acceptance angles, as the ROR decreased, the axial blurring at the edges of the FOV increased. Also, as the ROR decreased, the FOV becomes smaller, truncating the outer slices. The 90° acceptance angle has a wider FOV so less slices of the phantom are truncated as the ROR is decreased. In a clinical acquisition, we want the collimator as close as possible to the patient, approximately 10 cm to 25 cm depending on the projection angle. Figure 5-5 shows that axial blurring could affect the images of the myocardium at these short RORs.

We want collimator design parameters that minimize axial blurring while maximizing spatial resolution and sensitivity in a cardiac acquisition. To determine the acceptance angle and the collimator length, we needed a realistic source distribution to study the effects of axial blurring, first. Using the reconstructed data from the NCAT phantom simulations with realistic radius-of-rotations and two different acceptance angles, we were able to choose the acceptance

angle to minimize axial blurring. Figure 5-6 shows coronal and transaxial slices from the reconstructions with acceptance angles of 70 and 90 degrees along with the NCAT phantom used. Looking at the coronal slices where the axial blurring will have the greatest effect, both collimators showed minimal blurring at the edges of the FOV. The 70° did show slight streaking artifacts at left edge of the myocardium but this was due to anatomy truncation at short RORs from the smaller FOV. An advantage with the 70° acceptance angle is increased magnification and spatial resolution due to the longer focal length of the collimator but the decrease in FOV size is an issue especially in a clinical acquisition. In this simulation, the exact location of the heart is known so the myocardium was located completely in the FOV, but in a clinical situation where positioning the collimator perfectly is not easy, the small FOV with the 70° acceptance angle collimator could truncate anatomy.

With the 90° acceptance angle, the FOV is larger than with the 70° acceptance angle. Therefore, in a clinical acquisition, we will not have to be as concerned about anatomy truncation from detector positioning. This will make the overall acquisition easier and quicker. For this reason, we decided on the 90° acceptance angle even though there is increased out-of-field activity and the obliquity effect is increased. Another reason for choosing this larger acceptance angle was that the collimator focal length was shortened. This reduces magnification and the spatial resolution slightly, but more importantly it will reduce the overall weight of the collimator (see chapter 5.4). This 90° acceptance angle fixed the collimator length at 12.5 cm using Equations 5-8 and 5-9.

5.3.2 Pinhole Collimator Design Parameters

With the acceptance angle and focal length set, we needed to determine the pinhole diameter to meet our design goal of matching the spatial resolution and sensitivity of our parallel hole collimator. To obtain a meaningful comparison of spatial resolutions, profiles on the object

plane were generated and the FWHMs were obtained. Figure 5-7 shows profiles generated at four different locations in the FOV for two different pinhole diameters. Although Metzler, *et al.*'s profile has a flat top and is different from the Gaussian profiles generated for Anger's and Cherry, *et al.*'s predictions, there is good agreement in the FWHMs of the profiles. We will use these FWHM values to compare the spatial resolution with different pinhole diameters and source-to-collimator distances.

5.3.2.1 Spatial resolution

Figure 5-8 shows the parallel hole collimator resolution and the pinhole resolution predicted by Metzler, *et al* for different pinhole diameters. The spatial resolution was calculated on the object plane to eliminate the effect of magnification with the pinhole collimator. We did not include Anger's prediction in the figure because it agreed well with the prediction by Metzler, *et al.*

We needed to verify simulations from GATE with simple planar simulations in air to be able to simulate a keel edge collimator and tomographic acquisitions. Initial planar simulations in GATE with 511 keV point sources in air at $b = 10$ cm can be seen in Figure 5-9. The septal penetration patterns in the projection data that propagate through the reconstruction with the parallel hole collimator are clearly seen. To compare with the GATE projection images, the theoretical profiles were convolved with the intrinsic resolution of the simulated crystal in GATE. The intrinsic resolution was calculated to be 0.60 cm FWHM from a simulation with a 1 mm slit.

Figure 5-10 shows the profiles of the GATE and theoretical parallel hole collimator with two different source-to-collimator distances. The profiles simulated in GATE agree well with the predictions for the parallel hole collimators over different source-to-collimator distances. One difference in the GATE profile is the high energy penetration tails. The theoretical profile

goes to zero outside the peak because penetration patterns are not accounted for. Also, the GATE profiles show increased noise from fewer photons reaching the detector at long source-to-collimator distances.

Figure 5-11 compares the profiles in air for the GATE pinhole collimator with both theoretical profiles predicted by Anger and Metzler, *et al.* Again, the GATE profile agrees with both theoretical predictions. The tails seen outside of the peak can be ignored as they do not play a role in the final collimator. These noisy tails could be eliminated by thickening the lead in the simulated collimator but this would increase the simulation time. We are only concerned with the FWHMs of the GATE and theoretical profiles.

5.3.2.2 Sensitivity

Figure 5-12 shows Metzler, *et al.*'s prediction of pinhole collimator sensitivity relative to our parallel hole collimator with varying pinhole diameters and source-to-collimator distances. We did not include the prediction by Anger in the figure but his prediction was much higher than Metzler, *et al.*'s prediction, the same result as in [37]. The reason for the difference is the calculation of the penetrative component of the sensitivity. Since Anger only considers a geometric component with an effective diameter that is larger than the actual diameter, more photons enter the pinhole without any attenuation. Metzler, *et al.*'s prediction accounts for attenuation based on the photon pathlength through the pinhole edge and results in a more accurate calculation of sensitivity.

Remember from chapter 3 that the sensitivity is affected by the septal penetration photons because uncollimated counts contribute to the sensitivity measurement. To obtain a measurement that minimizes the effect of uncollimated counts on the sensitivity, we calculated a level of thresholding based on the maximum pixel intensity that would reduce the number of uncollimated photons counted. This was done by segmenting the image and only summing

pixels with counts higher than the threshold value. The threshold results from images obtained in GATE are seen in Figure 5-13. By increasing the threshold, more septal penetration counts are eliminated from the sensitivity measurement. We want a threshold level that eliminates septal penetration counts to provide a sensitivity close to that of the theoretical predictions scaled to account for the capture probability in the crystal.

As with the spatial resolution, we wanted to verify that the sensitivity in GATE was similar to theoretical predictions. Figure 5-14 shows the effect on sensitivity as the source-to-collimator distance is increased. It is not shown in the figure, but the GATE parallel hole results agreed well with the theoretical predictions as they did with spatial resolution. The GATE pinhole results agree well with predictions by Metzler, *et al.* but Anger's prediction is higher, as discussed earlier.

Except for Anger's sensitivity prediction, GATE simulations agreed well with the theoretical predictions and should provide accurate results for both the keel edge collimator simulation and the tomographic acquisition simulations.

5.3.2.3 Pinhole diameter

Our goal was to match the spatial resolution and sensitivity of the parallel hole collimator. Figure 5-8 shows that the spatial resolution with a 2 mm diameter pinhole was improved over the parallel hole collimator at relevant source-to-collimator distances and photon entry angles. When the diameter was increased to 3 mm, on axis, the resolution was slightly lower at short distances but improved as the distance was increased. It matched well for the off axis point. Based on spatial resolution, the 2 mm diameter would be a better choice but Figure 5-12 shows that the sensitivity for this diameter is lower than the parallel hole collimator. Because of this, we decided to use a 3 mm diameter to maximize the sensitivity of the pinhole collimator. We

chose the final design parameters to be a 3 mm diameter tungsten pinhole, with $l = 12.5$ cm, and $\alpha = 90^\circ$.

5.3.3 Keel Edge Collimator

Simulations in GATE with a pinhole collimator modified with a 2.5 mm keel showed an improvement in spatial resolution of about 1 mm with a decrease in sensitivity of 50% at distances of 10 cm and 25 cm on and off axis. The sensitivity was calculated using the 8% threshold. These simulations show that it is not beneficial to design this high energy collimator with a keel edge. In our opinion, the loss in sensitivity is not compensated by a significant increase in spatial resolution especially with longer radius-of-rotations. The keel edge design is more effective for lower energy photons around 300 keV since 511 keV photons require thicker keel resulting in a greater reduction in sensitivity.

5.3.4 Tomographic Comparison

For the initial collimator comparison, we calculated the theoretical spatial resolution and sensitivity of our parallel hole and pinhole collimator assuming an average ROR of 13 cm. The theoretical equations predicted that the parallel hole collimator had superior spatial resolution (1.10 cm FWHM vs. 1.22 cm FWHM) and superior sensitivity (0.92 cts/ μ Ci/s vs. 0.33 cts/ μ Ci/s).

Although the parallel hole collimator was theoretically superior to the pinhole collimator, septal penetration is not accounted for. Using GATE, we simulated a point source in a 10 cm radius sphere of water to compare the reconstructed spatial resolution and sensitivity accounting for septal penetration patterns. The sensitivity was calculated using the 8% threshold. Table 5-2 contains the results from the reconstructed images with fixed radius-of-rotations and also a varying radius-of-rotation acquisition.

As expected, the sensitivity of the parallel hole collimator was constant over all ranges of source-to-collimator distances and was higher than the sensitivity of the pinhole collimator,

especially at longer distances. For the spatial resolution, the reconstructed spatial resolution was better for the pinhole collimator over all distances. This proved that the penetration patterns propagate through the reconstruction and degrade the final reconstructed resolution of the parallel hole collimator.

When comparing the realistic, varying ROR acquisition, the parallel hole collimator had better sensitivity in both the simulations and theoretical predictions. In terms of spatial resolution, the theoretical prediction was that the parallel hole collimator should have improved resolution but because of spetal penetration patterns, the spatial resolution of the pinhole collimator was improved over the parallel hole collimator in the simulated data.

In a clinical environment, we suspect that the decreased sensitivity of the pinhole collimator can be partially compensated by extending the acquisition time. Also, we want to study the effect of eliminating the projection angles with long source-to-collimator distances that have a reduced sensitivity. Table 5-3 shows the sensitivity calculated after eliminating the long source-to-collimator distance projections. As expected, the sensitivity of the parallel hole collimator is constant over all source-to-collimator distances and therefore does not change if projections are eliminated. The pinhole sensitivity increases slightly as the projections with long source-to-collimator distances are eliminated although the gain in sensitivity is not great. Further study would have to be done using an acquisition protocol that not only eliminates the long distance projections but increases the scan time on the short source-to-collimator distance projection angles. Also, the effect on spatial resolution in the reconstructed image must be studied since removing projections reduces the angular coverage in the acquisition.

Overall, the simulations demonstrate a gain in spatial resolution with the pinhole collimator that supports our initial belief that designing a high energy pinhole collimator would improve image quality over high energy parallel hole collimator imaging.

5.4 Conclusions

We have considered the possibility of using a pinhole collimator with our mobile system for high energy cardiac imaging. We found that using a realistic acquisition protocol, the spatial resolution is better for the pinhole collimator but the sensitivity is better with the parallel hole collimator. With our mobile system, we believe that the low sensitivity for can be compensated for in a clinical environment by extending the acquisition time and using an acquisition protocol that lengthens the projections with short source-to-collimator distances. The greatest advantage of the pinhole collimator is the elimination of septal penetration photons seen with the parallel hole collimator which require a high degree of filtering to alleviate. This is the motivation to manufacture the pinhole collimator and continue with this investigation.

We have also demonstrated that the theoretical equations derived by Metzler, *et al.* and Anger agree well with simulations in GATE. Metzler, *et al.*'s prediction showed slightly better agreement with simulated data than did the equations derived by Anger for sensitivity. Accounting for the angular component of photon penetration resulted in increased accuracy.

Weight is a concern with this design because all detector positioning must be done manually. To achieve 99% attenuation with lead at 511 keV, a thickness of at least 2.5 cm required [43]. By reducing the thickness to 1.6 cm, the attenuation only drops to 95%. The simplest design would be to have an aluminum box and cover the top with lead around the pinhole. This design would result in a collimator weight of approximately 18 kg (40 lbs) even with 2.5 cm lead.

One problem with this simple design for our system is that out-of-field activity will be able to penetrate through the aluminum side walls and interact in the crystal because of the small size of the detector. There are two solutions to this issue; 1) use a cone shape collimator, or 2) cover the entire aluminum box in lead. The cone design will weigh approximately 39 kg (86 lbs) and the covered box design will weigh approximately 50 kg (110 lbs) if 2.5 cm of lead are used. By reducing the thickness to 1.6 cm, the weight of the cone is approximately 25 kg (55 lbs) and the box is approximately 34 kg (75 lbs). The cone design is more efficient than the covered box design and will be used in our design.

Future work will involve the fabrication and testing of the pinhole collimator with our mobile system. We will compare actual data to the theoretical predictions and the GATE simulations.

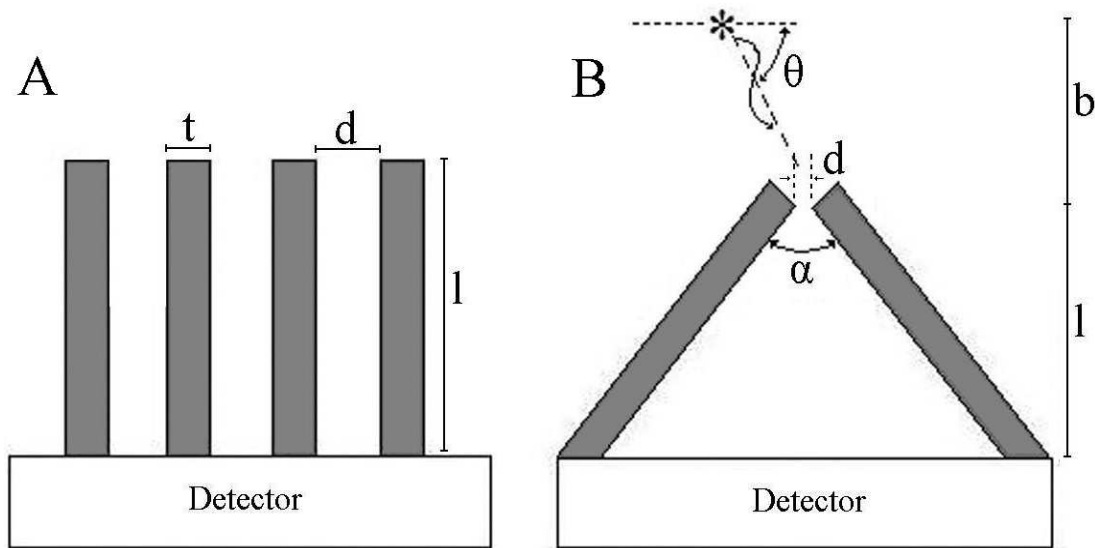


Figure 5-1. Design parameters for a parallel hole collimator and pinhole collimator. A) Parallel hole collimator. B) Pinhole collimator.

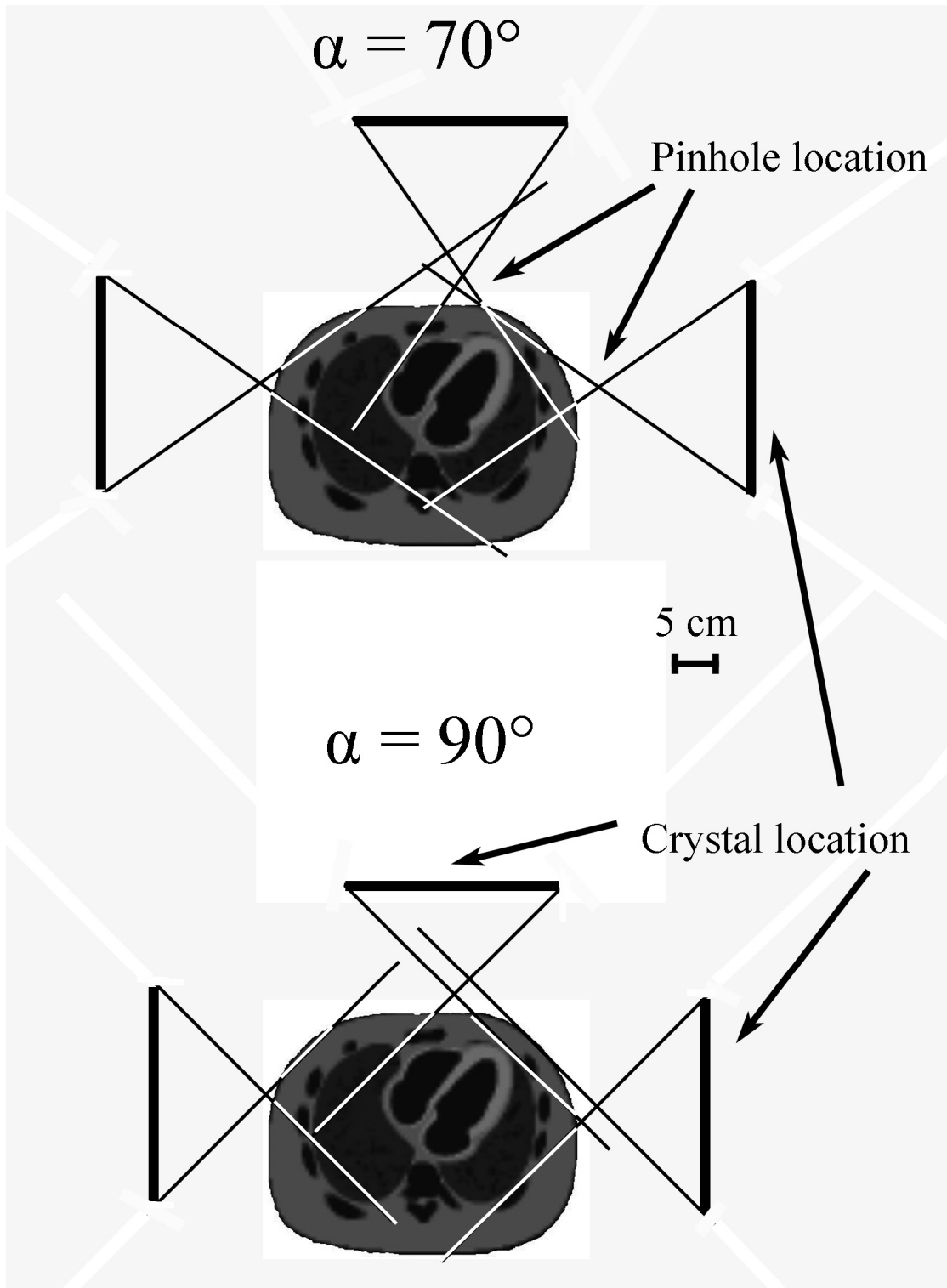


Figure 5-2. Scale drawing demonstrating the effect of different acceptance angles on the field-of-view at different projection angles. Notice the shortened focal length with the 90° acceptance angle.

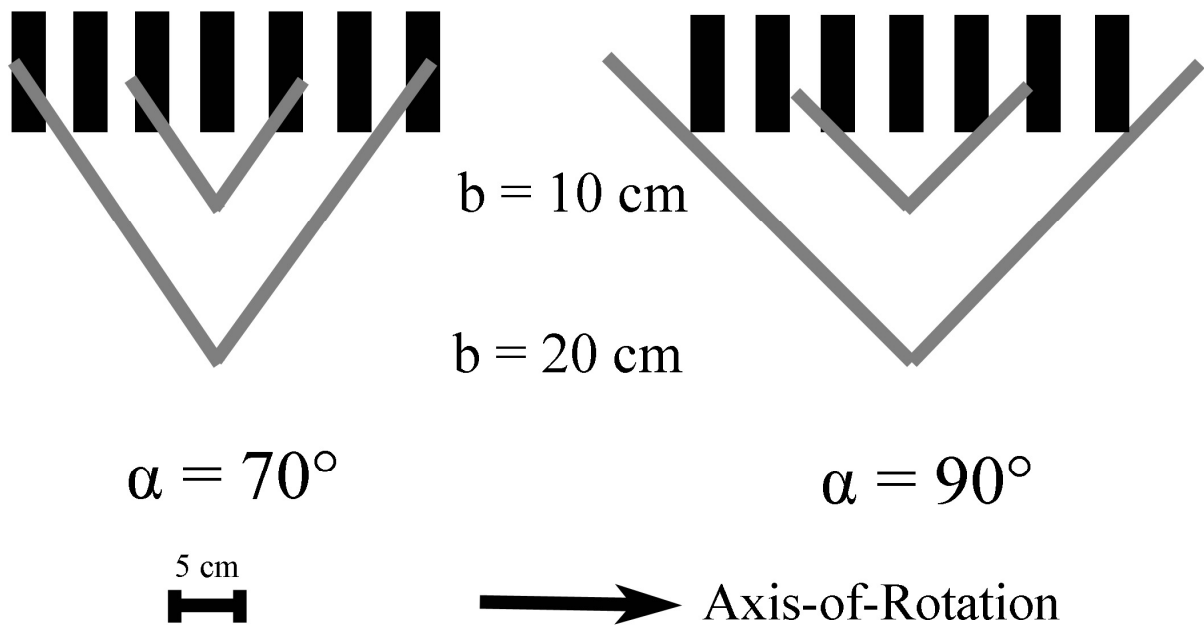


Figure 5-3. Scale drawing demonstrating the FOV size with two different collimator acceptance angles and the Defrise phantom at different source-to-collimator distances.

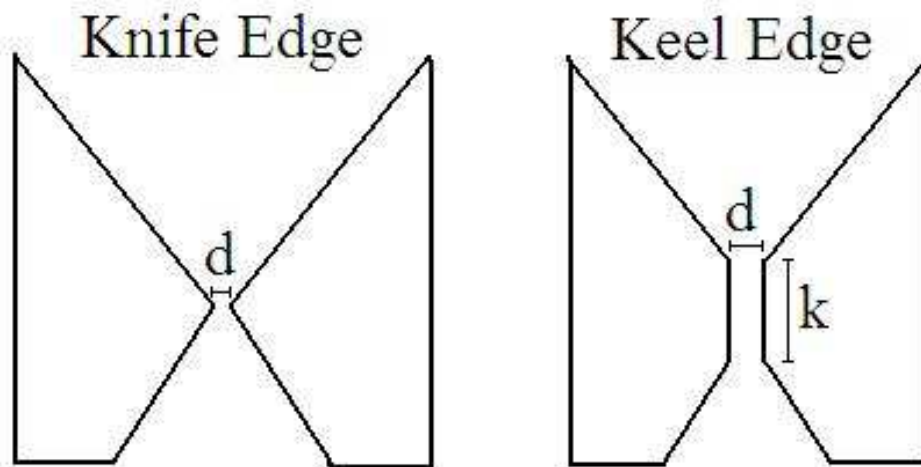


Figure 5-4. Difference between a knife edge and keel edge pinhole collimator. The keel thickness (k) can be changed to help reduce the penetration photons.

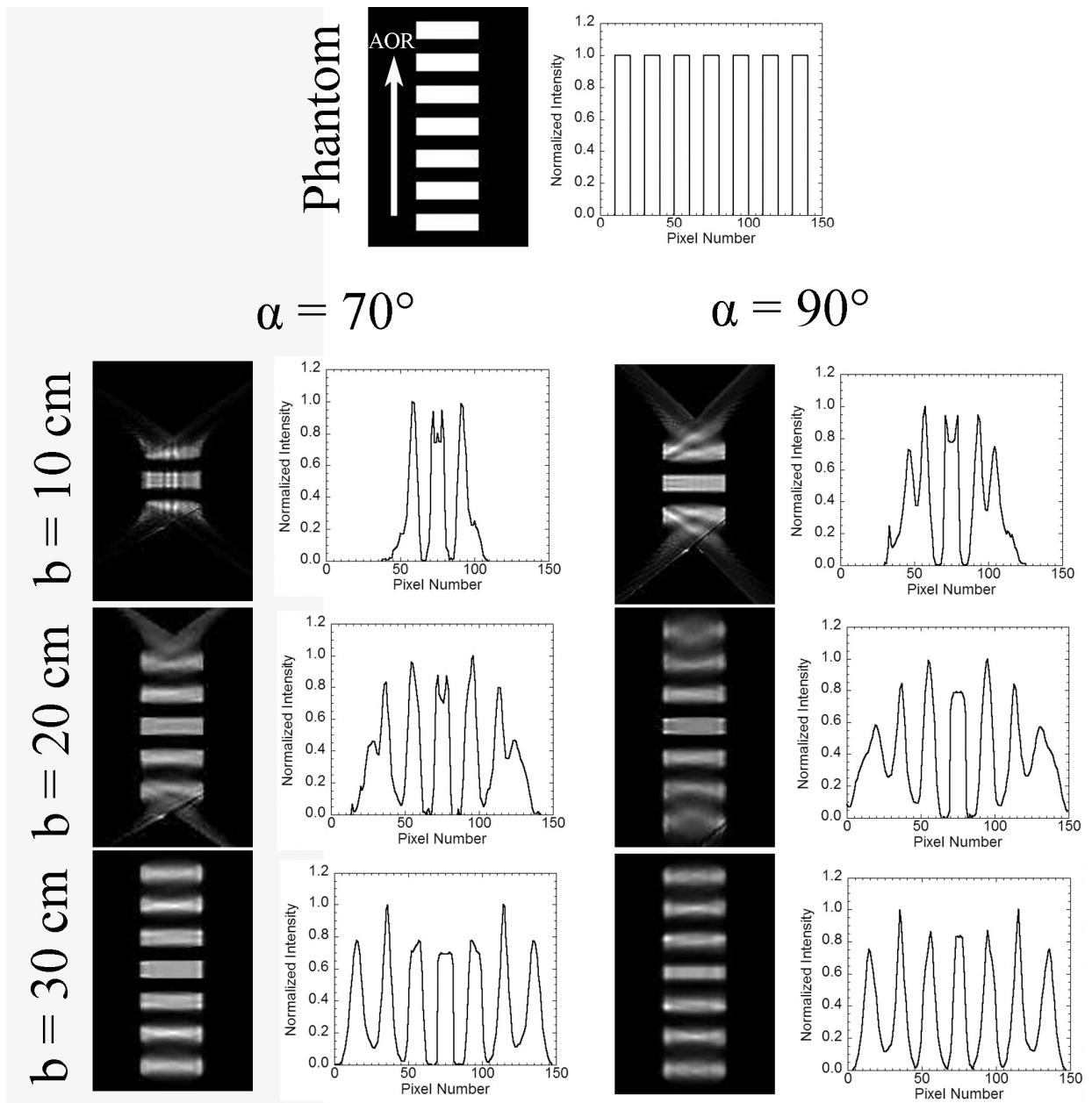


Figure 5-5. Coronal slices and profiles along the axis-of-rotation from the Defrise phantom reconstructions with two acceptance angles and varying radius-of-rotations. The white arrow indicates the direction of the axis-of-rotation.

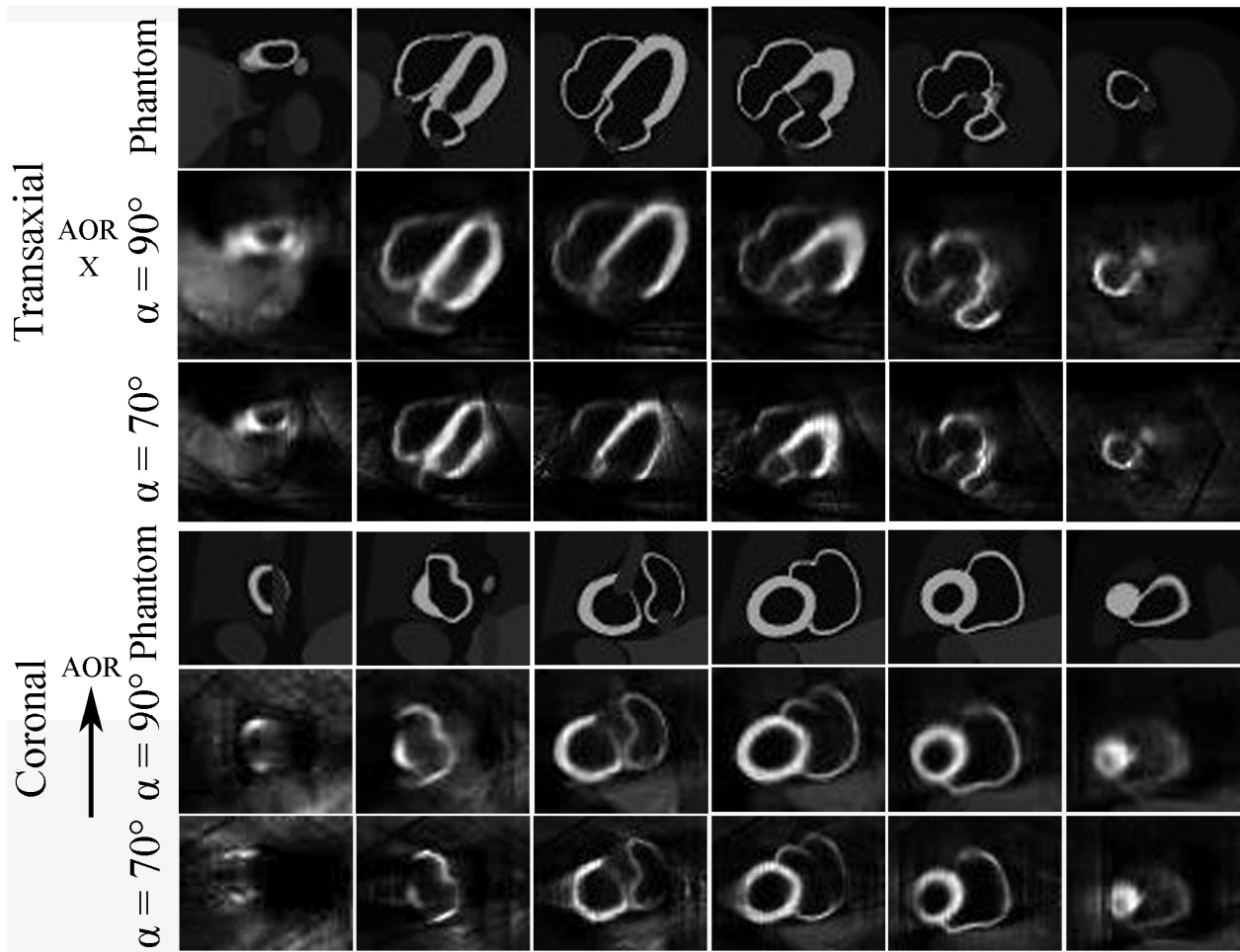


Figure 5-6. Transaxial and coronal slices from the NCAT phantom simulations with 70° and 90° acceptance angles. The axis-of-rotation (AOR) is indicated by the arrow (into the page for the transaxial slices).

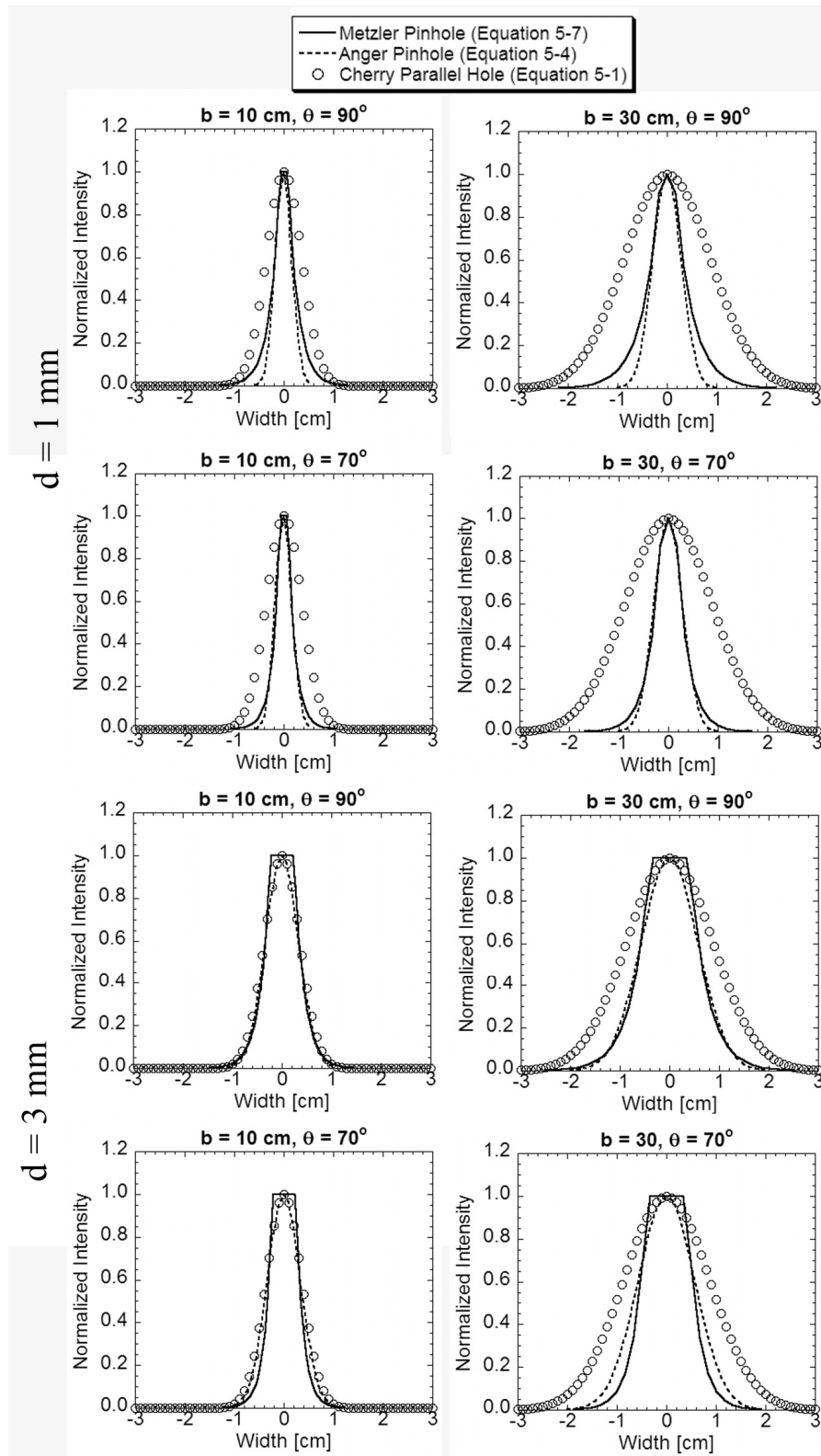


Figure 5-7. Theoretical profiles for both pinhole and parallel hole collimators with two different pinhole diameters at different locations in the FOV.

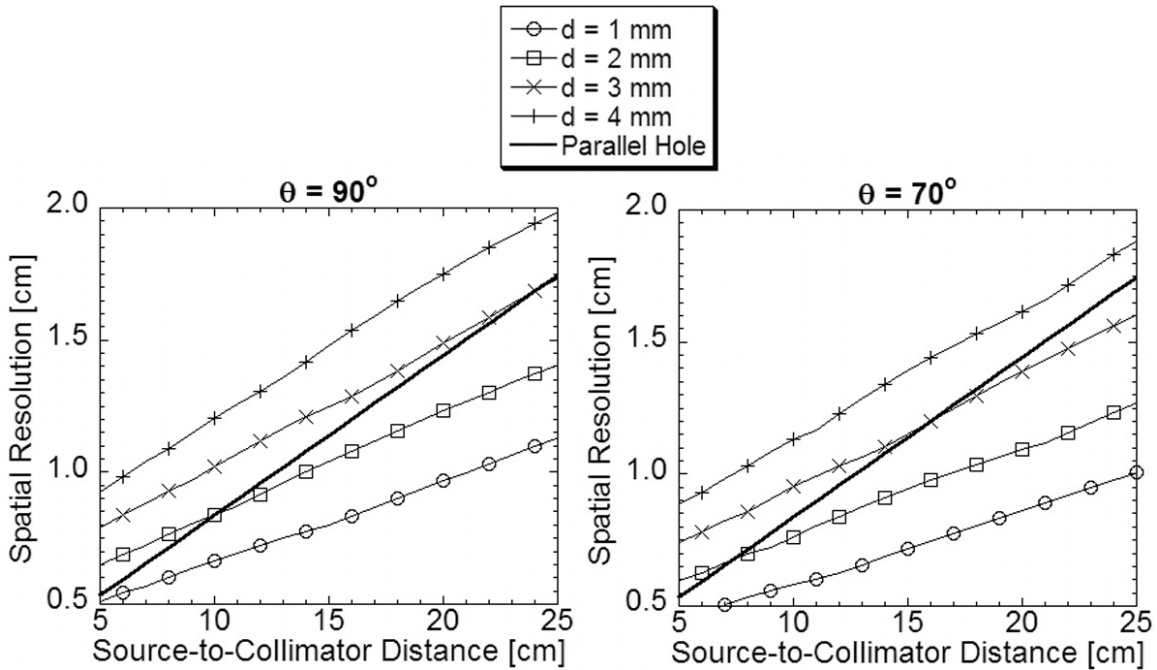


Figure 5-8. Theoretical spatial resolution on the object plane of our parallel hole collimator compared to Metzler, *et al.*'s pinhole collimator prediction with varying source-to-collimator distances.

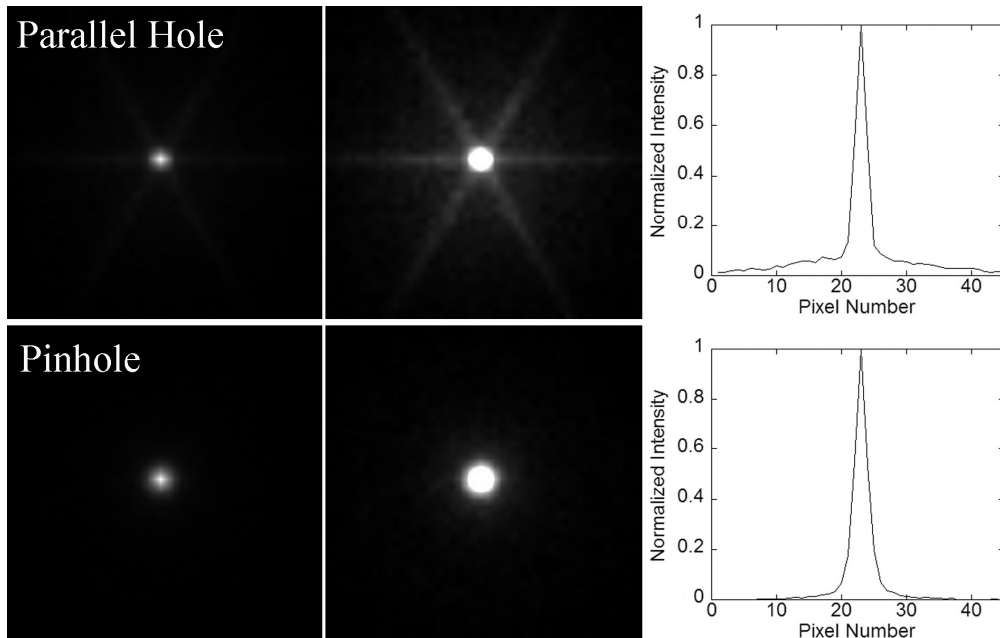


Figure 5-9. GATE simulations of a point source with both the parallel hole and pinhole hole collimator. Images shown without windowing, windowed to 25% of the maximum pixel intensity, and with a horizontal profile. Notice the star pattern visible with the parallel hole collimator.

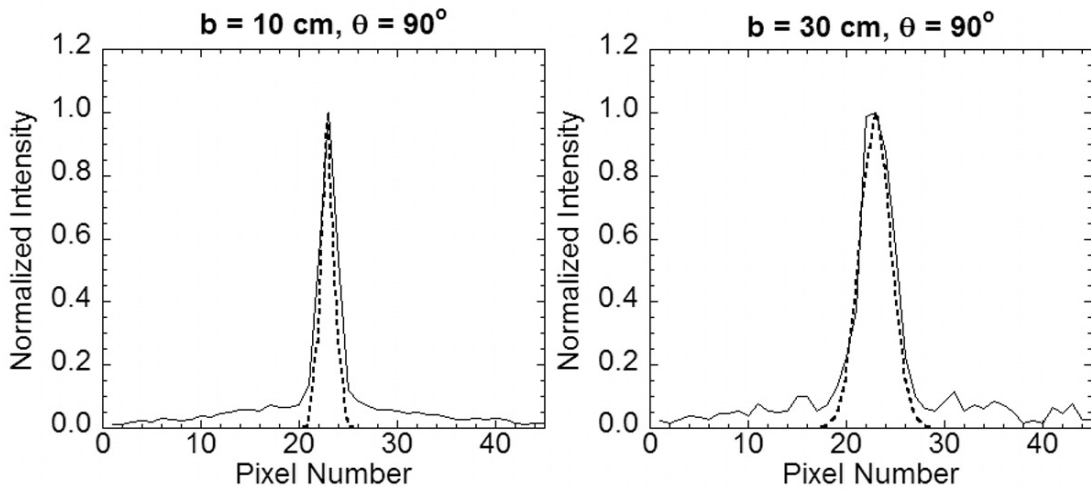


Figure 5-10. Theoretical profile predicted by Cherry, *et al.* (dashed line) and the horizontal GATE profile (solid line) of a point source in air with varying source-to-collimator distances for the parallel hole collimator on the image plane.

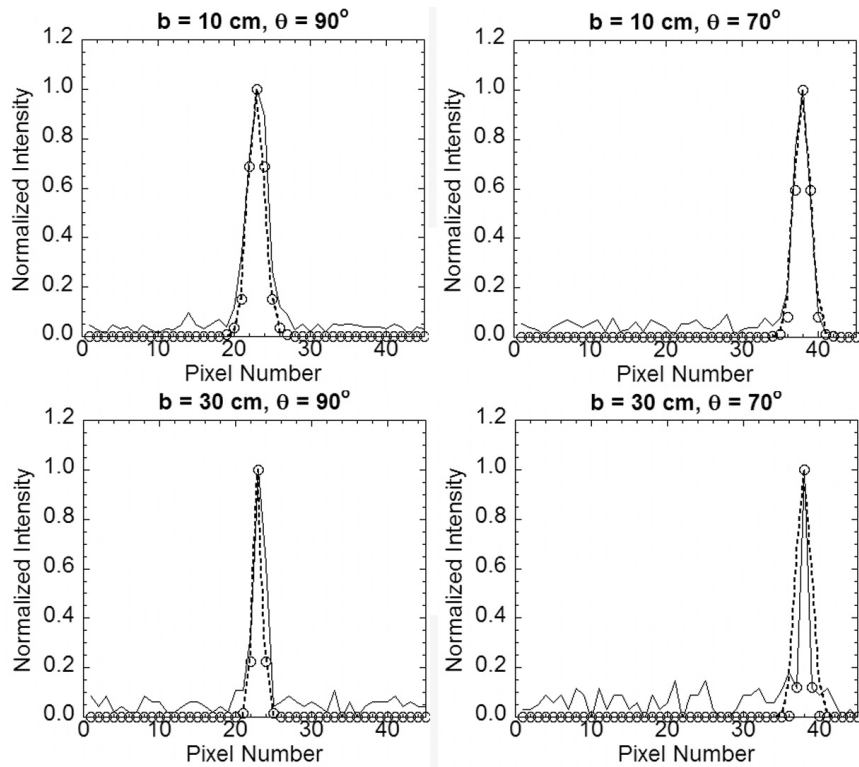


Figure 5-11. Theoretical profiles predicted by Anger (dashed line) and Metzler, *et al.* (open circles) and the horizontal GATE profile (solid line) of a point source in air with varying source-to-collimator distances and photon entry angles for the pinhole collimator on the image plane.

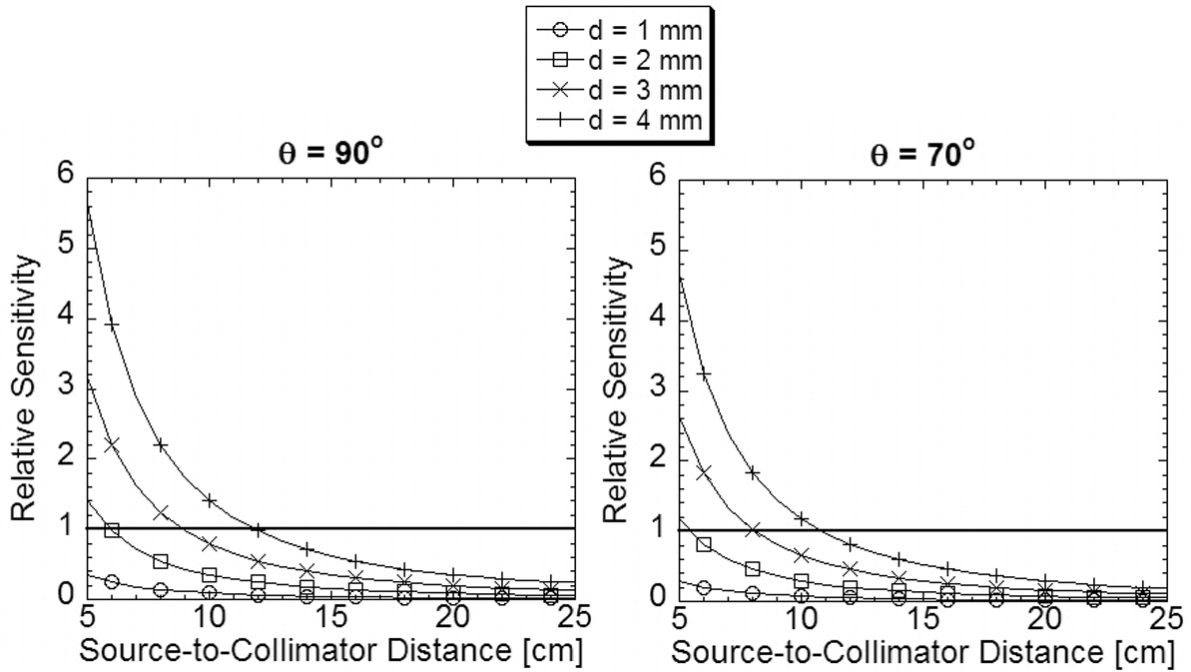


Figure 5-12. Metzler, *et al.*'s theoretical pinhole collimator sensitivity relative to that of our parallel hole collimator over varying source-to-collimator distances.

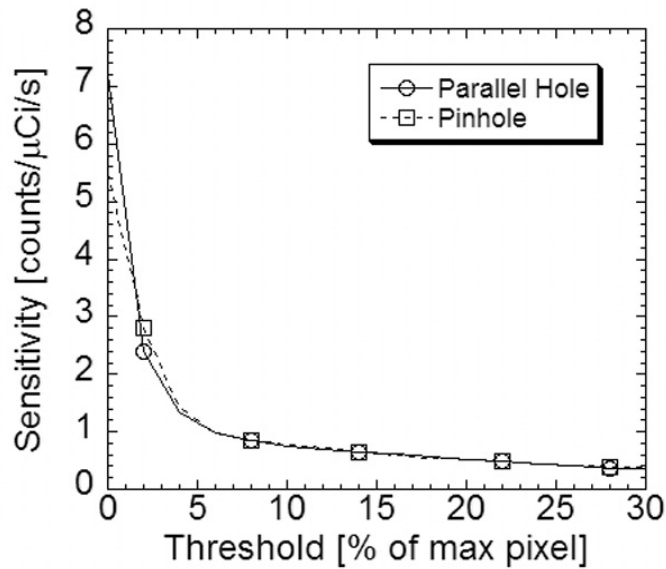


Figure 5-13. GATE sensitivity of the parallel hole and pinhole collimator at $b = 10$ cm with different degrees of thresholding demonstrating the effect of septal penetration photons.

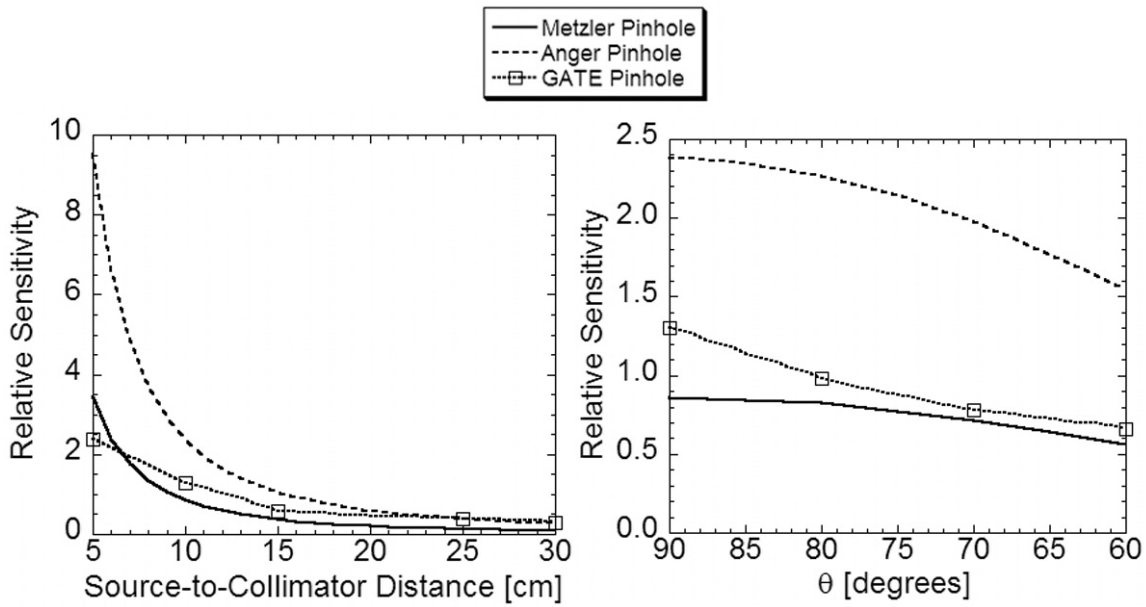


Figure 5-14. Theoretical and GATE sensitivities relative to that of the theoretical parallel hole collimator with different source-to-collimator distances and photon entry angles. For the varying distance plot, $\theta = 90^\circ$. For the varying θ plot, $b = 10$ cm.

Table 5-1. Source-to-collimator distances at each projection angle obtained from an acquisition with the mobile system using a dynamic cardiac phantom.

Projection	Source-to-Collimator Distance [cm]	Projection	Source-to-Collimator Distance [cm]	Projection	Source-to-Collimator Distance [cm]
1	16	10	7	19	14
2	14	11	7	20	16
3	13	12	7	21	17
4	12	13	7	22	19
5	11	14	8	23	20
6	10	15	8	24	22
7	9	16	10	25	25
8	8	17	11		
9	8	18	13		

Table 5-2. Reconstructed spatial resolution and sensitivity from GATE simulations for both the parallel hole and pinhole collimators.

Collimator	ROR	Spatial Resolution [cm FWHM]		Sensitivity [cts/ μ Ci/s]
		Coronal	Axial	
Pinhole	Varying	1.43	1.48	0.14
	10 cm	1.18	1.22	0.18
	15 cm	1.36	1.46	0.12
	20 cm	1.52	1.70	0.08
	25 cm	1.79	1.92	0.03
Parallel Hole	Varying	1.65	1.69	0.40
	10 cm	1.40	1.47	0.41
	15 cm	1.62	1.67	0.38
	20 cm	1.94	1.99	0.39
	25 cm	2.12	2.16	0.38

Table 5-3. Average sensitivity with the pinhole and parallel hole collimators calculated after eliminating the final projection angles with long source-to-collimator distances.

Collimator	# Projection Angles Used	Average Sensitivity [cts/ μ Ci/s]
Pinhole	25	0.14
	24	0.14
	23	0.15
	22	0.15
	21	0.16
	20	0.17
Parallel Hole	25	0.40
	24	0.40
	23	0.40
	22	0.40
	21	0.40
	20	0.40

CHAPTER 6 RADIATION DOSE TO SURROUNDING AREAS

6.1 Introduction

One aspect of the clinical feasibility of this mobile system that has not been addressed is the radiation dose to patients and staff in the surrounding areas during an acquisition. A typical nuclear medicine suite is designed with shielding to protect the public by attenuating the radiation emitted from the patient during a scan. Access to the rooms is also controlled to prevent people from entering and receiving unnecessary dose. In the environment this system will be used, the rooms will not be shielded and access will not be restricted.

There are three ways to reduce radiation dose; 1) decrease the time exposed, 2) increase the distance from the source, and 3) add shielding to attenuate the radiation. In our situation, time and distance cannot be altered since other patients in the area will also be immobile. The options we have to reduce the dose to others are to bring in portable shielding or reduce the activity administered to the patient. Reducing the activity from a typical clinical level will reduce the dose to any staff and patients in the ICU and surrounding rooms but is not ideal because the quality of the image will be reduced. Portable shielding does not require a reduction in administered activity but only reduces the dose to patients and staff in the ICU, not in surrounding rooms. All possible options will be considered to ensure the dose is below the regulatory limit to all individuals.

6.2 Methods

6.2.1 Regulatory Limits

Regulatory limits for radiation doses are set by the federal government. The limits are established in the code of federal regulations 10 CFR part 20. The regulatory limit is different for occupational radiation workers than it is for the general public. 10 CFR 20 states that the

effective dose equivalent in an unrestricted area (i.e. the general public) must be less than 1 milli-Sievert/year (mSv/year) which implies a weekly limit of 20 micro-Sieverts (μSv).

The occupational dose limit is higher at 50 mSv/year (a weekly limit of 1 mSv). This is the limit in a restricted area such as a designated nuclear medicine suite. The limit is higher to allow occupational workers to perform their job since they can be exposed to radiation in their work environment. Since we will be acquiring in an ICU environment with patients and staff that are members of the general public, we must meet the regulatory standards for an unrestricted area although we will also calculate the dose to the occupational workers that will be operating the system.

6.2.2 ^{18}F -FDG Effective Dose Calculation

We will first focus on the dose from a cardiac viability exam using ^{18}F -FDG. The reason for this is that the high energy, 511 keV photons require more shielding and produce a higher exposure rate than $^{99\text{m}}\text{Tc}$ photons at 140 keV.

We will use the methodology proposed by the American Association of Physicists in Medicine (AAPM) Task Group 108 [44]. In a typical nuclear medicine procedure, the patient receives an injection containing the radiopharmaceutical and then is held in a room for about an hour while the organ of interest metabolizes the compound. The patient is then brought to the scanner and the acquisition is performed. In our case, the patient will not be moved throughout the entire procedure so we modified the method in [44] accounting for the fact that all steps occur at the same location.

We will calculate the effective dose in three parts; 1) one hour uptake period, 2) one hour acquisition period, and 3) a decay period. For the initial dose calculations, will first assume that there is no shielding and the patient is administered a typical dose of 555 mega-Becquerels

(MBq) (15 mCi). We will also assume that in a typical ICU, the beds are 3 m apart (Figure 6-1). This will let us determine what doses, if any, are above the regulatory limit.

We will consider four groups of people who will be exposed; 1) other immobile patients in the ICU and surrounding rooms, 2) occupational staff operating the mobile system, 3) nurses and other staff members who are not occupational workers but are directly involved with patient treatment and must approach the patient during the acquisition, and 4) staff in adjacent rooms and ICU who are not directly involved with treating the patient. Figure 6-1 shows the layout of an ICU showing the different distances that we used for patients and staff that could be in the vicinity of the patient.

First, we will calculate the total effective dose accumulated every hour at different distances from the patient each hour through the uptake, acquisition, and decay periods. This will allow us to calculate the total effective dose integrated over the entire procedure. The total integrated dose is the dose to immobile patients in the ICU or in surrounding rooms. We can also use these values to determine the dose to staff in surrounding rooms and to staff in the ICU who are not dealing directly with the patient. From Figure 6-1, typical distances for surrounding rooms are 4 m for rooms above and below the ICU and 2 m for rooms adjacent to the ICU [44].

For the dose calculation to the staff not directly involved in treating the patient, we will only integrate the dose over the first ten hours of the acquisition. This is to account for the worst case scenario where their shift starts during the uptake period when the dose rate is the highest. We assume a ten hour shift to account for a staff member working overtime or a long ICU shift. We will then compare this dose to the 20 μSv weekly limit for the general public to determine how many studies could be performed each week in a single ICU before the regulatory limit was met.

Next, for the staff directly involved with patient treatment, we will again assume a ten hour shift. Taking the dose calculated at 1 m, we determined the amount of time each hour the individual can be at this distance the patient and still stay below the regulatory limit. This will allow us to calculate the amount of time allowed for non-occupational ICU staff to approach the patient to monitor their vital signs and for the occupational staff performing the acquisition with the mobile system to be near the patient positioning the detector heads. We will assume that all staff members move back to a distance of at least 4 m when not monitoring the patient or positioning the mobile system. We will compare the dose to the 20 μSv weekly limit for the general public and the 1 mSv weekly occupational limit.

6.2.2.1 Uptake period

The effective dose (D) to a point during the initial uptake period of 1 hour is defined by Equation 6-1 where A_0 is the initial activity, t_U is the uptake time, R_{tU} is the dose reduction due to the radioactive decay of the ^{18}F (0.91, 0.83, 0.76 for $t = 30, 60,$ and 90 min respectively), and d is the distance from the patient [44].

$$D(t_U) = 0.092 \frac{\mu\text{Sv} \cdot \text{m}^2}{\text{MBq} \cdot \text{h}} \times A_0 (\text{MBq}) \times t_U (\text{h}) \times \frac{R_{tU}}{d(\text{m})^2} \quad (6-1)$$

The effective dose during this period will be the highest so it is imperative that staff continually monitors the patient to ensure that no one is close to the patient for an extended period of time, including the nurses and occupational workers monitoring the patient. Regulations state that an area is a high radiation area and access must be controlled is the dose rate is greater than 1 mSv/h at 30 cm from the source. For a 555 MBq injection, the dose rate at 30 cm is 0.6 mSv/h. This means access does not need to be restricted but signs do need to be posted declaring the area a radiation area. A radiation area is defined as a dose rate at 30 cm from the source of at least 50 $\mu\text{Sv}/\text{h}$.

6.2.2.2 Acquisition period

Equation 6-2 defines the effective dose during the acquisition time. In TG 108, a dose reduction of 15% is assumed due to the excretion of some of the radiopharmaceutical through urine during the uptake period [44]. In a nuclear medicine clinic, this excretion is usually forced. This is not possible with patients in an ICU so we cannot assume this 15% decrease but we can account for the decay that occurred during the uptake time with the factor F_U (Equation 6-3). As with Equation 6-1, t_I is the acquisition time and R_{tI} is the dose reduction due to radioactive decay during the acquisition time. The acquisition time with this system would be around 60 min but could be extended into the decay period if required.

$$D(t_I) = 0.092 \frac{\mu\text{Sv} \cdot \text{m}^2}{\text{MBq} \cdot \text{h}} \times A_0 (\text{MBq}) \times F_U \times t_I (\text{h}) \times \frac{R_{tI}}{d(\text{m})^2} \quad (6-2)$$

$$F_U = \exp\left[-0.693 \times \frac{t_U (\text{min})}{110}\right] \quad (6-3)$$

One consideration during the acquisition time is that the nurses must still monitor the patients every few minutes. As with the uptake period, their time spent near the patient must be reduced as much as possible. To help reduce the time near the patient, the detectors can be moved away from the patient between projections to allow patient access since the system requires manual positioning at each projection. This will increase the overall acquisition time but could reduce the time the nurses spend near the patient.

6.2.2.3 Decay period

We calculated the accumulated dose every hour after the acquisition period until the dose rate at 0.5 m was less than 1 $\mu\text{Sv}/\text{h}$. We chose this dose rate because it was lower than the regulatory limit and if we included the remaining integrated dose into the total integrated dose, it did not significantly effect the result (remaining integrated dose \sim 1% of total integrated dose).

It took 15 hours for ^{18}F and 29 hours for $^{99\text{m}}\text{Tc}$ to reach this level. Since we did not account for any activity excreted, these times could be shorter and the dose during this period could be slightly overestimated since the patient most likely will urinate at least once in this time period. The effective dose during the decay time was calculated using Equations 6-2 and 6-3 with F_U recalculated to account for the radioactive decay.

6.2.3 $^{99\text{m}}\text{Tc}$ Effective Dose Calculation

The exposure rate from the 140 keV $^{99\text{m}}\text{Tc}$ photons is much lower than for 511 keV ^{18}F annihilation photons. This can be clearly seen when comparing the gamma ray exposure rate constants for ^{18}F which is $0.188 \mu\text{Sv m}^2/\text{MBq h}$ and $^{99\text{m}}\text{Tc}$ which is $0.033 \mu\text{Sv m}^2/\text{MBq h}$ [45]. This is the maximum dose received to a slab of tissue with a broad beam of photons.

For the dose calculation with ^{18}F in [44], the dose rate is calculated from the effective dose rate constant ($0.143 \mu\text{Sv m}^2/\text{MBq h}$) and is then reduced to account for attenuation in the body (36%) to the $0.092 \mu\text{Sv m}^2/\text{MBq h}$ seen in Equations 6-1 and 6-2. Following the method in [44], we calculated the effective dose equivalent for $^{99\text{m}}\text{Tc}$, using the effective dose rate constant of $0.018 \mu\text{Sv m}^2/\text{MBq h}$. We also accounted for attenuation in the body with the $^{99\text{m}}\text{Tc}$ photons and we calculated the total body absorption factor at 140 keV to be 38%. This reduces the dose rate constant from $0.018 \mu\text{Sv m}^2/\text{MBq h}$ to $0.011 \mu\text{Sv m}^2/\text{MBq h}$.

For our dose calculation with $^{99\text{m}}\text{Tc}$, we used this dose rate constant of $0.011 \mu\text{Sv m}^2/\text{MBq h}$ and substituted this into Equations 6-1 and 6-2. Also, we did not include the dose reduction factors (R_t) during the uptake, acquisition, or decay time because of the longer half-life (6.01 hours) of $^{99\text{m}}\text{Tc}$. We only considered decay using F_U from Equation 6-3. The average activity administered to the patient for a procedure with $^{99\text{m}}\text{Tc}$ is about the same as with ^{18}F so we will assume an initial activity of 555 MBq. As with ^{18}F , we calculated the doses every hour until the dose rate at 0.5 m was less than $1 \mu\text{Sv/h}$.

6.2.4 Effective Dose Reduction Options

As stated earlier, there are three ways to reduce dose; time, distance, and shielding. For other immobile patients we cannot change the time and distance to the source but we can bring in portable shielding and we can reduce the initial activity administered to the patient. For members of the staff directly treating the patient, we can reduce time and distance as much as possible but they will still be required to approach the patient during the acquisition. It is always good to practice the as low as reasonably achievable (ALARA) principle so the effective dose considering both of these options will be calculated with the same method as for the unshielded case.

6.2.4.1 Activity reduction

Although reducing the activity administered to the patient is a simple means of reducing dose, there will be degradation in the quality of the image. The main cause of image degradation would be increased noise from reduced counts. We suspect that one way to alleviate this effect is to increase the scan time. Since the patient is immobile and we have assumed a long decay time, a longer scan time with lower injected activity should reduce the effective dose to surrounding areas while maintaining the image quality.

Also, we suspect that the fact that FDG follows metabolic processes will also help to reduce image degradation with lower injected activity (this theory does not apply to ^{99m}Tc acquisitions). In a normal clinical situation after injection, the patient must be kept in a resting state since the tracer will be metabolized in active skeletal muscle. This minimizes the uptake in skeletal muscle, but the patient still must walk to the scanner and will move other extremities so some FDG will inevitably be metabolized in the skeletal muscle. Since patients in the ICU are immobile, the only muscle working is the myocardium and therefore the FDG uptake in the myocardium will be as high as possible. This will help reduce the noise in the image since more

activity is concentrated in the myocardium. Because of the complexity of the uptake of the radiotracers, the total effect of reducing the activity on the overall image quality cannot be determined until further studies are done in a clinical environment.

6.2.4.2 Portable shielding

One of the driving factors for this study is the fact that an ICU does not have shielding built into the walls to reduce dose to surrounding rooms. Without extensive construction we cannot shield adjacent rooms, but we will consider two different portable radiation shields; one for other patients, and one for staff in the ICU. There are commercially available portable shields that can be wheeled into place between patient beds or next to the bed to shield the staff directly treating the patient. A shield could also be custom made by purchasing a sheet of lead and attaching wheels. For this calculation, we will assume that the shields are a lead sheet on wheels to study the effect of increasing shield thicknesses in a simple calculation. The shield for the other patients will be 1.8 m wide by 1.8 m tall (6 ft × 6 ft). This shield could be rolled into place between patients beds both for dose reduction and for privacy.

The lead shield for the workers will be 0.9 m wide and 1.8 m tall (3 ft × 6 ft). This shield will also be on wheels to allow for easy access to the patient for detector positioning and monitoring of the patient's vital signs. For both shields we will calculate dose to ICU staff and patients using shield thicknesses of 1 mm up to 15 mm for both ^{18}F and $^{99\text{m}}\text{Tc}$. We will compare the reduction in dose and the weight of each shield design.

6.3 Results

6.3.1 Dose to Other Immobile Patients

We first calculated the total effective dose integrated over the uptake, acquisition, and decay periods at various distances from the patient with a typical 555 MBq injection and no shielding. The results for both ^{18}F and $^{99\text{m}}\text{Tc}$ can be seen in Figure 6-2. Remember that 10 CFR

20 states that the effective dose to the general public must be less than 20 μSv per week.

Therefore, it is possible to perform one exam per week with an immobile patient at least 2 m away with $^{99\text{m}}\text{Tc}$ and with a patient at least 3 m away with ^{18}F without exceeding the regulatory dose limit.

As expected, the first two hours following the injection are the most critical to ensure that no people remain close to the patient for an extended period of time. Comparing these results to Figure 6-1, it is possible for a patient to be at a distance of 2 m in an adjacent room. This means that with ^{18}F , that patient's dose would exceed the regulatory limit so some means of reducing the dose must be implemented.

6.3.2 Dose to Staff not Treating the Injected Patient

The doses to staff members not directly involved with the injected patient's treatment were calculated by integrating the dose over the first ten hours of the procedure. The results can be seen in Figure 6-3. To stay below the regulatory limit, the staff member must be at least 1.5 m from the patient for a procedure with $^{99\text{m}}\text{Tc}$ and 2.5 m from the patient for a procedure with ^{18}F . Comparing these results to Figure 6-1, staff in rooms above and below the ICU would be below the regulatory limit because they would be at a distance of about 4 m. Staff working the nurse's station in the ICU would be at a distance of about 3 m which would keep the dose below the regulatory limit for procedures with either isotope. For these staff members, one acquisition could be done per week in the ICU without exceeding the regulatory dose limit.

As with the immobile patient dose calculation, it would be possible for a staff member to be in an adjacent room at a distance of 2 m from the patient. This would not be an issue for one acquisition per week with $^{99\text{m}}\text{Tc}$ but the staff member would exceed the dose limit for a procedure with ^{18}F so this dose must somehow be reduced.

6.3.3 Dose to Non-Occupational Staff Directly Treating the Patient

It is necessary for non-occupational staff members in the ICU to approach the patient during an acquisition to monitor vital signs and treat the patient. To account for this, we took the dose calculated at a distance of 1 m from the patient each hour for the first ten hours of the procedure and recalculated the dose based on the amount of time the staff member would be near the patient. The results of the calculation for the first five hours can be seen in Figure 6-4. We also summed the dose over the entire ten hour period assuming that the staff member monitors the patient for the same amount of time each hour and also included the effective dose received at a distance of 4 m over the same ten hour period (8.2 μSv with ^{18}F and 2.4 μSv with $^{99\text{m}}\text{Tc}$). These results are found in Figure 6-5.

To stay below the regulatory limit, the staff can only be near the patient for about 5 minutes every hour for ^{18}F procedures and about 25 minutes every hour for $^{99\text{m}}\text{Tc}$ procedures. This is assuming that the same amount of time is spent near the patient each hour and that they are 4 m from the patient for the remaining time. Since the dose is higher in the first few hours, if the time near the patient during this period was reduced, more time could be spent near the patient later as the activity decayed away. Another observation with $^{99\text{m}}\text{Tc}$ procedures is that due to the long half life, the total dose to staff that will only be in the ICU for their ten hour shift is much lower than the dose to immobile patients who are exposed for over 20 hours. Overall, these results show that an acquisition can be done with both ^{18}F and $^{99\text{m}}\text{Tc}$ and keep the dose to non-occupational staff below the regulatory limit if the time spent near the patient is limited.

6.3.4 Dose to Occupational Staff in the ICU

As with the non-occupational staff dealing directly with the patient, the occupational staff working the mobile system must be near the patient to position the detectors at each projection angle. Unlike the non-occupational staff, the occupational staff will not have to monitor the

patient during the uptake time. For all other time periods, the doses in Figure 6-4 apply to the occupational staff except that the 10 CFR 20 limit is increased to 1 mSv per week. To determine how much time an occupational worker can spend near the patient, we recalculated the accumulated dose in the same manner as with the non-occupational workers but we eliminated the uptake period. The results are seen in Figure 6-6.

Since the regulatory limit to occupational workers is much higher, as long as the staff member stays at least 4 m from the patient during the uptake time, there would be no limit to the time spent near the patient using either ^{18}F or $^{99\text{m}}\text{Tc}$ for a single exam each week. Since we are following the ALARA principle and might want to perform more than one exam each week, this would never be the case limiting the time near the patient would mean that the dose to the occupational workers would be well below the regulatory limit.

6.3.5 Dose Reduction Techniques

It is always important to consider the ALARA principle to reduce the dose to the surrounding areas. From our calculations for a single, unshielded acquisition, we have shown that it is possible to perform one $^{99\text{m}}\text{Tc}$ procedure per week and not exceed the regulatory limit. For a single ^{18}F procedure, the dose to immobile patients or staff in an adjacent room could exceed the regulatory limit. To follow ALARA and to allow for exams to be done with this system, we must consider the two methods to reduce dose; 1) lower the activity administered to the patient and 2) bring in portable shielding.

6.3.5.1 Activity reduction

Because we exceed the regulatory limits in adjacent rooms that cannot be shielded easily, we will study how reducing the activity administered affects the dose in an adjacent room. Figure 6-7 demonstrates the effect of reducing the activity administered on the total effective dose to immobile patients or staff members that are in an adjacent room at a distance of 2 m.

The dose to an immobile patient is integrated over the entire procedure and the dose to staff is integrated over the first ten hours of the procedure. To reduce the dose below the regulatory limit for these personnel, the administered activity for acquisitions with ^{18}F must be reduced to about 325 MBq (9.2 mCi). It is not required to reduce the activity administered for $^{99\text{m}}\text{Tc}$ but this would limit the number of acquisitions per week to one. A reduction in activity to about 350 MBq would allow two exams to be done each week. It is important to remember that this is assuming a worst case scenario of a staff member with their desk or an immobile patient with their bed directly against the adjacent wall. Each ICU would have different layouts so a specific calculation would have to be completed before any acquisitions are started. If the hospital layout is different and the adjacent area is a hallway or other type of room (bathroom, storage, etc.), the occupancy factor would be lower and the limiting dose would be to the non-occupational workers in the ICU. For these individuals, it is possible to bring in portable shielding to reduce their dose.

6.3.5.2 Portable shielding

Since it is not possible to easily shield rooms surrounding the ICU, we will only consider portable shielding to reduce the dose to other patients and staff in the ICU. As a baseline to study the effect of shield thickness, we will assume that immobile patients in the ICU are 3 m from the injected patient and for the staff calculation we will assume that they must monitor the patient for 10 minutes every hour. Figure 6-8 shows the total effective dose for a typical activity of 555 MBq to ICU staff and other patients with different thicknesses of lead shielding. Table 6-1 shows the weights of both shields for the different lead thicknesses. Due to the higher attenuation coefficient of lead at lower energies, the shield was more effective for $^{99\text{m}}\text{Tc}$, even though it is not required. The shield for patients also is not necessary to keep the dose below the regulatory limit but we are following the ALARA principle and the shield should be used if at all

possible. To reduce the dose below the regulatory limit for non-occupational staff with an ^{18}F procedure, a shield thickness of 3 mm is required. Table 6-1 shows that this thickness would be the most practical due to the increase in weight as the shield thickness is increased.

6.4 Summary and Discussion

These calculations have shown that it is clinically feasible to acquire a tomographic image in an ICU environment and keep the dose to other patients and staff below the regulatory limit. The individuals receiving the highest dose are patients and staff in rooms adjacent to the ICU. Since it would be difficult to shield these staff members without moving beds or building shielding into the wall, it would be necessary to reduce the activity administered to perform an acquisition with ^{18}F . Even with the activity reduction, the number of acquisitions would be limited to one per week. With $^{99\text{m}}\text{Tc}$, without any reduction in activity, the dose to patients and staff in adjacent rooms would limit the number of acquisitions to one per week and an activity reduction would allow two acquisitions per week.

We suspect that our assumption for patients and staff in adjacent rooms is an overestimate for some hospital layouts and in that case the limiting dose is to the non-occupational staff in the ICU. The dose to the staff directly treating the patient or operating the mobile system is dependent on the time that they are near the patient. Portable shielding can also be used to reduce the dose. With ^{18}F , if we assume that the staff needs to be near the patient for 10 minutes every hour, we are limited to a single acquisition per week even with portable shielding. If this time was reduced, additional acquisitions could be done. With $^{99\text{m}}\text{Tc}$, we are limited to one acquisition per week in an unshielded procedure but with shielding this number becomes much higher.

Keeping ALARA in mind, it is important to note that the dose close to the patient is above the regulatory limit and precautions should be made that no individual is close to the patient for

an extended period of time, especially during the uptake period when the activity is the highest. Also, removal and proper disposal of the patient's urine is necessary since it is also radioactive and will help reduce the dose in the surrounding areas. Furthermore, for any procedure to be done in an ICU, radiation training would be required for all staff, especially the non-occupational workers required to directly treat the patient.

This calculation made several assumptions to prove the concept of acquiring a tomographic image in an ICU environment. Before any clinical procedures are performed, this calculation must be redone accounting for the specific layout of the hospital and ICU and for the distances staff will be from the injected patient. Each acquisition will be different and the number of acquisition per week will have to be closely monitored. This being said, the methodology used here should provide a template for future dose calculations with this mobile system.

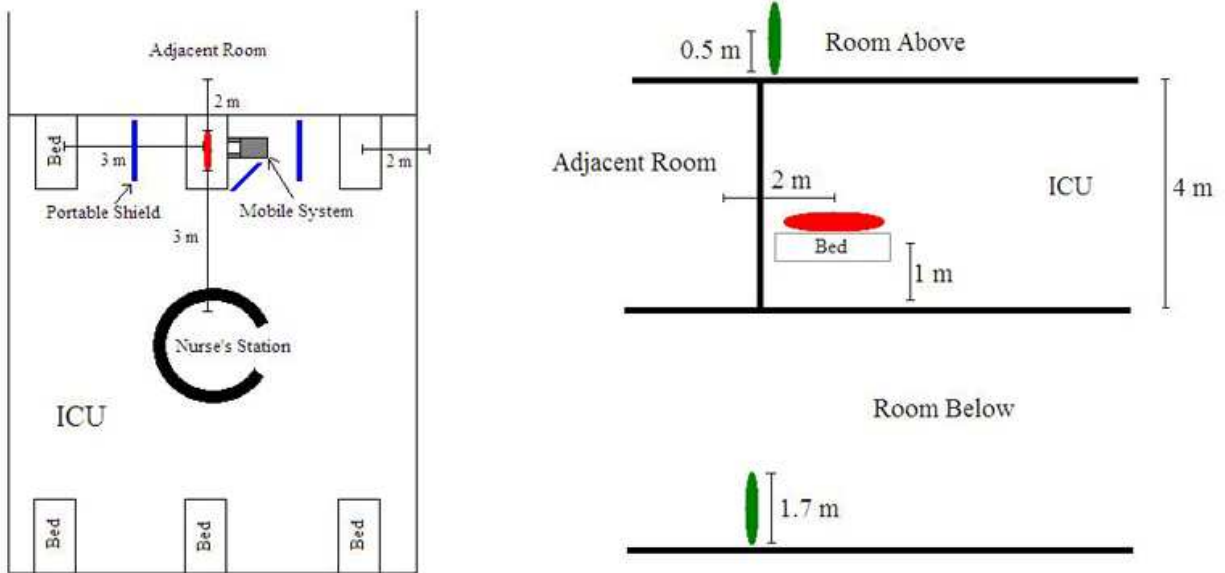


Figure 6-1. Top and side views of the distances assumed in the ICU for the dose calculation. The patient is red, portable shields are blue, and staff are green.

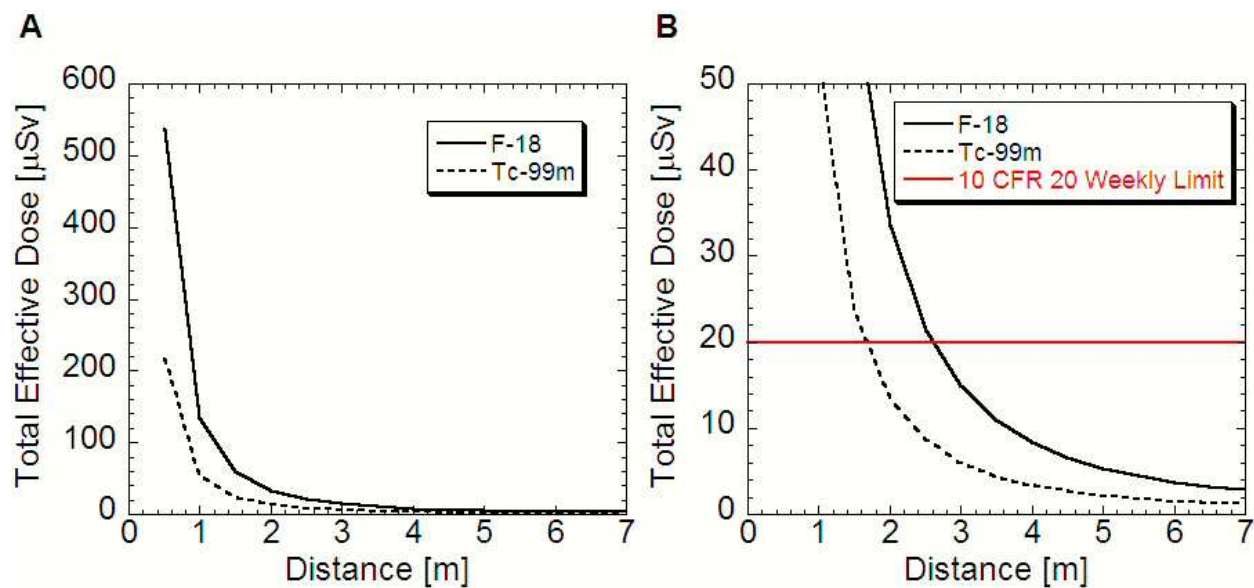


Figure 6-2. Total effective dose per exam integrated over all time periods at various distances from a patient for acquisitions with both ^{18}F and $^{99\text{m}}\text{Tc}$. A) Full range of data and B) Zoomed in to show the dose with respect to the 10 CFR 20 weekly limit.

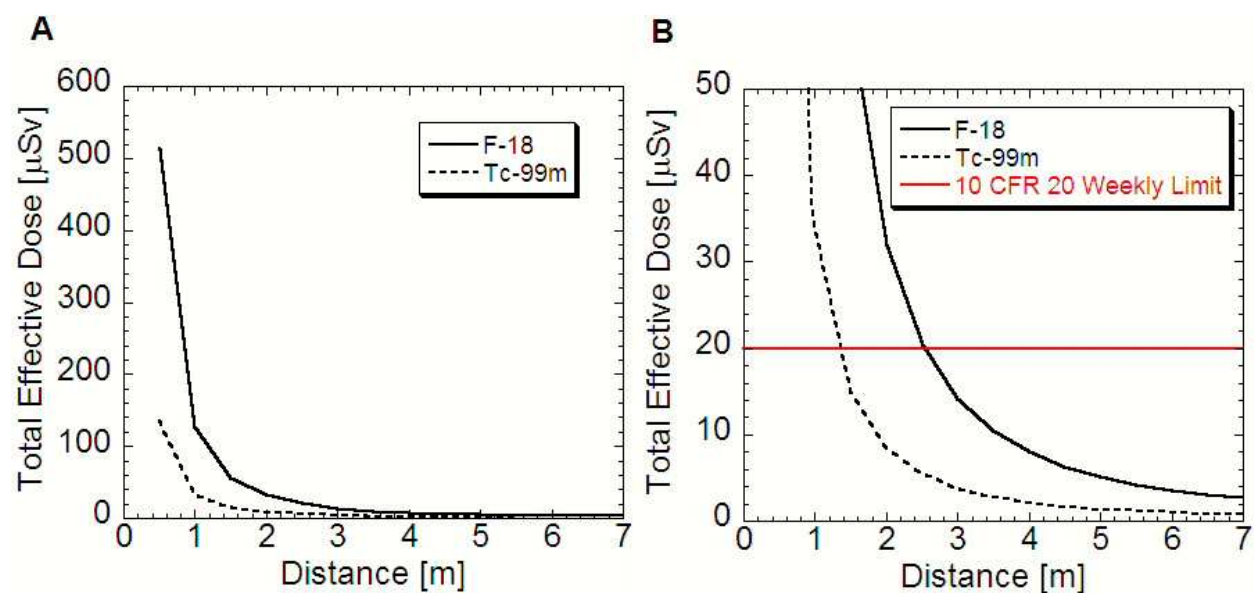


Figure 6-3. Total effective dose per exam integrated over the first ten hours of the procedure at various distances from a patient for acquisitions with both ^{18}F and $^{99\text{m}}\text{Tc}$. A) Full range of data and B) Zoomed in to show the dose with respect to the 10 CFR 20 weekly limit.

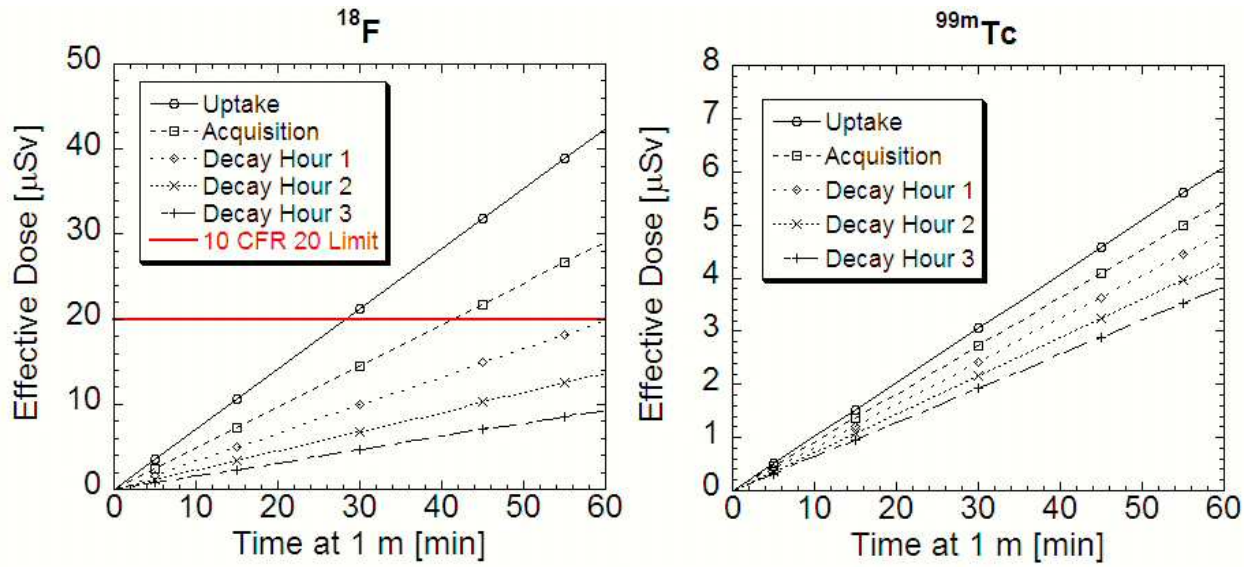


Figure 6-4. Effective dose for staff directly treating the patient based on the time spent at 1 m from the patient for acquisitions with both ^{18}F and $^{99\text{m}}\text{Tc}$.

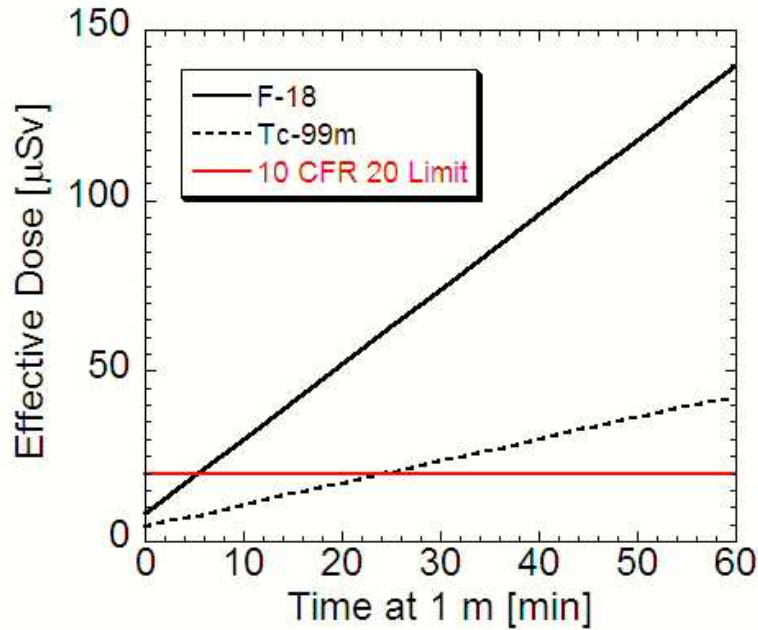


Figure 6-5. Total effective dose during a ten hour shift for non-occupational staff directly treating the patient assuming that the time spent at 1 m is the same every hour and the rest of the time is spent at least 4 m from the patient for acquisitions with both ^{18}F and $^{99\text{m}}\text{Tc}$.

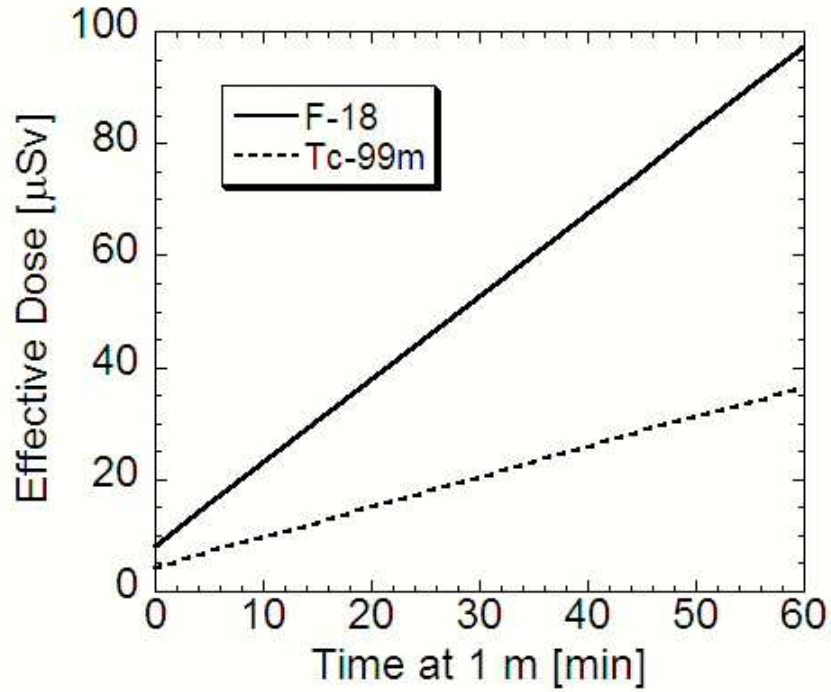


Figure 6-6. Total effective dose during a 10 hour shift for occupational staff directly treating the patient assuming that the time spent at 1 m is the same every hour and the rest of the time is spent at least 4 m from the patient for acquisitions with both ^{18}F and $^{99\text{m}}\text{Tc}$.

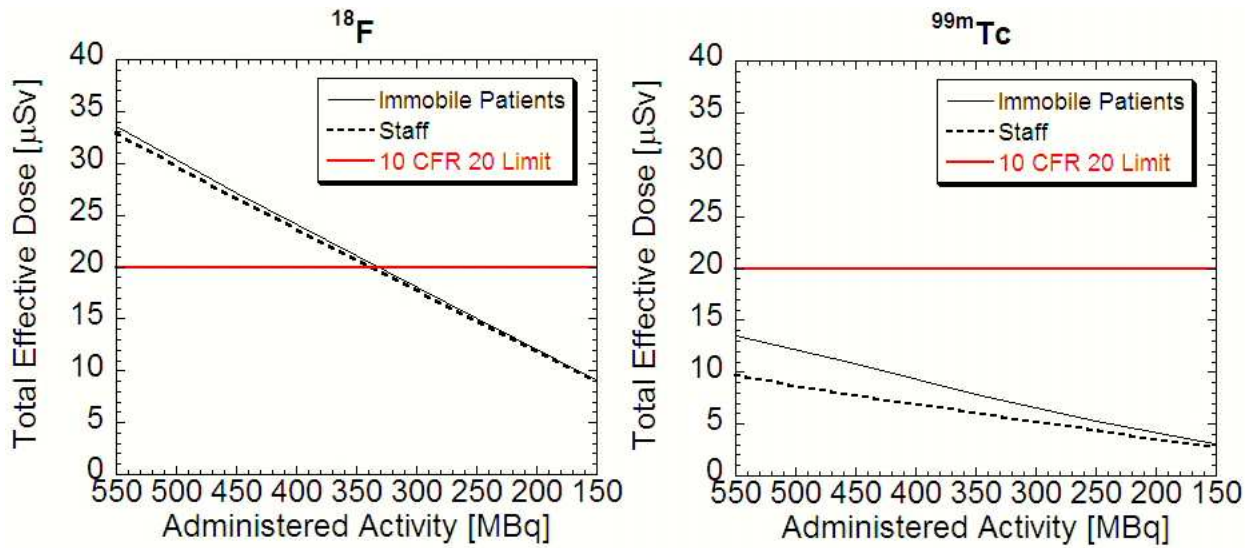


Figure 6-7. Total effective dose to immobile patients and staff in an adjacent room to the ICU with a patient injected with reduced amounts of ^{18}F or $^{99\text{m}}\text{Tc}$.

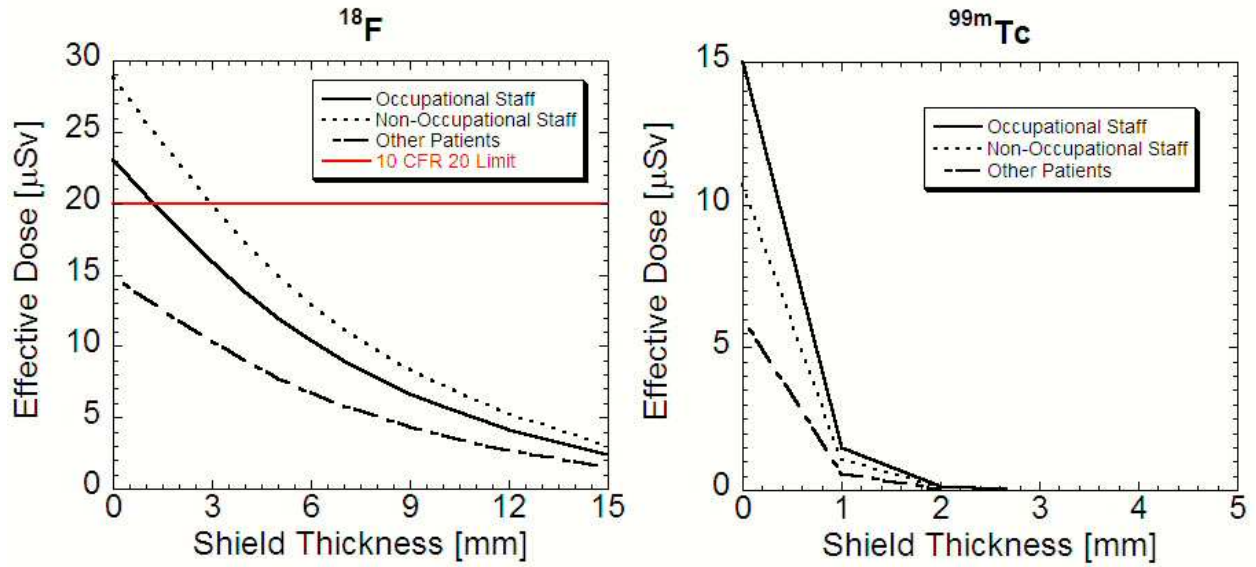


Figure 6-8. Total effective dose with lead shields of varying thicknesses to patients and staff in the ICU for both ^{18}F and $^{99\text{m}}\text{Tc}$ procedures.

Table 6-1. Portable shield weight for varying thicknesses of lead.

Thickness [mm]	Weight [kg] (lbs)	
	Patient Shield (6 ft × 6 ft)	Staff Shield (3 ft × 6 ft)
0	-	-
1	33 (72)	16 (36)
3	122 (270)	61 (135)
6	245 (540)	122 (270)
13	540 (1080)	245 (540)

CHAPTER 7 FUTURE WORK

7.1 Additional Studies

The critical question of whether the performance of this system is adequate to diagnose moderate-to-severe cardiac defects will require further study. There are three aspects of this system that still require evaluation before the final goal of patient imaging can be achieved.

1. Acquiring images on an experimental phantom with realistic defects.
2. Comparison of the simulated high energy pinhole collimator images to actual images using point sources and phantoms to determine if there is a reduction in septal penetration effects.
3. A performance evaluation in PET mode must be performed for this system like in SPECT mode.

7.2 Defect Phantom Acquisitions

Preliminary acquisitions have been done using a cardiac phantom with a defect (Figure 7-1). The defect is approximately 4.1 cm by 2.2 cm and 0.95 cm thick. We acquired a high count (300,000 counts per projection) 25 projection acquisition at both 140 keV and 511 keV. Approximately 2 mCi of activity was mixed in the myocardium and the defect was filled with water, only. We positioned the detector head as close to the phantom as possible to achieve the highest possible spatial resolution. Figure 7-2 shows short and long axis slices from both the 140 keV and 511 keV acquisitions. The images in this figure are unfiltered. The defect is clearly visible in the 140 keV image and can also be distinguished in the 511 keV image although not as clearly due to the degradation from septal penetration photons.

Future work will involve count thinning to simulate lower counts, acquiring at a more realistic radius-of-rotation, adding activity to the defect, and reducing the angular sampling and angular coverage to determine at what level the defect becomes undetectable. These preliminary

acquisitions did provide images demonstrating that the system can detect defects in the myocardium and continue to support the final goal of obtaining clinical images with this system.

7.3 PET Performance Evaluation

Typically the performance evaluation of a PET system would follow the guidelines laid out by National Electrical Manufacturers Association (NEMA) but many of these tests assume a stationary ring of detectors which this mobile system does not have. Therefore, we would use the NEMA NU 2 tests as a guideline but we will conduct our own performance evaluation [46].

A preliminary acquisition with two projection angles and a 10 μCi Sodium-22 (^{22}Na) point source demonstrated the ability of the system to process coincidence data. Figure 7-3 shows the results of this initial acquisition. As expected, streaking artifacts were present from inadequate angular sampling but system capability was demonstrated.

To evaluate the spatial resolution, six point sources of ^{18}F -FDG are placed between the two detectors in the manner described in the NEMA protocol and projections will be obtained with the detectors in opposed orientations. To start, a 37 projections acquisition will provide coverage every 5° over 360° . Because of the confined environment in the clinic that this system will be used in, it most likely will not be possible to achieve this number of projections. Therefore, reconstructions will be done reducing the number of projections obtained from the original acquisition to determine the effect of limited angles on the spatial resolution. Both the FWHM and FWTM of the point spread function (PSF) are measured in the transverse and axial directions in each reconstructed image. As a further test of the spatial resolution of the system, a PET image of a cold rod phantom could be obtained, again with 37 projections to test the effect of limited angles on the reconstructed spatial resolution.

To test the count rate capability of the system, a point source of approximately 2.0 mCi ^{18}F -FDG is placed between the detectors and images will be acquired every 10 min until the

source has decayed away. We expect the system to saturate at the high activity level and then begin to drop as the activity decreases. From this counting curve, the maximum count rate of the system can be calculated. Also, a common test recommended by NEMA is a scatter fraction, count losses, and randoms measurement, but this requires full 360° coverage at each acquisition, which is not feasible with this system. This is a test that would be beneficial if we could formulate a protocol with this system because a scatter fraction correction could be applied to the images.

To test the sensitivity of the system, a single 30 s projection with a point source of ^{18}F -FDG (activity resulting in a count rate below the maximum) is acquired. This allows a calculation of the number of counts/ $\mu\text{Ci/s}$. This is different from the NEMA test since there is not a ring of detectors. This sensitivity measured at one projection can be applied to by multiplying this value to the total number of projections with decay taken into account to obtain an overall sensitivity for an entire acquisition.

The greatest problem facing the PET aspect of this system is the positioning of the detector heads in an opposed orientation because of the gantry readout which only displays a horizontal and vertical component for each head. These can be zeroed to set a reference point for each head individually but calculating a reference point that is common to both heads will be difficult. A protocol for obtaining this reference point is required to be developed and optimized. This is an underlying reason why we decided to evaluate the SPECT approach first, along with the issue of having to rotate a head beneath the bed. This difficulty in positioning a detector below a bed demonstrates that this system will be most likely used in PET mode for brain imaging of immobile patients since support structures will not be as much of an issue around the head. For the evaluation of the PET aspect of this system, a head phantom such as a Hoffman 3D brain

phantom, would be beneficial. It would be beneficial to image the phantom and compare the PET images with images obtained with images obtained using the high energy parallel hole and pinhole collimators to see if there is an advantage of using PET over high energy SPECT with this system. Once all these aspects of the mobile system have been evaluated, the next step would be initial patient studies, reaching the overall goal of this mobile system.

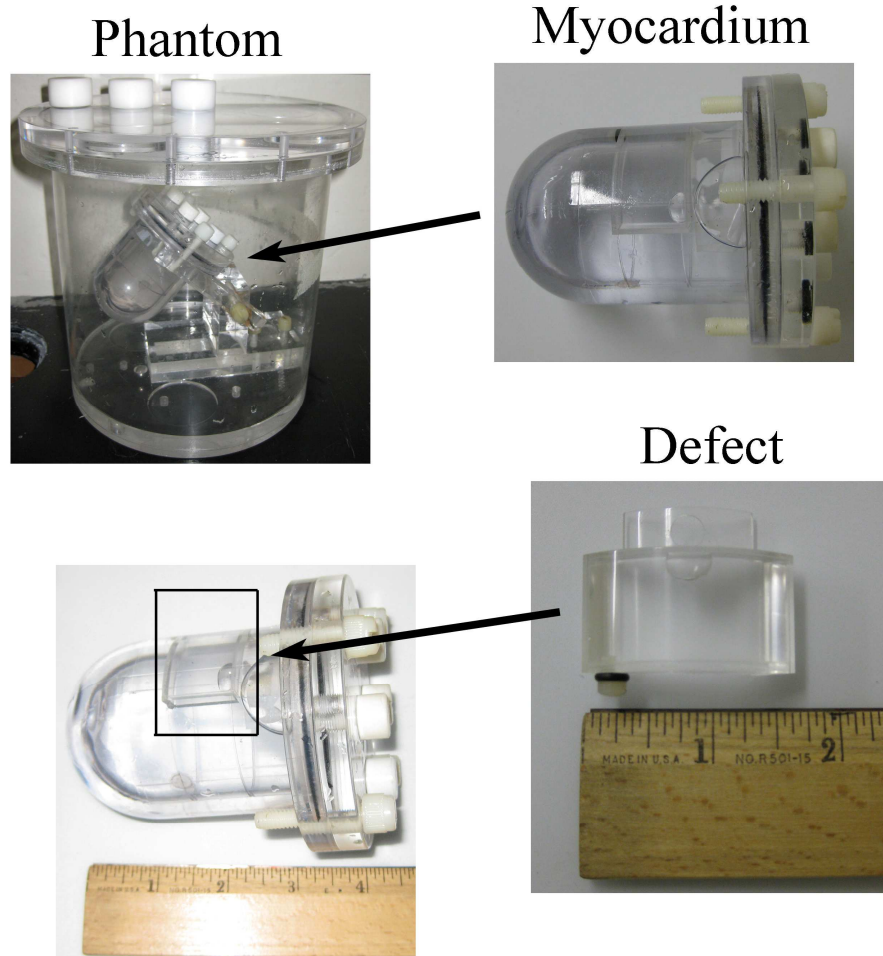


Figure 7-1. Pictures of the defect phantom showing the myocardium and the defect.

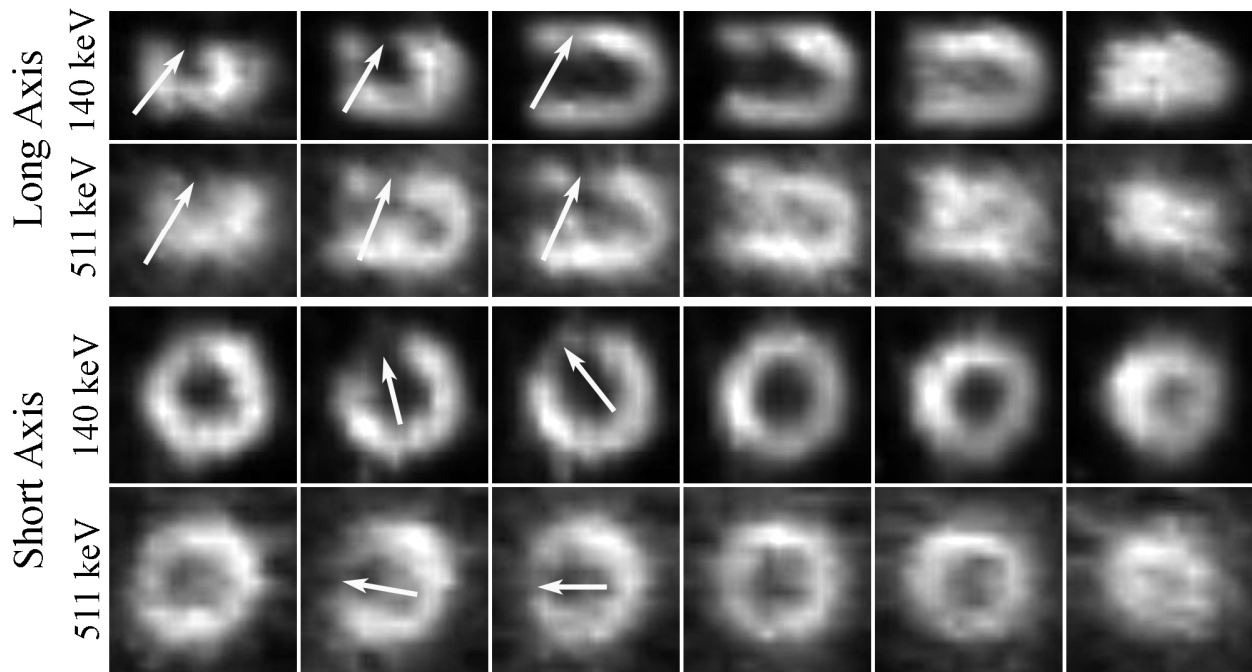


Figure 7-2. Short and long axis slices from the reconstructed image of the cardiac phantom with a defect at both 140 keV and 511 keV. White arrows indicate the defect.

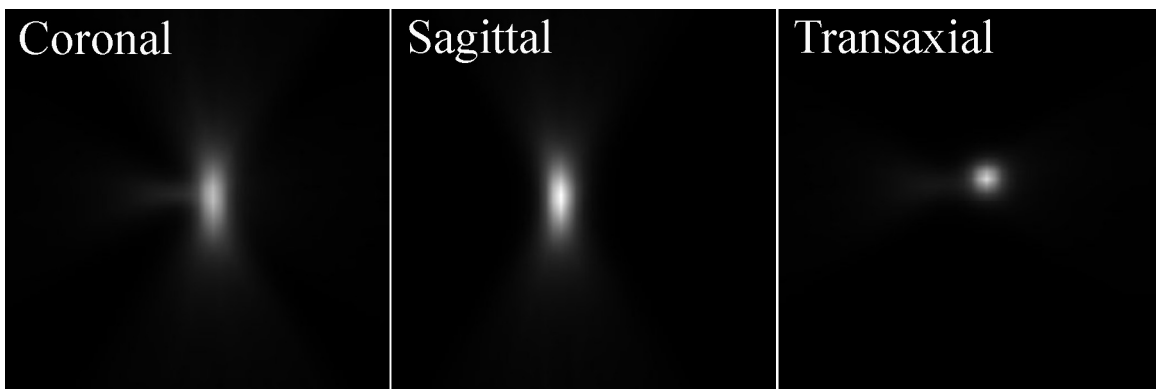


Figure 7-3. Three slices from the preliminary, two projection angle PET acquisition with a ^{22}Na point source demonstrating the system's ability to process coincidence data.

APPENDIX A SYSTEM INSTRUCTION MANUAL

A.1 Powering up the System

1. Ensure all cables are securely connected to detector heads and that the electronics rack is plugged into the wall.
2. Turn on the two power supplies (white boxes on bottom rack).
3. Turn on servers.
4. Turn on high voltage supply and make sure supply is operating correctly before turning on the voltage distribution boxes (on top of power supplies).
5. Ramp up the high voltage supply to the desired level (511 keV level marked on supply and 140 keV level is 100 V higher).
6. Log onto the servers (password located on the inside door of the electronics rack).

A.2 Testing the Detector

1. Start Kmax on either alpha or beta.
2. Click ok when the Doing Cardiac! window appears.
3. Place source (either 140 or 511 keV) at least 3 feet from detector face without a collimator.
4. Click on the control panel tab and perform a quick acquisition by clicking start to ensure the detector is working (if the counts are not seen in the window, right click on the display window and choose expand and then repeat and choose show all). The raw flood image should be visible.
5. Stop and clear the acquisition.

A.3 Setting the Channel Thresholds

1. Click do pedestals in the upper right of the control panel window (might need to maximize the window to see this).
2. Acquire for 30 seconds, stop the acquisition and click do pedestal again.
3. Click on save as default and on ok when the Doing Cardiac! window appears. This step sets the threshold for each channel.

A.4 Energy Calibration

1. Energy calibrations should be done at least once a week or after the system has been off for an extended period of time.

2. Choose the option in the upper left corner of the control panel window to calibrate energy.
3. Start an acquisition and click on the energy calibration tab. To check the calibration, click on the fix peaks button and use the scroll bar in the middle of the window to check the accuracy of the calibration on each channel. The calibration curve is in red at the bottom of the window and should look like a wave.
4. To more accurately find the peaks, the calibration window can be changed using the options in the upper left to ensure the peaks are found (lowest bin, highest bin, FWHM, etc.). Allow enough counts so that the software can identify a peak in each channel. The peak location can be verified by scrolling through each channel and checking that the software determined the correct location.
5. When the calibration curve is set, click use this LUT for current detector at the bottom right of the window (again, the window might have to be maximized to be able to see the scroll bar at the right). This will import the new calibration into the mapped image and LUT tab.
6. Click save as default in the control panel tab first and then choose save as from the control panel tab and name the .cog and .fpga files.
7. Copy these files from where they were saved on alpha or beta to delta where they will be used in the acquisitions.

A.5 Linearity Calibration

1. A linearity correction is required only if the images appear distorted.
2. Perform a long intrinsic flood acquisition and save the raw flood image to the desktop.
3. Open ImageJ (C:\Program Files\ImageJ) and choose plugins, and crystal map.
4. Cancel when it asks to load file. The flood you just obtained should appear. If not, load the saved flood image from where you saved it.
5. The first step is to filter the image to make each pixel as visible as possible. This is done by selecting a region with the yellow box and clicking on the 1. Filter button.
6. The trick is to find a balance between the size of the region you filter and the peak size (ruler at the bottom left). First, select the entire image with a small peak size and click filter. Now reduce the size of the box to a long rectangle that covers the entire area between columns of pixels. Increase the peak size slightly (maybe by 2 or 3). Position the rectangle and click filter again.
7. Choose the option with the cross with 4 arrows. This allows you to move the rectangle without changing the size. Repeat step 6 for the other two vertical regions and the three horizontal regions between the PMTs.

8. Make the rectangle a smaller square and increase the peak size. Filter the regions that are surrounded by 4 PMTs.
9. When all the pixels are clearly visible, the filtering is done. This will take several attempts to become familiar with the relationship between the peak size and area filtered. Usually a larger region requires a smaller peak size.
10. Click 2. Find Peaks. The software will take the filtered image and attempt to locate each pixel and place a yellow circle on them. Change from the cross with four arrow to the circle right above this. This option lets you remove pixels by right clicking or add pixels by left clicking. When adding pixels, the software places the pixel on the nearest peak it finds to your click. If the pixel is not going where you want it, decrease the peak size and the pixel will be set closer to your click location.
11. Be sure to only click find peaks once. Every time this is clicked, another layer of pixels will be added. This can be noticed when you right click on a pixel and it does not appear to be remove. This is due to the fact that an identical pixel was directly underneath it. If this happens, clear the entire map and click find peaks.
12. The goal of this step is to map the 45×45 pixel array. This step might involve creating a new row or column of pixels that the software did not pick up.
13. The magnifying glass option (below the cross with four arrows) is very useful. Left clicking will zoom in on the image and right clicking will zoom out.
14. When you think that you have the 45×45 pixel array, click count all. This will count the total pixels you have selected. You need the number to be 2025. Keep adding and removing pixels until there are 2025.
15. When you have 2025 pixels, click 3. Map Peaks. Enter 45 for column and row. An error message will appear if you do not have exactly 2025 pixels. In this step, the software attempts to number each pixel from 1 to 2025.
16. If the software is unable to label all pixels (it only labels half or less), use the magnifying glass tool to zoom in on the area. Most likely the software confused rows or columns. Ensure that the pixels are counted in order and the software is not jumping from row to row. This will involve adding or removing pixels. Remember to be in peak mode and not filter mode.
17. Keep choosing map peaks until all 2025 pixels are identified.
18. Click 4. Define Regions. The software takes each pixel and defines polygons that represent each pixel. This is the linearity correction.
19. Click 5. Save for KMax.

20. Back in KMax, go to the mapped image and lookup table tab. In the upper right area, right click and choose import histogram data. Import the saved file. It might be necessary to rotate the imported data.
21. Click save as default in the control panel window.

A.6 Starting an Acquisition

1. Start the RMI server on alpha, beta, or both.
2. Acquisitions are performed on delta. There are four saved configurations, alpha140, alpha511, beta140, and beta511. The only difference between them is the .fpga and .cog files that are used for the energy calibration. To change the energy calibration used, add one of the detectors. Choose load from the window at the right for either cog or fpga file where the detector is displayed. Choose the file that was copied from either alpha or beta and then save. This must be done for each detector.
3. Choose either a time limit for the acquisition or an event limit and name the file.
4. The file is output to C:\daq\processed and the detector used (alpha140, etc.) is appended to the filename.
5. For a PET acquisition, two detectors must be added (alpha511 and beta511). Once this is done, select both detectors by holding down ctrl and clicking on both detectors. Next, right click on one of them and choose pair selected carriers. Finally, right click on alpha511 and choose set selected as master. Finally, ensure that on the trigger box, the wires are in the TTL out positions. For a SPECT acquisition, these should be in the C1 and C2 positions.

A.7 Acquisition Protocol

1. Attach the gantry power cord and pendant.
2. Attach the appropriate collimator. The low energy collimator is attached with the side with no screw holes inserted first. The high energy collimator is inserted with the side with the writing first. Attach the collimator with screws.
3. Position the detector at the first projection angle with the detector vertical. Move the detector as close to the phantom/patient as possible. Estimate the radius-of-rotation from the center of the field-of-view to the center of the detector axle and record this number.
4. Zero the horizontal and vertical position indicators on the gantry.
5. Choose the length of the acquisition and name the file in jDaq.
6. Record the detector head angle from the digital protractor and both the horizontal and vertical position from the gantry.

7. When the first projection is completed, rotate the detector head to the next angle and reposition the detector's horizontal and vertical components so the FOV is covered and the detector is as close as possible to the phantom/patient. Create a new file in jDaq and start the acquisition. Record the head angle and the horizontal and vertical position of the detector.
8. Repeat step 7 until the desired angular coverage is achieved. Monitor the cables connected to the detector to make sure they are not stressed or disconnect.
9. Process the projection data.

A.8 Powering the System Down

1. Ramp down the high voltage slowly.
2. Turn off the voltage distribution box.
3. Turn off the high voltage supply.
4. Shut down the servers. You must enter a comment (just a letter is sufficient) before you can shut down.
5. Turn off power supply.

A.9 Troubleshooting

1. Mapping the network. If the network should reset or fail, go into my computer, make sure the network is disconnected, and then select tools and map network drive. The network is in the V:\ drive and then browse folders, detector\Daq_delta\JDaq_Settings to reconnect the network.
2. Acquisition will not finish and always stops at the same event number. This occurs because the acquisitions are cached on alpha and beta. The old files must be periodically deleted or the hard drive on alpha and beta fills up (files located in the D:\ local disk drive on alpha and beta). The files are the same as saved on delta is deleting them will not remove anything from delta.

APPENDIX B
MATLAB CODE FOR IMAGE POST-PROCESSING

B.1 SPECT Listmode Data Processing

```
clc;
clear all;

% image to process
fid=fopen('projection.bin','r','b');

% saved flood image
fid2=fopen('flood.bin','r','l');

% corrected image file to write
fid3=fopen('corrected.bin','w','l');

list=fread(fid,'int16'); % read listmode data
head=zeros(45,45); % set detector pixels to 0
energys=zeros(1,1024); % set energy spectrum to zero

% generate the energy spectrum
for x=1:7:length(list)
    if(list(x+2)>0 && list(x+2)<2000)
        energys(list(x+2))=energys(list(x+2))+1;
    end
end

% find the peak of the energy spectrum for an energy window
for x=1:length(energys)
    if(energys(x)==max(energys))
        max_pix_1=x;
    end
end

% increment each pixel by 1 if the event is within your chosen energy window (20% in this
case; 10% on either side of the max energy spectrum value)
for x=1:7:length(list)
    if(list(x)<50 && list(x+1)<50 && list(x+2)>(max_pix_1-(max_pix_1*.1)) &&
list(x+1)<(max_pix_1+(max_pix_1*.1)))
        head(list(x)+1,list(x+1)+1)=head(list(x)+1,list(x+1)+1)+1;
    end
end

% read in the saved flood image
flood=fread(fid2,[45 45],'int16');
```

```

% uniformity correct the projection image with the saved flood image
meanf=mean(mean(flood));
cor_flood=meanf./flood;
corrected=cor_flood.*head;

corrected=corrected';

% write the corrected image
fwrite(fid3,corrected,'int16')

```

B.2 Center-of-rotation Correction

```

clc;
clear all;

hor=[0 1 2 3 etc.]; % enter the horizontal position of each projection image
vert=[0 1 2 3 etc.]; % enter the vertical position of each projection image
theta=[0 1 2 3 etc.]; % enter the detector angle of each projection image
ROR=235; % estimated radius of rotation in mm
num_proj=19; % # of projection angles

hor_conv=1/200; % 200 counts/mm gantry conversion
ver_conv=1/288; % 288 counts/mm gantry conversion

h=hor.*hor_conv; % get the h and v values in mm
v=vert.*ver_conv;

% read in projection image
fid=fopen('image.prj','r','l');
fid2=fopen('new_image.shift','w','l');

image=fread(fid,[45 45*num_proj],'int16');

% average into 46x46 pixel matrix
for slice=1:num_proj
    for y=1:45
        for x=1:45
            projection(x,y,slice)=image(x,y+(45*(slice-1)));
        end
    end
end

for slice=1:num_proj
    for x=1:45
        for y=1:45
            if(x==1)

```

```

        projection_avg(x,y,slice)=projection(x,y,slice)/2;
        projection_avg(46,y,slice)=projection(45,y,slice)/2;
    else
        projection_avg(x,y,slice)=(projection(x,y,slice)+projection(x-1,y,slice))/2;
    end
end
end
end
end

```

```

for slice=1:num_proj
    for y=1:45
        for x=1:45
            if(y==1)
                projection_avg(x,y,slice)=projection(x,y,slice)/2;
                projection_avg(x,46,slice)=projection(x,45,slice)/2;
            else
                projection_avg(x,y,slice)=(projection(x,y,slice)+projection(x,y-1,slice))/2;
            end
        end
    end
end
end
end

```

% this creates a new image matrix that is 256x256 pixels so filtering can be done
shifted=zeros(256, 256, 19);

d=zeros(1,num_proj); % set the initial shift to 0

% calculate the shift required at each projection angle

```

for n=1:num_proj
    if(h(n)<=ROR)
        x=ROR-h(n);
        y=v(n);
        r=sqrt(x^2+y^2);
        t1=atan(y/x)*(180/pi);
        if(t1<=theta(n))
            t2=(theta(n)-t1)*(pi/180);
        else(t1>theta(n))
            t2=-(t1-theta(n))*(pi/180);
        end
        d(1,n)=r*sin(t2);
    end
    if(h(n)>ROR)
        x=h(n)-ROR;
        y=v(n);
        r=sqrt(x^2+y^2);
        t1=atan(y/x)*(180/pi);
    end
end

```

```

    if(t1>=(180-theta(n)))
        t2=(t1-(180-theta(n)))*(pi/180);
    else(t1<(180-theta(n)))
        t2=-((180-theta(n))-t1)*(pi/180);
    end
    d(1,n)=r*sin(t2);
end
end

d=int16(d.*(1/5)); % convert the shift into pixels from mm (5 mm/pixel)

% shift the image by d pixels in the new 256x256 matrix
for n=1:num_proj
    yc=0;
    for y=105:150
        yc=yc+1;
        xc=1;
        for x=105+d(n):150+d(n)
            shifted(x,y,n)=projection_avg(xc,yc,n);
            xc=xc+1;
        end
    end
end
end

% join the shifted images back together (as many as are needed depending on num_proj)
shifted_new=cat(2,shifted(:, :, 1),shifted(:, :, 2), ... , shifted(:, :, num_proj));

fwrite(fid2, shifted_new, 'float32'); % write shifted image

```

LIST OF REFERENCES

1. S. Dale, M. Holmberg, H. Larsson, M. Persson, T. Ribbe, H. Elmquist, D. Bone, L. A. Brodin, C. Lindstrom, and L. Jorfeldt, "A mobile tomographic gamma camera system for acute studies based on ectomography." *Nuclear Science Symposium and Medical Imaging Conference*, Oct. 1995. Vol. 2, 934-938.
2. M. Persson, D. Bone, L. Brodin, S. Dale, C. Lindstrom, T. Ribbe, and H. Elmquist, "A mobile gamma camera system for 3D acute myocardial perfusion imaging." *Computers in Cardiology*. 7-10 Sept. 1997. 685-688.
3. S. Dale, and P. Edholm. "Gamma camera ectomography with a limited view angle." *Nuclear Science Symposium and Medical Imaging Conference*, Oct. 1992. Vol. 2, 1098-1100.
4. B. Pichler, T. Gremillion, V. Ermer, M. Schmand, B. Bendriem, M. Schwaiger, S. I. Ziegler, R. Nutt, and S. D. Miller, "Detector characterization and detector setup of a NaI-LSO PET/SPECT camera." *IEEE Trans. Nuc. Sci.* Vol. 50, No. 5, Oct. 2003.
5. I. Matsunari, T. Yoneyama, S. Kanayama, M. Matsudaira, K. Nakajima, J. Taki, S.G. Nekolla, N. Tonami, K. Hisada, "Phantom Studies for Estimation of Defect Size on Cardiac ^{18}F SPECT and PET: Implications for Myocardial Viability Assessment." *J. Nucl. Med.* 2001; 42:1579-1585.
6. M. N. Mabuchi, K. Kubo, K. Morita, Y. Noriyasu, C. Itoh, Y. Katoh, N. Kuge, N. Tamaki, "Value and Limitation of Myocardial Fluorodeoxyglucose Single Photon Emission Computed Tomography using Ultra-high energy Collimators for Assessing Myocardial Viability." *Nuc. Med. Commun.* 2002; 23:879-885.
7. A. G. Weisenberger, S. Majewski, D. Gilland, W. Hammond, B. Kross, V. Popov, J. Proffitt, J. McKisson, and M. F. Smith, "Implementation of a Mobile, Cardiac PET Imager for the Emergency Room and Intensive Care Unit," *2007 IEEE Nuclear Science Symposium and Medical Imaging Conference*.
8. R. R. Raylman, S. Majewski, M. F. Smith, R. Wojcik, A. Weisenberger, B. Kross, V. Popov, J.J. Derakhshan, "Comparison of Scintillators for Positron Emission Mammography (PEM) Systems." *IEEE Trans. Nucl. Sci.*, 2003; 50:42-49.
9. U. Tipnis, M. Smith, T. Turkington, J. Wilson, S. Majewski, D. Gilland, "A Simulation Study of a Bedside Cardiac PET Imager." *2004 IEEE Nuclear Science Symposium Conference Record*, 16-22 Oct, 2004, vol. 5, pp. 3126-3129.
10. S. Cherry, J. Sorenson, and M. Phelps. *Physics in Nuclear Medicine*, 3rd Ed. Philadelphia, PA. Saunders, 2003.
11. L. A. Shepp and Y. Vardi, "Maximum Likelihood Reconstruction in Positron Emission Tomography," *IEEE Trans. Medical Imaging*. 1 (2), 113-122, 1982.

12. H. H. Barrett and W. Swindell. Radiological Imaging: The Theory of Image Formation, Detection, and Processing. San Diego, CA. Academic Press Inc., 1981.
13. C. Laymon and T. Turkington, "Characterization of Septal Penetration in 511 keV SPECT," *Nuc. Med. Comm.* 27(11), 901-909, 2006.
14. L. Adam, J. Karp, and R. Freifelder, "Energy-Based Scatter Correction for 3-D PET Scanners using NaI(Tl) Detectors," *IEEE Trans. Medical Imaging*. Vol. 19, No. 5, May 2000.
15. Y. Qi, B. Tsui, B. Yoder, and E. Frey, "Characteristics of Compact Detectors based on Pixellated NaI(Tl) Crystal Arrays," *2002 IEEE Nuclear Science Symposium Conference Record*, 10-16 Nov. 2002.
16. R. Pani, R. Pellegrini, M. N. Cinti, P. Bennati, M. Betti, V. Casali, O. Schillaci, M. Mattioli, V. Orsolini Cencelli, F. Navaria, *et al.* "Recent Advances and Future Perspectives of Gamma Camera Imagers for Scintimammography," *Nucl. Instr. and Meths.* A 569, 296-300, 2006.
17. C. Jeanguillaume, A. Douiri, M. Quartuccio, S. Begot, D. Franck, M. Tence, and P. Bellongue, "CACAO a Collimation Means well Suited for Pixellated γ -Camera," *2001 IEEE Nuclear Science Symposium Conference Record*, Vol. 4, pp. 2291-2294. 4-10 Oct. 2001.
18. M. A. King, R. B. Schwinger, B. C. Penney, P. W. Doherty, and J. A. Bianco. "Digital restoration of Indium-111 and Iodine-123 SPECT images with optimized Metz filters," *J. Nucl. Med.* 27:1327-1336, 1986.
19. R. Bartoszynski and M. Niewiadomska-Bugaj. *Probability and Statistical Inference 2nd Ed.*, Wiley-Interscience, 2008.
20. C. E. Metz. "A mathematical investigation of radioisotope scan image processing," Doctoral thesis, University of Pennsylvania, 1969. Ann Arbor, MI. University Microfilms, Publication 70-16-186.
21. D. E. Copeland and E. W. Benjamin, "Pinhole camera for gamma ray sources," *Nucleonics*, vol. 5, pp. 44-49, 1949.
22. R. K. Mortimer, H. O. Anger, and C. A. Tobias, "The gamma ray pinhole camera with image amplifier," *Conv. Rec. Institute of Radio Engineers, Part 9-Medical and Nuclear Electronics*, 1954, pp. 2-5.
23. D. Paix, "Pinhole imaging of gamma rays," *Phys. Med. Biol.*, vol. 12, no. 4, pp. 489-500, 1967.
24. F. J. Beekman and B. Vastenhouw, "Design and simulation of a high resolution stationary SPECT system for small animal," *Phys. Med. Biol.* Vol. 49: 4579-4592, 2004.

25. D. A. Weber, M. Ivanovic, D. Franceschi, S. E. Strand, K. Erlandsson, M. Franceschi, *et al.* "Pinhole SPECT: An approach to in vivo high resolution SPECT imaging in laboratory animals," *J. Nucl. Med.* vol. 35, no. 2, pp. 342-384, 1994.
26. P. M. Wanet, A. Sand, and J. Abramovici, "Physical and clinical evaluation of high-resolution thyroid pinhole tomography," *J. Nucl. Med.* vol. 37, no. 12, pp. 2017-2020, 1996.
27. A. Spanu, M. E. Solinas, A. Falhci, S. Nuvoli, F. Chessa, and G. Madeddu, "Tc-99m Tetrofosmin neck pinhole SPECT vs. ultrasonography in differentiated thyroid carcinoma patients," *J. Nucl. Med.* vol. 42, no. 5, p. 325P, 2001.
28. A. Spanu, G. Dettori, F. Chessa, P. Cottu, S. Nuvoli, A. Porcu, P. Solinas, B. Stochino, and G. Madeddu, "Tc-99m Tetrofosmin axillary, planar, SPECT and pinhole SPECT in breast cancer non palpable lymph node metastases detection," *J. Nucl. Med.* vol. 42, no. 5, p 24P, 2001.
29. D. R. Gilland, E. L. Johnson, T. G. Turkington, R. E. Coleman, and R. Jaszczak, "Evaluation of a pinhole collimator for I-131 SPECT head imaging," *IEEE Trans. Nucl. Sci.* vol. 43, pp. 1126-1132, Aug. 1996.
30. M. F. Smith, D. R. Gilland, R. E. Coleman, and R. Jaszczak, "Quantitative imaging of I-131 distributions in brain tumors with pinhole SPECT: A phantom study," *J. Nucl. Med.* Vol. 39:856-864, 1998.
31. M. F. Smith, R. J. Jaszczak, and H. Wang, "Pinhole aperture design for I-131 tumor imaging," *IEEE Trans. Nucl. Sci.* Vol. 44:1154-1160, 1997.
32. M. Smith, R. Jaszczak, H. Wang, and J. Li, "Lead and tungsten pinhole inserts for I-131 SPECT tumor imaging: Experimental measurements and photon transport simulations," *IEEE Trans. Nuc. Sci.* Vol. 44, No. 1, Feb. 1997.
33. G. Santin, D. Strul, D. Lazaro, L. Simon, M. Krieguer, M. Vieira Martins, V. Breton, and C. Morel, "GATE: A Geant4-based simulation platform for PET and SPECT integrated movement and time management," *IEEE Trans. Nucl. Sci.* Vol. 50:1516-1521, 2003.
34. Geant4 Collaboration, "GEANT4: A Simulation Toolkit," *Nuclear Instruments and Methods in Physics Research*, NIM A 506:250-303, 2003.
35. H. O. Anger, "Radioisotope cameras," *Instrumentation in Nuclear Medicine*, G. J. Hinc, Ed. New York: Academic, 1967, vol. 1, pp. 485-552.
36. S. D. Metzler, J.E. Bowsher, K. L. Greer, and R. J. Jaszczak, "Analytic determination of the pinhole collimator's point-spread function and RMS resolution with penetration," *IEEE Trans. Med. Imag.* vol. 21, no. 8, Aug. 2002.

37. S. D. Metzler, J. E. Bowsher, M. F. Smith, and R. J. Jaszczak, "Analytic determination of a pinhole collimator sensitivity with penetration," *IEEE Trans. Med. Imag.* vol. 20, no. 8, Aug. 2001.
38. E. Marieb, and K. Hoehn, *Human Anatomy and Physiology*, Pearson Education, Inc. San Francisco, CA. 2007.
39. C. R. Tenney, M. F. Smith, K. L. Greer, and R. J. Jaszczak, "Uranium pinhole collimators for I-131 SPECT imaging," *IEEE Trans. Nucl. Sci.* Vol. 46:1165-1172, 1999.
40. C. R. Tenney, "Pinhole edge penetration and scatter in small-animal energy-integrating pinhole emission computed tomography," *IEEE Nuclear Science Symposium Conference Record*, vol. 3, pp. 1810-1814, 19-25 Oct., 2003.
41. S. D. Metzler, K. L. Greer, and R. J. Jaszczak, "Helical pinhole SPECT for small-animal imaging: A method for addressing sampling completeness," *IEEE Trans. Nucl. Sci.* Vol. 50, No. 5, 1575-1582, Oct. 2003.
42. W. P. Segars, D. S. Lalush, and B. W. S. Tsui, "A realistic spline-based dynamic heart phantom," *IEEE Trans. Nucl. Sci.* 46(3):503-506, 1999.
43. M. J. Berger, J.H. Hubbell, S. M. Seltzer, J. Chang, J. S. Coursey, R. Sukumar, and D. S. Zucker, (2005), *XCOM: Photon cross section database* (version 1.3). [Online] Available: <http://physics.nist.gov/xcom> [2008, November 19]. National Institute of Standards and Technology, Gaithersburg, MD.
44. M. T. Madsen, J. A. Anderson, J. R. Halama, J. Kleck, D. J. Simpkin, J. R. Votaw, R. E. Wendt III, L. E. Williams, and M. E. Yester, "AAPM Task Group 108: PET and PET/CT shielding requirements," *Med. Phys.* 33 (1), Jan. 2006.
45. B. Schlein, L. Slaback, and B. Birky. *Handbook of Health Physics and Radiological Health*, 3rd Ed., Baltimore, MD. Lippincott, Williams, and Wilkins, 1998.
46. National Electrical Manufacturers Association. "NEMA Standards Publication NU 2-2001: Performance Measurements of Positron Emission Tomographs." Rosslyn, VA 22209. 2001.

BIOGRAPHICAL SKETCH

Matthew Thomas Studenski was born in Royal Oak, Michigan, in 1983. Matthew received his Bachelor of Science degree in 2005 from the University of Michigan–Ann Arbor in nuclear engineering and radiological sciences and in 2006, he received his Master of Science degree from the University of Michigan–Ann Arbor in nuclear engineering and radiological sciences. After graduation, he began work on his Ph. D. at the University of Florida focusing on nuclear medicine and imaging applications. In 2008, he received a Master of Science degree from the University of Florida in nuclear engineering sciences and in 2009 he received his Ph. D. from the University of Florida in nuclear engineering sciences.

While finishing his master's degree at the University of Michigan with Dr. Kimberlee Kearfott, Matthew published two articles: (1) Design and Simulation of a Neutron Facility. *Health Physics. Operational Radiation Safety*. 92(2) (Supplement 1): S37-S44, February 2007. and (2) Simulation, Design, and Construction of a Cs-137 Irradiation Facility. *Health Physics. Operational Radiation Safety*. 92(5) (Supplement 2): S78-S86, May 2007.